Hydromorphic response dynamics of oak

Arends, T.

Award date:
2016

HYGROMORPHIC RESPONSE DYNAMICS OF OAK

MASTER'S THESIS

Thomas Arends

Hygromorphic response dynamics of oak

Thomas Arends

s114129

Graduation committee members:

dr. ir. L. Pel

dr. ir. H.L. Schellen

ir. R.A. Luimes

prof. dr. ir. A.S.J. Suiker

11 July 2016

The work described in this thesis was carried out in the group Transport in Permeable Media at the Eindhoven University of Technology, Department of Applied Physics.

CONTENTS

1 INTRODUCTION

Examples of wood products exposed to a cyclically fluctuating relative humidity are abundant: one may think of furniture, parquet floors, structural elements, or art objects. Being a hygroscopic material, wood strives for equilibrium with the moisture in the ambient air. During these dynamic exposure conditions, the moisture content at the surface of the material changes continuously, provoking moisture transport inside the material, thereby changing the moisture locally and macroscopically. In wood, a change in the moisture content is accompanied by expansion or shrinkage. Macroscopically, this is observed as a shape change in the object. These shape changes can be desirable, e.g., in barrels where the sealing is assured by expanded boards, but it can also lead to undesired effects. A warping parquet floor is a relatively innocent example, more serious consequences can arise when the stresses associated with expansion or shrinkage reach high values. Exceedance of the material's strength by these stresses results in material failure, manifested for example in the formation of cracks. This is obviously unwanted if art objects are considered. The study of the shape changes of wood during dynamic relative humidity conditions is therefore important. In order to relate moisture in wood to expansion under dynamic conditions, first an extensive literature study is performed to gather existing knowledge on wood microstructure and moisture-wood interactions.

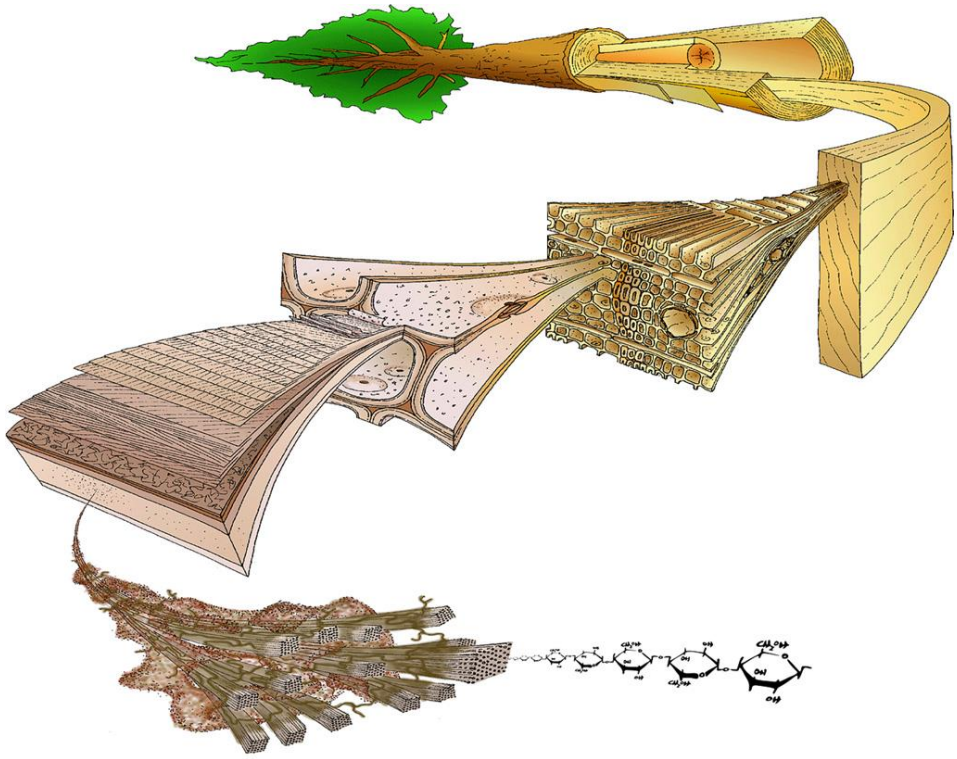

Figure 1.1: *The hierarchical structure of softwood (Harrington, 1996).*

1.1 WOOD AS A MATERIAL

Wood has been used by mankind for thousands of years. Its abundance, natural appearance, and durability have led to application not only in construction, but also as a source of energy, to manufacture weaponry, or in the creation of art objects. However, wood is not an engineered material, it is an organic material designed by nature to fulfil the needs of a living tree. Its microstructure and the resulting properties on a macroscopic scale are consequences of its purpose. The trunk of a tree must mechanically support its crown, transport minerals and water from the roots of the tree to the leaves, and it should be able to store nutrients (Forest Products Laboratory, 2010). To perform these functions, an interconnected system of cells constitutes the wood. This results in a complex microstructure, with highly inhomogeneous characteristics and anisotropic properties. Furthermore, the tree as a natural system grows during its life, which leads particularities on the mesoscale. All these features make wood a multi-scale, hierarchical material with characteristic structures on different levels of detail, as elucidated in Figure 1.1. It is therefore common to analyze the structure of wood on different scales to better understand its macroscopic properties. A familiar way to elucidate characteristic features of a tree is to consider a cross-section of the trunk of a tree.

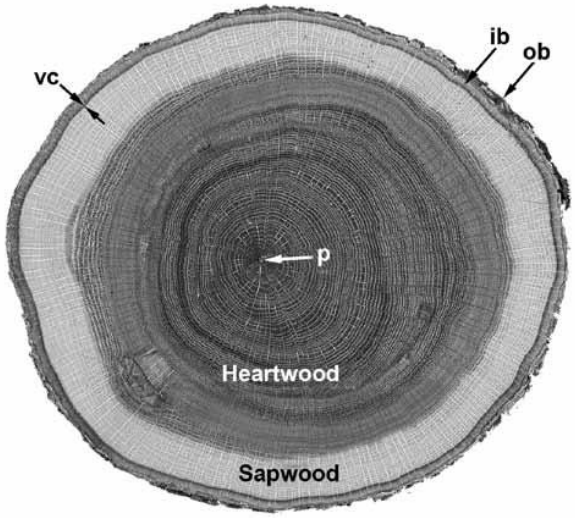

Figure 1.2: *A transverse section of white oak (Quercus Alba), with the distinct macroscopic regions from outside to inside: outer bark (ob), inner bark (ib), vascular cambium (vc), sapwood, heartwood, and pith (p) (Forest Products Laboratory, 2010).*

The cross-section of the trunk of a tree in Figure 1.2 shows several distinctive regions and particularities. On the outside of the tree, the outer bark limits the evaporation of water and protects the softer inner bark from external mechanical influences. The inner bark is the tissue through which transport of nutrients from the leaves to the roots or growing parts of the tree takes place. A thin layer known as the vascular cambium produces tissue by cell division for both the inner bark and the sapwood it surrounds. Conduction of water and nutrients from the roots of the tree to its leaves, and storage and synthesis of bio-chemicals takes place in the sapwood. It is distinguishable by its lighter color from the dark heartwood. In contrast to the sapwood, the heartwood is a non-active part of the trunk. Its main purpose is the storage of

chemicals known as extractives, which are, e.g., responsible for the resistance to fungi or water in several species. Finally, the pith in the center of the trunk is the remnant of the early growth of the tree.

A common feature found in the cross-section of many species is the presence of growth rings. Seasonal differences in growth result in alternate concentric regions of earlywood (less dense) and latewood (dense). With the introduction of growth rings, three principle directions can be distinguished. The longitudinal or axial direction is along the growing direction of the tree; the radial direction runs from the center of the tree to the bark; perpendicular to both directions, the tangential direction is tangent to the growth rings. Due to the microstructural organization, properties are dependent on the orientation of wood. Wood is, e.g., more permeable and stiff in the longitudinal direction compared to the other two directions.

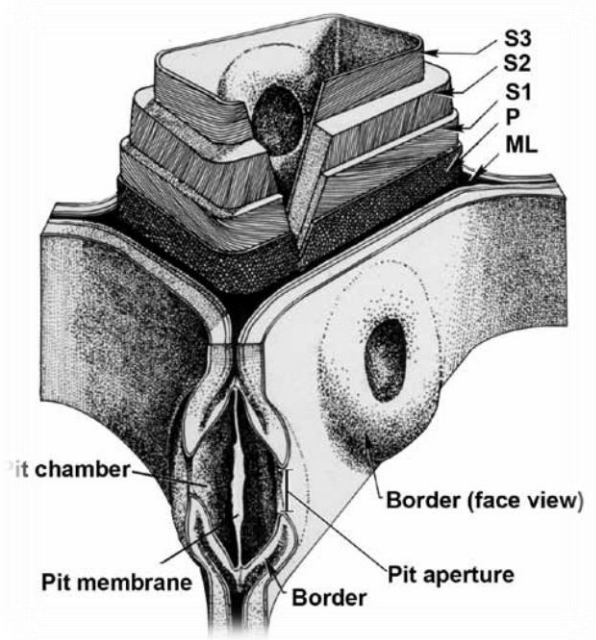

Figure 1.3: *Cellular structure of wood cell types. The void space, known as lumen, is surrounded by three secondary cell wall layers (S1, S2, S3), a primary layer (P), and the middle lamella (ML). Transport between cells takes place through thin regions in the cell wall, known as pits (Forest Products Laboratory, 2010).*

An important difference between wood and other living natural systems is that most cells are dead at maturity, even in the active sapwood. In contrast to a living plant cell, composed of protoplast and cell wall, cells in wood have removed their protoplast before reaching functional maturity. This leaves an air void, known as the lumen, encapsulated by the cell wall. The lumen and cell wall are often referred to as a cell in wood literature. The main function of a wood cell, shown in Figure 1.3, is carried solely by the cell wall; it provides mechanical support and buffering capacity. The cell wall is a carbohydrate matrix, consisting of three major layers: the middle lamella, the primary wall, and the secondary wall. All these layers are composed for the most part of cellulose microfibrils, hemicellulose, and a matrix of pectin or lignin (Forest Products Laboratory, 2010). The microfibrils can be seen as strong thread-like macromolecules of cellulose with high tensile strength, whereas lignin is a brittle matrix. Hemicelluloses are smaller branched molecules, which interconnect the microfibrils

and the matrix into a unified system in each layer of the cell wall. The angle of the microfibrils is different in each of the cell wall layers, thereby influencing its mechanical properties (Rafsanjani, et al., 2012). Interconnection between the cells for transport of biochemicals and water is assured through thin areas in the cell wall, known as pits. The number, type, and size of these pits influences wood properties to a large extent, ranging from moisture transport to the response of wood to the application of a coating.

The above described characteristics of the tree are typical for the approximately 20,000 different species of woody plants (Forest Products Laboratory, 2010). Each specie has, however, more or less unique features. Different species may for example be characterized by their leaves. Moreover, structural differences are visible from a cross-section of the trunk. Wood species can, nevertheless, be divided in two main types: softwoods and hardwoods. These names may be misleading, since they not necessarily indicate mechanical resistance. Apart from the botanic definition of softwood and hardwood as coming from gymnosperm or angiosperm trees respectively, the types cover two distinct cellular arrangements. Softwoods have a simple basic structure with roughly two cell types. Longitudinally oriented long (1-10 mm) tracheid cells and radial brick-like ray parenchyma cells constitute the microstructure. Transport of water and nutrients in the vertical direction of the tree takes place through the tracheids, whereas the rays ensure transport from the center towards the bark. Hardwoods possess a higher degree of structural complexity. Not only the number of different hardwood cell types is higher, they also exhibit more variation compared to the two softwood cell types. Although the radial system is composed of rays, just as in softwoods, rays in hardwood can be more than one cell wide, and the variability in shapes and sizes is higher. Furthermore, the longitudinal system is composed of various kinds of vessel elements, fibers, and axial parenchyma cells. Axial parenchyma cells are only occasionally present in softwood, but more abundant and varied patterns exist in hardwoods. Fibers in hardwood serve almost exclusively as mechanical support. In some hardwood species, such as oak, special cells are present circulating around a vessel, known as vessel tracheids. Vessel elements are specialized hardwood cells, absent in softwoods, which are stacked onto each other, connected through so-called perforation plates. A wide range in vessel diameters is present, but typical sizes range from 50 to 200 μm. In some hardwood species, large vessels can be observed from a cross-section by the naked eye, as is the case in oak. Owing to their small size, pores in softwoods are not visible by eye. Moreover, a difference in diameters between latewood and earlywood can be present dependent on the species, which is also the case in softwood with tracheids. Cells are typically thin-walled in earlywood, whereas the cell wall is thicker in the latewood.

1.2 MOISTURE IN WOOD

The main constituents of the wood cell wall are cellulose, hemicellulose, and lignin. Although the lignin which glues the cell together is more hydrophobic, the ability of the hydroxyl-groups on the cellulose and hemicellulose polymers to bind water molecules make the cell wall hygroscopic. Furthermore, moisture can be present in the lumen as liquid water or water

vapor. Green wood, i.e. a freshly cut tree, generally contains water in these three forms: 'free' liquid water in the lumens, water vapor in the empty parts of lumens, and 'bound' water in the cell walls (Skaar, 1988). Upon drying, i.e. with decreasing moisture content, the wood will first lose its liquid water. At some point, a moisture content is reached at which no liquid water is present in the cell cavities, but the cell walls are fully saturated with moisture. This point is often denoted the fiber saturation point (FSP), although its notion has been subject of discussion (Engelund, et al., 2013), and still many definitions circulate in literature. Depending on the definition, different values for moisture content (kg of moisture / kg of dry material) are assigned to the FSP, commonly around 0.25 to 0.30 (Forest Products Laboratory, 2010). Regardless of the definition, only water in the cell walls and water vapor in the cell cavities are present below the FSP. The range between completely dry and the FSP is denoted the hygroscopic range of water in wood. In the hygroscopic range, the relationship between the relative humidity of the ambient air and the moisture content in equilibrium is characterized in terms of the sorption isotherm. Different theories of moisture sorption in wood circulate in literature (Brunauer, et al., 1938; Babbitt, 1942; Dent, 1977), resulting in a wide variety of sorption curves (Simpson, 1973; Simpson, 1980). Although the equations may appear different, they can often be reduced to the same mathematical form (Bouquet, et al., 1980).

The relation of ambient relative humidity to moisture content is often not unique. Dependent on the sorption history, the moisture content at a certain relative humidity may be in a range of values. This phenomenon, known as sorption hysteresis, has been the subject of various studies (Merakeb, et al., 2009; Patera, et al., 2015). Multiple explanations exist to account for the discrepancy in moisture content during adsorption and desorption (Time, 1998), e.g., based on incomplete wetting, capillary condensation, and sorption site availability.

1.2.1 MOISTURE TRANSPORT

The sorption curve represents the equilibrium relation between ambient relative humidity and moisture in wood. In real-life applications, wood is rarely in equilibrium with the moisture in the ambient air. In these non-equilibrium conditions, transport of moisture takes place. Furthermore, transport can also take place when wood is in contact with liquid water. This gives rise to the division of moisture transport in wood into two main regimes (Siau, 1984). Above the FSP, moisture transport is governed by liquid water flow: a gradient in the static or capillary pressure causes moisture to flow through interconnected pores. Below the FSP with no liquid water present, moisture transport may be subdivided into diffusion of water vapor through the air in the lumens of the wood cells, and transport of bound water in wood cell walls. In all these transport mechanisms, the driving force for moisture transport is a gradient in the chemical potential of water (Avramidis, et al., 1992), also denoted water potential (Siau, 1984). Many factors influence the chemical potential of water present in the porous matrix of wood, e.g., vapor pressure, static pressure, capillary pressure, or mechanical stresses (Sar, et al., 2012). Moreover, temperature has an undisputed impact on the chemical potential. A gradient in any of these aspects thus provokes moisture transport. Since some of these processes depend on moisture content, or can even be directly related to moisture content,

moisture transport in wood is often described by Fick's first law of diffusion. In Fick's first law, the moisture flux **J** is proportional to a gradient in moisture content θ:

$$\mathbf{J} = -D\nabla\theta, \tag{1.1}$$

where D is the diffusion coefficient. In the hygroscopic range, the transport of water vapor and bound water in the cell walls is sometimes treated together, to arrive at a single diffusion equation with the flux proportional to a gradient in the total moisture content, with constant diffusion coefficient (Tuttle, 1925), or diffusion coefficients dependent on moisture content or temperature (Stamm & Nelson, 1961; Nelson, 1986; Simpson, 1993; Kang, et al., 2008; Pereria da Silva, et al., 2015). In this approach, the diffusion coefficient is a combined parameter for both transport processes. Furthermore it is implicitly assumed that water vapor in the lumens and bound water in the cell walls are in equilibrium at all times. In sorption experiments on wood, however, non-Fickian effects have been encountered (Wadsö, 1994). Examples of such effects are the dependence of the diffusion coefficient on the thickness of the sample or the size of the imposed step change, which have no physical relevance. To account for these effects, other ways to describe moisture transport in wood have been suggested. In some of these approaches the diffusion of moisture in the vapor phase and the bound water transport are treated separately, but both processes are coupled by a sorption rate (Skaar & Babiak, 1982; Siau, 1984; Avramidis, et al., 1992; Cunningham, 1995; Krabbenhoft & Damkilde, 2004; Kang, et al., 2009), which can also be dependent on the moisture content (Dvinskikh, et al., 2011). This has also been the starting point of several modeling studies (Eitelberger, et al., 2011; Eitelberger & Hofstetter, 2011). Other influences on the diffusion coefficient have also been studied, e.g., the influence of openings, such as pits in the cell walls (Kang, et al., 2008), or the influence of the moisture-induced swelling of the cell wall (Skaar & Babiak, 1982).

1.2.2 MEASUREMENT OF MOISTURE TRANSPORT

Moisture in wood has been assessed by diverse measurement techniques. The easiest and most common method is gravimetrical measurement. The weight of a sample at a certain condition is measured, and compared to the weight of the sample after oven-drying at 105 °C or at the condition of 0% relative humidity. The moisture content is then retrieved as the fractional difference in weight. Sorption curves are generally determined gravimetrically by changing the ambient relative humidity stepwise and awaiting equilibrium (Skaar, 1988; Time, 1998; Schellen, 2002; Wadsö, et al., 2004; Bratasz, et al., 2008; Forest Products Laboratory, 2010). By doing so, an equilibrium moisture content can be assigned to a certain relative humidity. On the other hand, the course of the moisture content of a sample during non-equilibrium conditions provides information about transport in the material. Transport properties can be determined from the moisture content over time in a variety of ways. By assuring one-dimensional transport, and assuming a constant diffusion coefficient, analytical solutions exist for a step change in the moisture content at one surface (Crank, 1975). The diffusion coefficient can then be retrieved from the moisture content over time (Time, 1998; Droin, et al., 1988; Droin-Josserand, et al., 1988; Allegretti & Ferrari, 2007; Uetimane Junior, et al., 2010). Diffusion coefficients can also be derived from sorption experiments

numerically by parameter optimization, i.e. by successive adjustment of parameters in numerical computations to better describe experimental results (Simpson & Liu, 1991; Avramidis, et al., 1992; Hukka, 1999; Kang, et al., 2009). Numerical determination is the only option in case more profound models are tested, e.g., with the transport of water vapor and bound water treated separately. Diffusion coefficients for the water vapor and bound water can then be retrieved from fitting the numerical model to the experimental data. A direct way to measure the bound water diffusion coefficient of the cell wall has been proposed by Stamm (1959), which relies on filling the lumens with a low-melting alloy of bismuth, lead, and tin, and performing sorption measurements.

Another method to determine the moisture content of wood is by measuring its electrical properties, which are influenced by the presence of moisture. The electrical resistivity of wood, for instance, decreases with increasing moisture content (Stamm, 1927). The moisture content can thus be determined by measuring the resistance between two electrodes inserted in the wood (Norberg, 1999). This method is quite accurate up to a moisture content of 50 %. The measurement error, however, increases with increasing moisture content (Frederiksson, et al., 2013). Alternatively, the moisture content of wood can also be measured by its dielectric properties (Skaar, 1988), although this method is used less in practice.

In the above described methods the moisture content of the sample as a whole is measured. Spatial information can only be derived by a priori assumptions on the transport mechanisms. The measurement of the moisture content locally provides more information about moisture transport. A straightforward and classical method to determine moisture content profiles is gravimetrically, by cutting the sample into thin slices and measure their weight before and after oven-drying (Simpson, 1993; Kang, et al., 2009). This is a tedious and time-consuming way of measuring, moreover it provides poor resolution. The main disadvantage, however, is that it is a destructive method. The sample can only be used once; this complicates the acquisition of transient moisture content profiles to a large extent. Non-destructive methods are therefore preferred. An example of a such a method is X-ray computed tomography (CT), which has been applied to wood to measure moisture content profiles during capillary absorption (Johansson & Kifetew, 2010), to determine the water vapor diffusion coefficient by numerical back-calculation (Danvind & Ekevad, 2006; Eriksson, et al., 2006), or to characterize the microstructure by measuring the local density (Lindgren, et al., 1992; Krähenbühl, et al., 2014). Another non-destructive method is neutron radiography, which has been used to study heat and consequent mass transfer in wood during one-sided heating (Gilani, et al., 2014). Nuclear Magnetic Resonance (NMR) is another example of a non-destructive measurement technique. It has the main advantage over the previous two methods that it can selectively probe nuclei, rather than measure the local density of the system.

Due to its non-invasive nature, NMR has been applied in multiple studies focusing on wood. The selective measurement of different nuclei enables determining the composition of wood by means of spectroscopic analysis (Maunu, 2002; Alesiani, et al., 2005; Santoni, et al., 2015), e.g., to characterize ancient wood (Viel, et al., 2004). It can also be used to determine the pore size distribution by means of cryoporometry (Mitchell, et al., 2008), using the dependence of the melting point of water on its confinement in a pore. The water resonance

intensity measured as a function of the temperature can then be converted to the pore size distribution using a reference sample. Furthermore, NMR has been applied to moisture in wood as related to, e.g., moisture absorption or drying (Menon, et al., 1987; Schellen, 2002; Merela, et al., 2009), moisture transport during daily relative humidity cycles (Hameury & Sterley, 2006), the study of coatings on wood (Ekstedt, et al., 2007; van Meel, et al., 2011), or the use of a portable magnet for in-situ, unilateral moisture content measurements in large boards (Casieri, et al., 2004), in a historical painting (Senni, et al., 2009), or beneath a coated wood surface (Dvinskikh, et al., 2011; Pourmand, et al., 2011; Johansson, et al., 2013). Moreover, it has also been used to identify different water types in wood. Several water components can exist in wood which can be distinguished with NMR: free water in the lumens, water vapor in the empty parts of the lumens, and bound water in the cell walls. A possibility to distinguish between these water components is the measurement of the ^{1}H and ^{2}H NMR spectrum during D_2O absorption in wood (Dvinskikh, et al., 2011). The absorbed water content is obtained from the ^{2}H NMR spectrum, and the macromolecular tissue density follows from the ^{1}H NMR spectrum. Another method is based on the different T_2 relaxation times of the water components in wood (Telkki, et al., 2013). Almeida et al. (2007) discriminate between liquid water in vessel elements (long T_2), liquid water in fiber and parenchyma elements (medium T_2), and bound or cell wall water (short T_2) in hardwood during desorption at varying equilibrium states. It is found that a loss of bound water occurs even at an equilibrium moisture content above the FSP, i.e. it takes place in the presence of liquid water. With the help of anatomical data of softwood, Menon et al. (1987) assign T_2 relaxation times to water in and on the cell wall, water in the ray and latewood tracheid lumens, and water in the earlywood tracheid lumens. The exchange of moisture between lumen and cell wall has been studied using 2D NMR by correlating T_2 relaxation times (Cox, et al., 2010). Furthermore, lumen water, bound water in cell walls, and wood polymer are distinguished by T_1-T_2 relaxation time correlation. The bound water can be divided in two different components based on T_1 relaxation times; mobile water in small voids and less mobile wood which swells the wood polymers. The relation between T_2 relaxation time and strain has more elaborately been assessed by Senni et al. (2010). A combination of unilateral NMR and a Bragg grating sensor is used to differentiate between strain regimes based on T_2 relaxation time.

When moisture content profiles over time are measured, the diffusion coefficient can more reliably be retrieved compared to sorption measurements, where only the total mass of the sample is measured. With the transient profiles, the diffusion coefficient can be determined, e.g., by numerical optimization to minimize the sum of squares of the deviation with the experimental moisture content profiles (Schellen, 2002). Also profound models can be tested with the measured moisture content profiles, e.g., multi-Fickian models with separate bound water and water vapor transport coupled by a sorption rate (Eitelberger, et al., 2011), where latter can be dependent on the moisture content (Dvinskikh, et al., 2011).

Several additional approaches exist to derive transport properties of porous media, which have not yet been applied to wood. The diffusion coefficient can, e.g., also be derived directly from transient moisture profiles, without numerical fitting of a model. First, application of the one-dimensional form of Eq. (1.1) in a mass balance results in

$$\frac{\partial \theta}{\partial t} = \frac{\partial}{\partial x}\left(D(\theta) \frac{\partial \theta}{\partial x} \right), \tag{1.2}$$

where t is time and x is the one-dimensional space coordinate. Eq. (1.2) can be integrated to obtain the moisture diffusion coefficient as a function of moisture content (Pel, 1995):

$$D(\theta) = \frac{\int_L^{x'} \left(\frac{\partial \theta}{\partial t} \right) dx}{\left(\frac{\partial \theta}{\partial x} \right)_{x'}}. \tag{1.3}$$

This approach has been applied successfully in the determination of the moisture dependent diffusion coefficient of various materials, such as brick and gypsum (Pel, 1995). Another method to derive the diffusion coefficient from moisture profiles during drying has been presented by Pel et al. (2002). An analytical solution describing the dynamics of a front entering a drying porous material is proposed. This front moves into the sample with a constant speed, which provides the diffusion coefficient by assuming a predefined exponential form. Diffusion coefficients for clay, gypsum, fired-clay brick, and sand-lime brick are determined accordingly.

An alternative method to derive transport properties of different porous media has been applied in numerous studies by Scherer and co-workers (Scherer, 1992; Vichit-Vadakan & Scherer, 2003; Scherer, et al., 2009; Zhang & Scherer, 2012). The method relies on the redistribution of liquid in the pores of a liquid-saturated porous beam when subjected to a three-point bending experiment. The mechanical response of the beam at constant deflection is thus influenced by the liquid flow. The time-evolution of the load, more specifically the load relaxation, therefore provides information about the permeability of the material. In addition, the experiment yields both the Young's modulus and Poisson's ratio of the material of interest.

1.3 HYGROMORPHIC BEHAVIOR OF WOOD

Moisture in wood is associated with macroscopic dimensional changes. A familiar example is the warping of a parquet floor when exposed to a high relative humidity (Blumer, et al., 2011), or the sealing of a liquid-filled barrel due to the expansion of individual planks. On the cellular scale, water molecules are adsorbed on sorption sites on the surface of cell wall constituents, mainly on the surface of hemi-cellulose. This forces the constituents apart, which is observed as macroscopic swelling of the material. During desorption, the opposite occurs: the material shrinks since water molecules are freed from their bonds to a sorption site, and the space between wood constituents is reduced. The highly anisotropic and inhomogeneous microstructure gives rise to differences in expansion in the three principal directions. The longitudinal alignment of the microfibrils results in more expansion in the tangential and radial direction than in the longitudinal direction (Skaar, 1988). Furthermore, almost all

expansion and shrinkage takes place in the hygroscopic range: above the FSP, hardly any dimensional change occurs.

A wide variety of experimental techniques has been used to study the deformation of wood as a result of a stepwise change in the ambient relative humidity. Displacement measurement gauges and an Electronic Speckle Pattern Interferometer have been used in the study of the dimensional changes in the three principal directions of a cubic beech wood sample during adsorption and desorption (Schellen, 2002). Chomcharn and Skaar (1983) perform experiments on wood wafers of three wood types during wetting and drying, where the dimensional changes are measured by a linear variable differential transformer (LVDT) mounted to a micrometer. Lanvermann et al. (2014) study the deformation field during moisture adsorption by analyzing high-resolution time-lapsed images using digital image correlation (DIC). DIC has also been applied in combination with confocal laser scanning microscopy to examine the microscopic swelling behavior of latewood (Murata & Masuda, 2006) Using phase contrast synchrotron X-ray tomography in combination with finite element calculations, Derome et al. (2012) study the swelling/shrinkage hysteresis of wood cell walls. NMR and X-ray microtomography are employed by Caré et al. (2012) to assess the influence of mesoscopic features (earlywood and latewood zones in growth rings) on the swelling strains during sorption tests. The local moisture content is measured by NMR, whereas the local swelling strains are determined by X-ray microtomography in combination with volumetric digital image correlation. Senni et al. (2010) assess the relation between moisture content and strain in silver fir samples; the moisture content is determined from measurements with a portable NMR probe, and simultaneously the expansion is obtained by a fiber Bragg grating optical sensor.

All aforementioned studies affirm the anisotropy in deformation of the three principal directions. In accordance with literature (Skaar, 1988), the largest deformation is observed in the tangential direction of the wood; the radial deformation is about 1.5-2.0 times smaller, and the axial deformation is negligible. Moreover the radial shrinkage is seen to be delayed in time compared to the tangential direction (Chomcharm & Skaar, 1983). Anisotropic swelling on the macroscale is a result of anisotropy on the microscale; the anisotropy of the cellulose fibrils arrangement in the cell wall layers results in an anisotropic swelling coefficient of the cell wall (Derome, et al., 2012). This also affects the expansion and shrinkage on an intermediate level, i.e. in high and low density areas (Caré, et al., 2012). Consequently the strain in the radial direction is found to be heterogeneous due to earlywood and latewood regions in this direction.

Anisotropy in expansion and shrinkage can also cause shape changes of a component, when differential expansion results in a bending moment. An elucidating example of such a hygromorphic effect in a natural system is the opening and closing of pine cones at different environmental conditions (Reyssat & Mahadevan, 2009). Due to the bilayered structure of the individual scales, a change in the relative humidity of the ambient air causes differential expansion of the two layers. As these two layers are firmly attached to each other, this will result in a bending moment, thereby opening the cone. This effect has recently been studied in light of hygromorphic biocomposites (Erb, et al., 2013; Le Duigou, et al., 2016), and electrically controllable soft actuators (Taccola, et al., 2015). The anisotropy of wood gives rise to similar effects, and has been exploited in architecture. An example is in the application

of wood boards in the construction of 19th century boathouses in Nordmøre, Norway (Larsen & Marstein, 2000). The walls of these boathouses are cladded with pine boards, nailed towards their upper edges. The anisotropy in expansion causes the boards of the boathouse to bend upwards during dry conditions, allowing natural ventilation through the façade. During humid conditions, the boards bend downwards, ensuring weathertight sealing of the façade. More recently, a prototype façade has been developed which reacts to environmental changes by the warping of individual thin wood slices constituting the façade (Reichert, et al., 2015). The effect may be amplified by adding a passive layer with different expansion to the active wood veneer, e.g., a polymer (Holstov, et al., 2015), thereby mimicking a pine cone or a bimetallic strip.

Bending in wood can also be caused by an asymmetric moisture content distribution. Similarly to a flat moisture content profile in a composite material, an asymmetric moisture content distribution in a homogeneous material causes unequal expansion over the thickness, which results in bending. This phenomenon has been studied during kiln-drying (Brandao & Perré, 1996; Allegretti, et al., 2003; Allegretti & Ferrari, 2007; Uetimane Junior, et al., 2010; Rémond, et al., 2013), and in the case of a board simulating a painted panel (Dionisi Vici, et al., 2006). Five of the six sides of a wood board are sealed, leaving only one surface exposed to the environment. A change in the exposure condition thus causes moisture transport, and consequently a curvature of the board which changes over time. The curvature has a maximum in time when the asymmetry in the moisture content distribution is maximal, after which the board becomes more flat. The time scale and magnitude of this process are dependent on the thickness of the board. Dionisi Vici et al. (2006) performed measurements on large Poplar panels with a thickness of 40 mm. This resulted in long-term experiments, necessitating an apparatus specifically designed for this purpose to measure the minor dimensional changes. The smaller thicknesses used in the kiln-drying experiments yield a more pronounced dimensional change, and the process is much faster. Latter may also be caused by the performance of measurements at high temperatures. Furthermore, curvature reversal at the end of the experiment is observed, i.e. the board is not straight again.

The relative humidity of the ambient air rarely changes stepwise, except in extreme cases, e.g., during flooding. Changes of environmental conditions are continuous, often manifested in daily or seasonally repeating cycles (Forest Products Laboratory, 2010). Knowing the hygromorphic response of wood under cyclically changing relative humidity has therefore a practical relevance. Gauvin et al. (2014) employ DIC to study the deformation field in wood during successive periods of low and high relative humidity, with special attention paid to the influence of anisotropy on the deformation. A similar block wave is used by Zhou et al. (1999) in their study on the creep behavior of a wood beam subjected to four-point bending. Ma et al. (2005) study radial and tangential dimensional changes by using a digital micrometer during triangular relative humidity waves. The aforementioned studies investigate the response of wood samples during block waves and triangular waves. Sinusoidal fluctuations are, however, more realistic, but studies concentrating on these conditions are rather scarce. Chomcharn and Skaar (1983) study the dimensional changes of wood wafers with a micrometer during exposure to sinusoidally varying relative humidity with cycling periods of 5.33, 10.67, 16.00, and 26.67 hours. Similarly, Yang and Ma (2014) assess the dynamic sorption and expansion of cylindrical poplar wafers during sinusoidal

fluctuations with periods of 1, 6, and 24 hours, at two different temperatures, 25 and 40 °C. The main scope of the study is the effect of temperature on the hygro-expansivity of the wood wafers. Schellen (2002) exposes cylindrical beech wood samples in an NMR setup to an air flow with a sinusoidally varying relative humidity, with periods of 12 and 24 hours. The tangential and radial deformations are recorded using resistance strain gages mounted to the sides of the cylinder.

1.4 OUTLINE OF THIS THESIS

The thesis starts in Chapter 2 with the description of a new method to determine the sorption curve of oak, relying on the approximation of its sorption behavior as a linear system. Exposure to a sinusoidal fluctuation in relative humidity is shown to provide the sorption curve. In Chapter 3 the moisture sorption and expansion frequency behavior of small cubic blocks is examined, and shown to follow a simple scaling law. Additionally, three-dimensional simulations are performed. Furthermore, the moisture transport in oak under dynamic exposure conditions is studied in detail using NMR, and experiments are performed to assess the relation between moisture content and expansion. Chapter 4 is concerned with shape change of an oak board under changes in the relative humidity. A model is introduced for the scaling of the involved behavior. Conclusions are drawn in Chapter 5, and an outlook for further study is provided.

2 DYNAMIC MOISTURE SORPTION

Many properties of materials are influenced by the presence of moisture. Moisture can cause softening of a material, expansion or shape changes (Blumer, et al., 2011), differences in electrical properties (Stamm, 1927), and provides a favorable environment for fungal growth in, e.g., gypsum (van Laarhoven, et al., 2015). It is therefore important to know how the relative humidity of the ambient air and the equilibrium moisture content in the material are related. This relation is characterized by the sorption curve, which is schematically shown in Figure 2.1. The boundary curves describe the moisture content of the sample when either adsorption starting from a relative humidity of 0 % or desorption from a relative humidity of 100 % is followed. The difference between these curves is attributed to sorption hysteresis, resulting in a non-unique relation between relative humidity and moisture content. The boundary curves should therefore rather be considered as bounding the region of possible moisture contents at a certain relative humidity. As a consequence, the moisture content follows an intermediate, so-called scanning curve when adsorption or desorption on the boundary curve is interrupted.

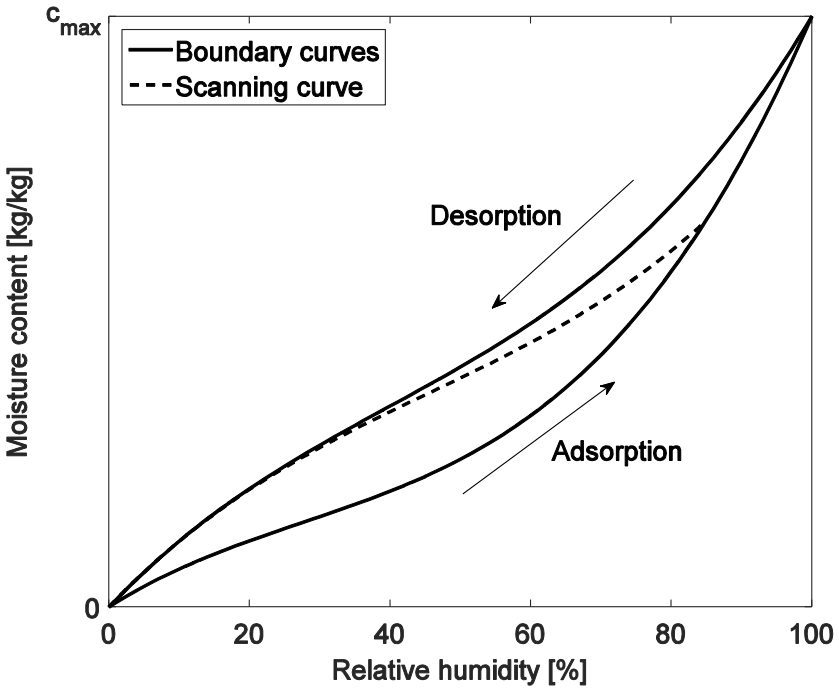

Figure 2.1: *A schematic example of a sorption curve describing the relation between relative humidity and moisture content of a material. The boundary curves bound with adsorption and desorption boundary curves and a scanning curve.*

The determination of the sorption curve is tedious and typically takes several weeks, dependent on the size of the sample (Wadsö, et al., 2004). In this section, a method is presented to obtain the sorption curve from a short experiment. It relies on exposing the sample to a sinusoidal relative humidity fluctuation. By assuming the sample to be a linear

system, its response to the dynamically changing relative humidity is shown to provide the sorption curve. Both equilibrium experiments and non-equilibrium experiments are performed to determine the sorption curve, and a comparison between the two is provided.

2.1 THEORY

Since no analytical solutions exist describing three-dimensional diffusion in a rectangular geometry, diffusion in a sphere is analyzed here. We consider a sphere with radius a, exposed to a step change in the moisture content at its surface. This problem can be formulated mathematically as

$$\begin{cases} r^2 \partial_t c = D \partial_r \left(r^2 \partial_r c \right), \\ c\left(r,0\right) = c_0, \\ \partial_r c\left(0,t\right) = 0, \\ c\left(a,t\right) = c_s, \end{cases} \tag{2.1}$$

where r is the radial coordinate, c the moisture content, D the constant diffusion coefficient, c_0 the initial moisture content, and c_s the moisture content imposed at the boundary. An analytical solution can be obtained by separation of variables (see, e.g., (Strauss, 2008) or (Crank, 1975)). The result can be formulated in the form of the Fourier series:

$$c\left(r,t\right) = c_s - \sum_{n=1}^{\infty} \frac{A_n}{r} \sin\left(g_n r\right) e^{-D g_n^2 t}, \tag{2.2}$$

with components

$$A_n = 2a \frac{c_0 - c_s}{\pi n} \left(-1\right)^n, \quad g_n = \frac{n\pi}{a}. \tag{2.3}$$

Eq. (2.2) can be integrated to obtain the evolution of the average moisture content of the sample c with its initial content $c_0 = 0$ as (Crank, 1975):

$$c\left(t\right) = c_s \left(1 - \frac{6}{\pi^2} \sum_{n=1}^{\infty} \frac{\left(-1\right)^n}{n^2} \mathrm{e}^{-D g_n^2 t} \right). \tag{2.4}$$

Note that, since we are dealing with a linear system, only the size of the imposed change is of interest, not its initial or final value. We may, therefore, consider c to be $c - c_0$. The moisture content can thus be described with an infinite sum of exponential terms. The sum quickly converges (Talbot & Kitchener, 1956), and hence the moisture content can be approximated by taking into account only the first few modes g_n. Sorption experiments have shown similar exponential evolution of the moisture content (Time, 1998; Wadsö, et al., 2004). It is

therefore assumed here that the response to a step change in the moisture content on the exposed surfaces of a cubic sample has the form

$$x(t) = \beta\left(1 - e^{-bt}\right), \tag{2.5}$$

with β the final moisture content, and b the sorption rate constant, which equals Dg_1^2. The influence of approximating Eq. (2.4) with only one mode, and with Eq. (2.5) is shown in Figure 2.2. Eq. (2.5) is seen to be a rather crude approximation of Eq. (2.4). Due to its simplicity, however, it will be used in the subsequent analysis to derive the sorption curve from the dynamic moisture content response of a sample. Note that the analysis can be extended to incorporate more modes, which, however, adds complexity to the solution. First the transfer function of the linear system needs to be determined. The transfer function $H(s)$ in terms of the complex variable s relates the input function and the system's response in the Laplace space (Franklin, et al., 1994):

$$X(s) = H(s)U(s), \tag{2.6}$$

where X and U are the Laplace transforms of the output and input function respectively. In our case, X is the Laplace transform of Eq. (2.5):

$$X(s) = \mathcal{L}\{x(t)\} = \beta\frac{b}{s(b+s)}. \tag{2.7}$$

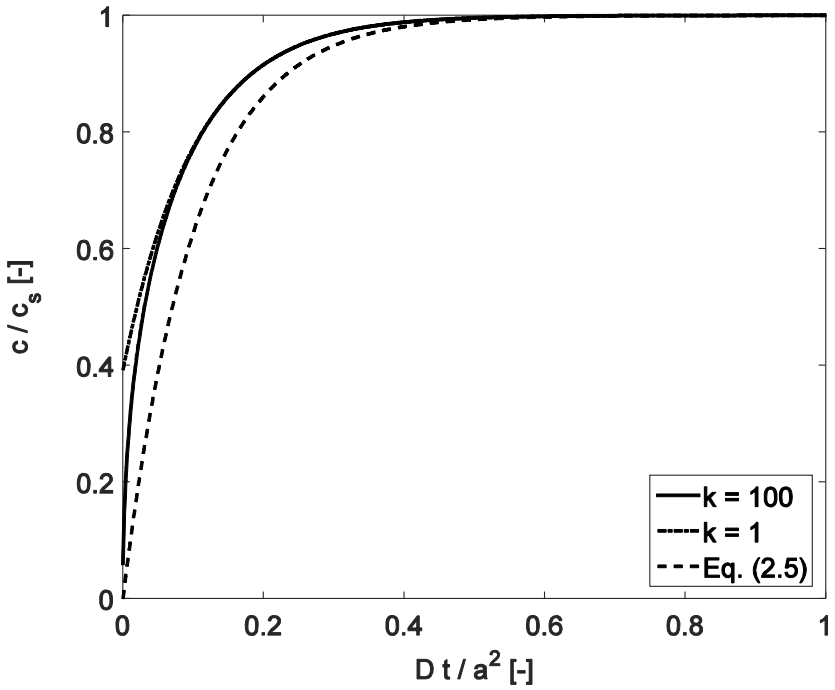

Figure 2.2: *Relative moisture content in a sphere with radius a as a function of the dimensionless variable Dt/a^2. The influence of the number of modes k in Eq. (2.4), as well as the approximation with the single exponential in Eq. (2.5) is shown.*

Eq. (2.5) is the time response to the step function in equilibrium moisture content $u(t) = \beta$. Note that β is the step in equilibrium moisture content which the sample eventually reaches. The transfer function $H(s)$ of the system is derived with the Laplace transform of the input function

$$U(s) = \mathcal{L}\{u(t)\} = \frac{\beta}{s}, \tag{2.8}$$

and with Eqs. (2.6), (2.7), and (2.8) to arrive at

$$H(s) = \frac{b}{b+s}. \tag{2.9}$$

With the transfer function known, the response of the system to any input function u with Laplace transform U can be determined by inverse Laplace transformation of Eq. (2.6). Here we are interested in the response of the system to the sinusoidal relative humidity variation

$$h(t) = h_0 + h_a \sin(\omega t), \tag{2.10}$$

where h_0 is the equilibrium value, h_a the amplitude, and ω the angular frequency. In the remainder of the text we will consider the fluctuation about h_0, i.e.

$$\xi(t) = h_a \sin(\omega t), \tag{2.11}$$

with $\xi = h - h_0$. In case of a linear relation between relative humidity and equilibrium moisture content, i.e. $m = e_1 h$, Eq. (2.11) results in a sinusoidal fluctuation of the equilibrium moisture content at the exposed surfaces of the sample:

$$m(t) = e_1 h_a \sin(\omega t). \tag{2.12}$$

Eq. (2.12) is first Laplace transformed and then multiplied with the transfer function H in Eq. (2.9). The inverse Laplace transform of the result yields the moisture content of the sample over time:

$$c(t) - c_0 = \mathcal{L}^{-1}\{H(s)M(s)\} = e_1 h_a \frac{b^2 \sin(\omega t) - \omega b \cos(\omega t)}{(b^2 + \omega^2)} + \frac{e_1 h_a b \omega}{(b^2 + \omega^2)} e^{-bt}. \tag{2.13}$$

Eq. (2.13) is plotted in Figure 2.3 to illustrate the typical time response of a sample with linear sorption. Several features are elucidated with this example. First of all, an exponentially decaying envelope of the sinusoidal response is seen, which is attributed to the last term in Eq. (2.13). Secondly, the response lags behind the imposed sinusoidal fluctuation, where the phase is dependent on the frequency. Finally, it is seen that the response reaches steady-state after some time, which is dependent on the ratio of the frequency ω and the time constant b.

In contrast to the analysis above, the relation between relative humidity and equilibrium moisture content is often non-linear. Although a purely sinusoidal relative

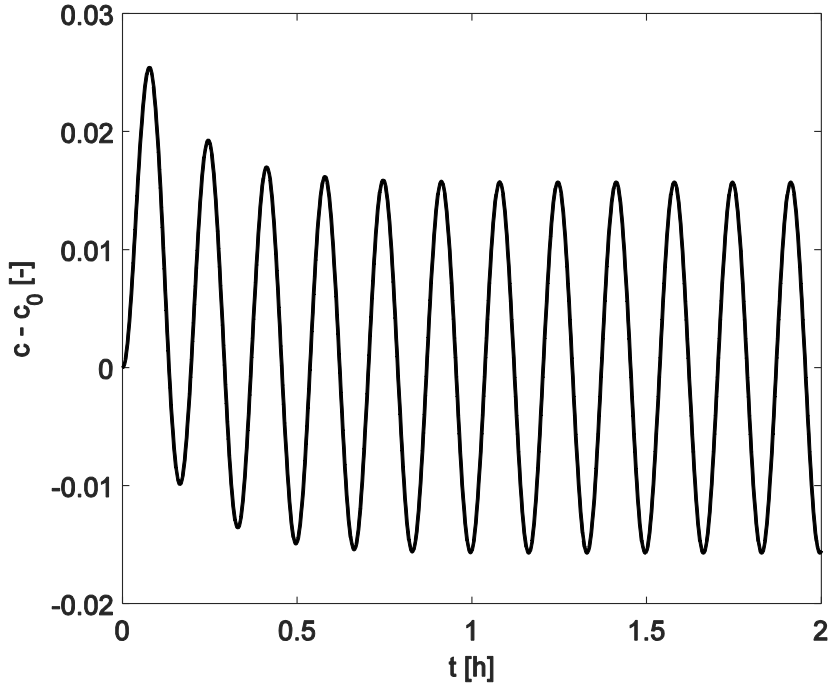

Figure 2.3: *The response of a system with a linear sorption curve to a sinusoidal fluctuation in relative humidity. Parameters used in the calculation of Eq. (2.13) are:* $e_1 = 0.2$, $h_a = 0.4$, $b = 1/600$, $\omega = 2\pi/600$.

humidity fluctuation of the ambient air is applied, the non-linearity of the sorption curve transforms the equilibrium moisture content fluctuation. The analysis is therefore extended to include a non-linear sorption curve. Let us first assume a third-order polynomial with zero constant term for the sorption curve as

$$c_{eq}(h) = e_3 h^3 + e_2 h^2 + e_1 h, \tag{2.14}$$

with e_1, e_2, and e_3 constants. We impose the condition that the sorption curve passes through (h_0, c_0), with $c_0 = c_{eq}(h_0)$, i.e. the initial equilibrium moisture content. With this condition we obtain an expression for e_1 in terms of the other variables:

$$e_1 = \frac{c_0}{h_0} - e_2 h_0 - e_3 {h_0}^2. \tag{2.15}$$

Eq. (2.14) is transformed with respect to h_0, such that we have

$$c_{eq}^0(\xi) = e_3 \xi^3 + \gamma_2 \xi^2 + \gamma_1 \xi, \tag{2.16}$$

with

$$\gamma_1 = \frac{c_0}{h_0} + e_2 h_0 + 2 e_3 {h_0}^2, \qquad \gamma_2 = e_2 + 3 e_3 h_0. \tag{2.17}$$

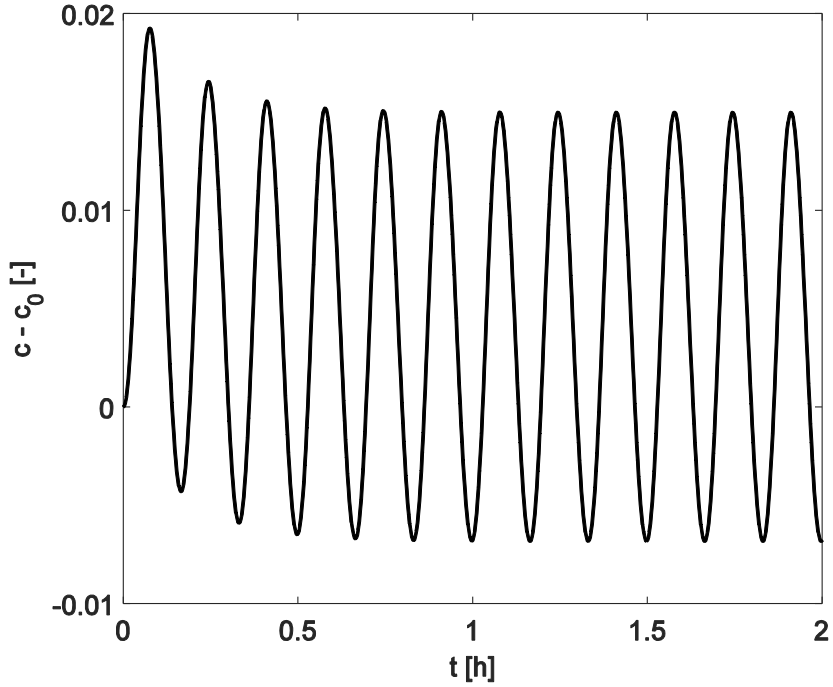

Figure 2.4: *The response of a system with a non-linear sorption curve to a sinusoidal fluctuation in relative humidity. Parameters used in the calculation of Eq. (2.19) are:* $h_0 = 0.5$, $h_a = 0.4$, $c_0 = 0.1$, $e_2 = -0.1$, $e_3 = 0.1$, $b = 1/600$, $\omega = 2\pi/600$.

Eq. (2.11) can be inserted into Eq. (2.16), which yields the time-evolution of the equilibrium moisture content:

$$m(t) = e_3 h_a^{\,3} \sin^3(\omega t) + \gamma_2 h_a^{\,2} \sin^2(\omega t) + \gamma_1 h_a \sin(\omega t). \tag{2.18}$$

Eq. (2.18) can be rewritten and its Laplace transform is then multiplied with the transfer function H in Eq. (2.9). The inverse Laplace transform of the resulting product provides the evolution of the moisture content over time as

$$\begin{aligned} c(t) - c_0 = {} & \mathcal{L}^{-1}\{H(s)M(s)\} = \\ & \frac{\gamma_2 h_a^{\,2}}{2} - e_3 h_a^{\,3} b \frac{b\sin(3\omega t) - 3\omega\cos(3\omega t)}{4\left(b^2 + 9\omega^2\right)} - \gamma_2 h_a^{\,2} b \frac{b\cos(2\omega t) + 2\omega\sin(2\omega t)}{2\left(b^2 + 4\omega^2\right)} \\ & + h_a b\left(3e_3 h_a^{\,2} + 4\gamma_2\right)\frac{b\sin(\omega t) - \omega\cos(\omega t)}{4\left(b^2 + \omega^2\right)} \\ & + h_a \omega e^{-bt} \frac{\left[\begin{array}{l} \gamma_2 b^5 - 2\gamma_1 h_a b^4 \omega + b^3\omega^2\left(6e_3 h_a^{\,2} + 13\gamma_2\right) - \\ 20\gamma_2 h_a b^2 \omega^3 + b\omega^4\left(24e_3 h_a^{\,2} + 36\gamma_2\right) - 18\gamma_1 h_a \omega^5 \end{array}\right]}{\left(b^2 + 9\omega^2\right)\left(b^2 + 4\omega^2\right)\left(b^2 + \omega^2\right)}. \end{aligned} \tag{2.19}$$

A plot of Eq. (2.19) is provided in Figure 2.4. The same characteristic, exponentially decaying envelope is seen, as well as a steady-state fluctuation after the exponential term has decayed.

In contrast to Eq. (2.13), however, the steady-state solution is not a sinusoidal fluctuation around the zero line with a phase shift. The first term in Eq. (2.19) causes the response to be around an equilibrium position other than 0 for a non-linear sorption curve.

Although Eq. (2.19) is rather excessive, note that it contains merely 3 unknown variables: b, e_2, and e_3. By fitting the evolution of the moisture content of a sample with Eq. (2.19), initially in equilibrium at a relative humidity h_0 and moisture content c_0, the variables b, e_2, and e_3 can be retrieved. Eqs. (2.14) and (2.15) then provide the sorption curve.

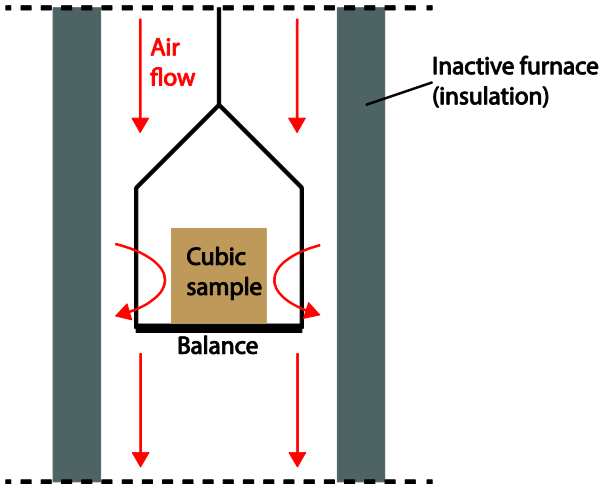

Figure 2.5: *Schematic representation of the thermogravimetrical analyzer (TGA). A cubic sample is placed on a balance in an insulated shaft, through which air can be blown. The mass of the sample is continuously measured, which can be back-calculated to the moisture content.*

2.2 MATERIALS AND METHODS

A cubic oak sample with sides of 4 mm is prepared from a large oak board. The sample is used to determine the sorption curve in an equilibrium experiment, as well as during non-equilibrium conditions using the proposed analysis. In both experiments, the mass of the sample is measured gravimetrically using a Mettler Toledo thermogravimetrical analyzer (TGA) TG50. The original purpose of a TGA is the measurement of the mass of a sample as a function of temperature. The TGA consists of a cylindrical shaft inside a furnace, which contains a balance on which a sample can be placed. For our purpose, the control of temperature is not needed, therefore the furnace is inactivated and is merely used as insulation for the shaft containing the balance, as is shown in Figure 2.5. Air can be blown through the shaft, which is employed to vary the relative humidity inside the shaft. To this end a humidifier is used, which generates a continuous air flow with adjustable relative humidity.

The working principle of the humidifier is schematically shown in Figure 2.6. Compressed air is first dried by a membrane dryer, which is verified by the color of silica gel beads, embedded in a connected chamber. The dehumidified stream is then divided over two

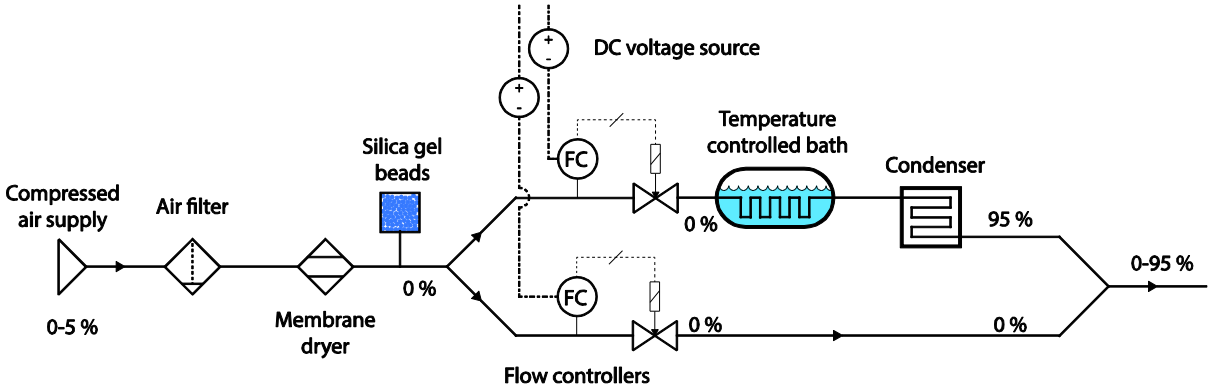

Figure 2.6: *A schematic representation of the humidifier. Compressed air is filtered and dried, after which the air stream is divided over two parallel circuits. One stream is humidified, while the other one remains dry. The mixing proportions of the two streams, controlled by applying a voltage to a flow controller (FC), determine the relative humidity of the air.*

Bronkhorst© flow controllers, with which the flow can be set. One of the air streams is conducted through tubing with semi-permeable sides, embedded in a temperature controlled bath, to moisten the air. After leaving the bath, the air stream is conducted through a condenser to avoid formation of liquid droplets. Both streams are mixed to produce a uniform flow with a relative humidity

$$RH = \frac{V_{wet}}{V_{wet} + V_{dry}}, \tag{2.20}$$

where V_{wet} and V_{dry} are the wet and dry flow respectively. A more elaborate description of the humidifier and the calibration procedure is given in Appendix A.

The computer-controlled flow controllers allow not only step changes in the relative humidity of the air flow; a continuously changing relative humidity is also feasible. The course of the relative humidity can thus be varied as any desired function. In this study, the relative humidity will be varied stepwise to determine the equilibrium sorption curve, and sinusoidally to acquire the sorption curve from dynamic experiments. The moisture content of the sample c at a relative humidity h is derived from the mass of the sample w as

$$c(h) = \frac{w(h) - w_0}{w_0}, \tag{2.21}$$

where w_0 is the mass of the sample at a relative humidity of 0 %.

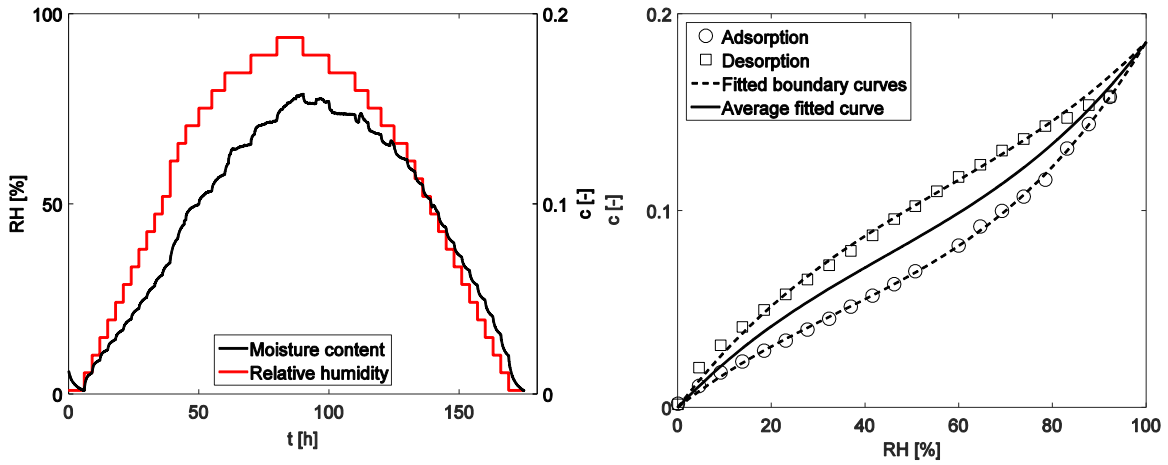

Figure 2.7: *Relative humidity and measured moisture content over time during the equilibrium experiment (left), and the resulting sorption curve (right).*

2.3 RESULTS AND DISCUSSION

Figure 2.7 shows the result of the equilibrium sorption series to determine the sorption curve. The relative humidity of the air flow is changed in discrete steps. Since the relative humidity of the air flow is preprogrammed, and no feedback from the TGA is obtained, the sample is often not in equilibrium at the time the relative humidity is changed. The moisture content step response is therefore fitted with a sum of exponentials, the asymptote of which provides the equilibrium moisture content for each step. The sorption curve is determined for both adsorption and desorption, which results in the hysteresis loop shown in Figure 2.7, with a higher moisture content at the same relative humidity during desorption compared to adsorption. Since the humidifier is not able to reach a relative humidity of 100 %, the sorption curve can only be determined up to a relative humidity of 95 %. As a result, the moisture content at high relative humidity is not captured, which is often seen to increase strongly above 95 % (Time, 1998). Another consequence is that the subsequent desorption curve is not the boundary desorption curve, i.e. the maximum moisture content during desorption, but an intermediate, so-called scanning curve.

To compare the sorption curve from the equilibrium experiment to the curves from dynamic experiments, an average sorption curve is calculated from the adsorption and desorption curve. Both curves are fitted with the cubic polynomial in Eq. (2.14). The fact that the desorption curve is not a boundary curve is incorporated by including only the experimental points up to a relative humidity of 70 % in the fitting, and adding the stringent condition that the curve should reach the fitted adsorption curve at a relative humidity of 100 %. The mean of the two fitted cubic polynomials is taken as the average sorption curve, which is also shown in Figure 2.7.

Experiments are performed with a sinusoidally varying relative humidity in different relative humidity ranges (10-50%, 30-70%, 50-90%, and 10-90%) and at different frequencies (periods of 4, 8, 16, and 32 minutes). An example of the moisture content evolution during a sinusoidal variation in relative humidity is shown in Figure 2.8. The moisture content of the sample varies sinusoidally with an exponentially decaying envelope, as expected from the

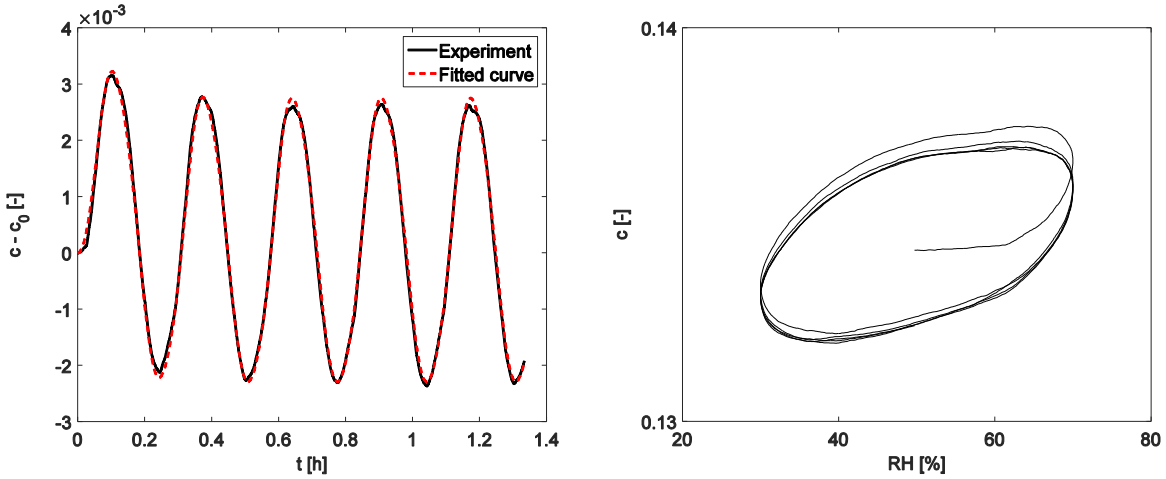

Figure 2.8: *An example of the moisture content evolution during a sinusoidal relative fluctuation of 50 ± 20 %, with a period of 16 minutes (left), and the moisture content as a function of the ambient relative humidity in the same dynamic experiment (right).*

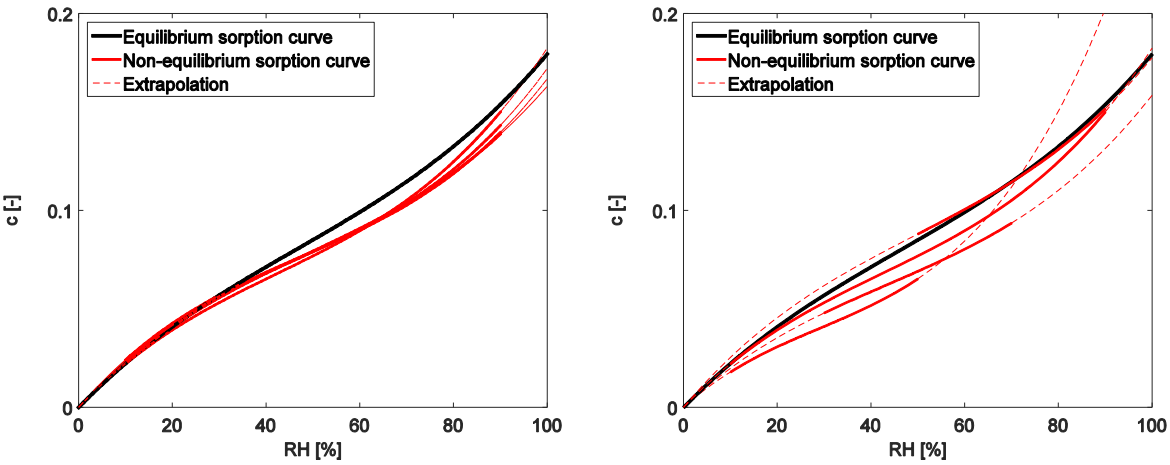

Figure 2.9: *Sorption curves derived from non-equilibrium experiments in the same relative humidity range (50 ± 40 %) at different frequencies (left), and in different relative humidity ranges at the same frequency (period of 16 minutes). The sorption curve in the relative humidity range of the experiment is indicated by the solid red line, extrapolated parts are dotted.*

theory. Furthermore, the fluctuation is not about the zero line, which implies a non-linear sorption curve. The fit with Eq. (2.19) is seen to be fairly accurate, despite some minor deviations.

Two sorption curves derived from the experiments are shown in Figure 2.9. Good agreement is found between the sorption curves determined from the non-equilibrium experiments in the same relative humidity range (10-90%) and the average equilibrium sorption curve. The non-equilibrium sorption curve slightly underestimates the average curve, which is most probably caused by the stringent condition that the sorption curve from the non-equilibrium experiment should pass through (h_0, c_0), i.e. the condition of the sample before the experiment. Since the sample was dried before the experiments, the initial condition of the

sample in the sequence is likely to be different than the average sorption curve. This is also reflected in the sorption curves derived from the non-equilibrium curves in different relative humidity ranges, but at the same frequency. The initial condition is seen to highly affect the derived sorption curve: the curves derived from experiments in the relative humidity ranges 50 ± 20 % and 50 ± 40 % are seen to have different initial points, despite their same equilibrium relative humidity. The experiments were performed subsequently, without drying the sample after each experiment. During the dynamic experiments, sorption hysteresis causes the moisture content of the sample to deviate from a single sorption curve. This is also shown in Figure 2.8, where the moisture content during a sinusoidal fluctuation is seen to follow an ellipsoid shape rather than a curve.

The single exponential form of the step response of the system is seen to describe the moisture content of the sample following a step change in the relative humidity only to a certain extent, as shown in Figure 2.10. A more accurate fit to the moisture content evolution can be obtained by incorporating a second exponential term in Eq. (2.5). This, however, adds more complexity to the analysis and results in an even more extensive expression for the fitting function. Moreover, it results in more fitting variables, which not necessarily results in a more accurate sorption curve. Another source of discrepancies can be the assumption of a constant sorption rate. In other words, the sample is assumed to behave linearly in its moisture sorption. The response is assumed to be independent of the initial or final condition, only the size of the change is of interest. This has been contradicted in several studies (Wadsö, 1994), where sorption is found to be slower at high relative humidity. The approach taken in this study is therefore a simplification of the sorption process, which may result in deviations.

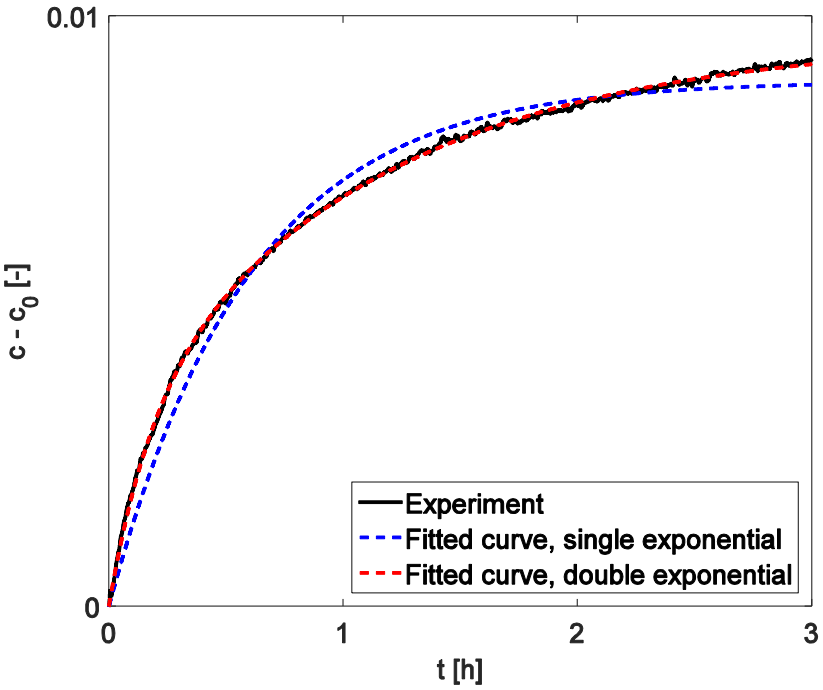

Figure 2.10: *An example of the moisture content evolution of the cubic sample due to a step change in relative humidity. Fitted exponential curves are shown with one and with two components.*

The derived equilibrium sorption curve is an average curve for both adsorption and desorption, similarly to the average sorption curve from the equilibrium experiment in Figure 2.7. In the derivation of the sorption curve from dynamic experiments, however, the condition is used that the curve should pass through (h_0, c_0), i.e. the condition of the sample before the experiment. This initial condition is dependent on the sorption history of the sample; if the sample is dry before the experiment, the point (h_0, c_0) will be on the adsorption boundary curve, if the sample is initially wet, (h_0, c_0) will be on the desorption curve. The derived equilibrium sorption curve will therefore be dependent on its initial condition. This is not the case for the average of the boundary adsorption and desorption curves in Figure 2.7.

2.4 CONCLUSIONS

A method is presented to derive the equilibrium sorption curve from a short non-equilibrium experiment. It relies on the approximation of the sample as a linear system, such that the response to any exposure function can be determined by its transfer function. The theoretical analysis shows that the moisture content evolution during a sinusoidal relative humidity fluctuation can be fitted to obtain the equilibrium sorption curve. Good qualitative agreement with the sorption curve from the equilibrium experiment is found for experiments in different humidity ranges and at different frequencies. Discrepancies are caused by the condition that the sorption curve should pass through the initial condition of the sample, i.e. through the point (h_0, c_0). The derived sorption curve is therefore dependent on the sorption history of the sample.

Nevertheless, the proposed method provides a fast means of acquiring a first order approximation of the sorption curve. To verify the method, experiments with other hygroscopic materials should be conducted. Particularly interesting is whether the method is applicable to both highly hygroscopic materials (e.g., other wood species or gypsum) and materials with hardly any moisture sorption in the hygroscopic range (e.g., brick).

3 FREQUENCY-DEPENDENCE OF MOISTURE SORPTION AND HYGRO-EXPANSION

We present a combination of experimental methods and numerical modeling to investigate the sorption and hygro-expansive frequency behavior of oak wood. The frequency dependence of moisture content and expansion, and the influence of sample size are assessed in a series of experiments where the moisture content and the one-dimensional expansion of two equally sized sample are measured simultaneously. The experiments are simulated numerically using COMSOL. The one-dimensional moisture penetration depth during sinusoidal relative humidity fluctuations is then investigated non-invasively using Nuclear Magnetic Resonance (NMR). In a different set of experiments, a combination of NMR and an optical fiber displacement sensor is employed to concurrently measure properties of the water-wood system and one-dimensional expansion.

3.1 THEORY

To relate the frequency behavior of samples with different sizes, we first consider the diffusion equation in a sphere with radius a with a constant concentration at the surfaces, as introduced in Section 2.1. The moisture content c of the sphere after a step change at its boundaries to a moisture content c_s can then be described by Eq. (2.4) as

$$c(t) = c_s\left(1 - \frac{6}{\pi^2}\sum_{n=1}^{\infty}\frac{(-1)^n}{n^2}\mathrm{e}^{-Dg_n{}^2 t}\right),$$

with D the diffusion coefficient and g_n the n$^{\text{th}}$ mode. The moisture content of the sample is approximated by the first mode, neglecting the higher modes. Furthermore the initial moisture content is assumed to be zero. Note that, since we are dealing with a linear system, only the size of the imposed change is of interest, not its initial or final value. We may, therefore, consider c to be $c - c_0$, with c_0 the initial moisture content. We again assume that the step response can be described with Eq. (2.5), which is repeated here for convenience:

$$x(t) = \beta\left(1 - e^{-bt}\right),$$

with x the response to a step change β in the moisture content at its exposed surfaces, and b the reciprocal of the characteristic time scale τ, with

$$b = D\frac{\pi^2}{a^2}. \tag{3.1}$$

Using the system's transfer function $H(s)$ in Eq. (2.7), its frequency behavior can be determined by considering $H(j\omega)$. The amplitude as a function of the angular frequency ω can then be obtained by the length of $H(j\omega)$ in the complex plane, which reads

$$A(\omega) = \beta \frac{b}{\sqrt{b^2 + \omega^2}}. \tag{3.2}$$

If we introduce the frequency $f = \omega/2\pi$, we can rewrite Eq. (3.2) as

$$A(f) = \beta \frac{b}{\sqrt{b^2 + 4\pi^2 f^2}}. \tag{3.3}$$

To determine the inflection point of Eq. (3.2), its first and second derivatives are calculated as

$$A'(f) = -\frac{4\pi^2 \beta b f}{\left(b^2 + 4\pi^2 f^2\right)^{\frac{3}{2}}}, \quad A''(f) = -\frac{4\pi^2 \beta b \left(b^2 - 8\pi^2 f^2\right)}{\left(b^2 + 4\pi^2 f^2\right)^{\frac{5}{2}}}. \tag{3.4}$$

The second derivative in Eq. (3.4) has a root at $f = \sqrt{b^2}/8\pi^2$. With Eq. (3.1) we can relate this inflection point to the diffusion coefficient D and the radius of the sphere a as

$$f_{inf} = \frac{\pi D}{2a^2\sqrt{2}}. \tag{3.5}$$

From this expression, a dimensionless frequency can be deduced as

$$f^* = \frac{f a^2}{D}. \tag{3.6}$$

The inflection point in the scaled amplitude is accordingly located at $f^* = \pi/2\sqrt{2}$. With Eq. (3.6) we find the amplitude as a function of the dimensionless frequency f^* by substitution in Eq. (3.3):

$$B(f^*) = \beta \left[1 + 4\left(\frac{f^*}{\pi}\right)^2\right]^{-\frac{1}{2}}. \tag{3.7}$$

The moisture content amplitude as a function of frequency of different samples can thus be scaled with the dimensionless frequency based on their size and diffusion coefficient using Eq. (3.6). A familiar way to visualize amplitude-frequency relations in the field of dynamic systems is by means of a Bode amplitude plot (Franklin, et al., 1994). The Bode plot of Eq. (3.7) is shown in Figure 3.1 with $\beta = 1$. Three dimensionless frequency regions can be distinguished. For low f^*, i.e. for $f a^2 << D$, the amplitude is seen to be constant, since transport is faster than the imposed moisture content changes at the boundary. For $f a^2 \approx D$, an inflection in the amplitude is observed towards lower values, due to the same time scale of the

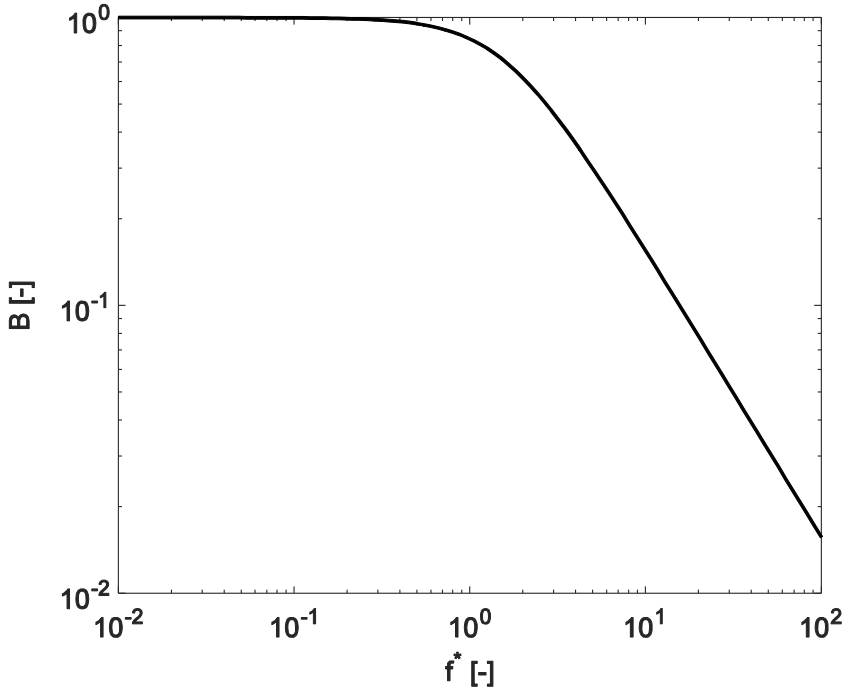

Figure 3.1: *Amplitude as a function of the dimensionless frequency for diffusion in a sphere.*

imposed changes and the transport in the material. In the final region, for $f\,a^2 >> D$, the changes are faster than transport and a decline in amplitude is seen since the sample cannot equilibrate, with a slope of -1 on the logarithmic scale.

In the experiments, cubic block are used instead of spheres. A conversion is therefore introduced to account for the different shape. The most simple and obvious is $d = 2a$, with d the length of the side of the cubic sample. This, however, results in the sphere being smaller in volume than the cubic geometry considered in the experiments. Another relation between the radius a and d is therefore introduced, based on an equality in volume, resulting in $d = a\,\sqrt[3]{4\pi/3}$. Latter conversion will be used in the calculations of the diffusion coefficient from the experimental Bode plots.

In wood, a change in the moisture content is associated with a change in dimension. If we consider a sphere again, the change in radius Δr due to a change in the moisture content c-c_0 can be written as

$$\Delta r = \alpha r\left(c - c_0\right), \tag{3.8}$$

where α is the linear hygroscopic expansion coefficient. Eq. (3.8) describes the radius change of a sphere with a uniform moisture content. Although the deformation of a cube due to local moisture-induced expansion is complex and governed by multiple mechanical properties, here the expansion is assumed to follow the simple relation

$$\varepsilon = \alpha\left(c - c_0\right). \tag{3.9}$$

The expansion is directly related to the moisture content and thus has the same time constant, meaning it is assumed to have the same frequency behavior. As a consequence, the scaling as derived above is applicable to the expansive frequency behavior as well.

The scaling in Eq. (3.6) also follows from the similarity solution at short times. Under these conditions, the medium can be considered semi-infinite and solutions to the diffusion equation can be found in terms of the dimensionless variable

$$\eta = \frac{x}{\sqrt{Dt}}, \tag{3.10}$$

with x the space variable. The moisture content $c(x,t)$ can then be described by $g(\eta)$, i.e. moisture content profiles are scaled by space and time. Qualitatively this can be interpreted as follows: for η smaller than the sample size, the moisture content of two samples will be similar if the scaled penetration depth η is equal. A larger sample will have a similar moisture content profile as a small sample after a time proportional to d^2. Note the resemblance between Eqs. (3.10) and (3.6), with the frequency as the reciprocal of a characteristic time scale.

3.2 MATERIALS AND METHODS

3.2.1 MATERIAL

Cubic oak blocks are prepared from a large board, with different dimensions (sides of 2, 4, 6, 8, and 10 mm on the sides), for the frequency dependent sorption and expansion experiments. From the same board, cylindrical samples with two different sizes are prepared for the NMR measurements. One batch is prepared with a diameter of 10 mm and a height of 30 mm, and one batch with a diameter of 20 mm and a height of 10 mm. Prior to the experiment, the sample of interest is placed in a desiccator over a saturated salt solution, ensuring a relative humidity close to the equilibrium relative humidity of the experiment. Nevertheless, in each experiment an equilibration time is taken into account before the change in exposure condition. The sample is hence in equilibrium before the actual experiment.

3.2.2 MOISTURE CONTENT AND EXPANSION

The moisture content and expansion of small blocks is measured simultaneously on two equally sized samples, exposed to the same condition. To this end, an experimental set-up is constructed which consists of a thermogravimetric analyzer (TGA), a thermomechanical analyzer (TMA), and a humidifier to generate an air flow with adjustable relative humidity. The humidifier and the TGA have been introduced in Section 2.2, the TMA will shortly be described here.

The air flow leaving the humidifier is divided over two parallel circuits. One of these circuits concerns the gravimetric measurement of the mass of the sample using the TGA. The other part of the air flow leaving the humidifier is blown over a sample placed under a probe of fused silica, which is part of a Mettler Toledo TMA/SDTA 841e system. Similarly to the

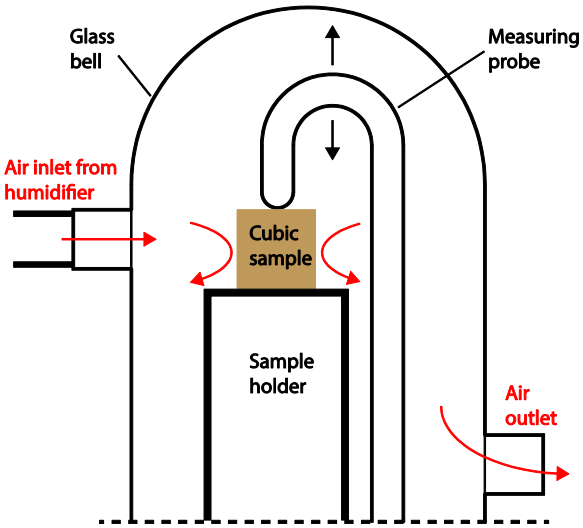

Figure 3.2: *Schematic representation of the thermomechanical analyzer (TMA). A cubic sample is placed on a sample holder, under a measuring probe, which detects the change in height by a linear variable differential transformer. A glass bell with an inlet for air from the humidifier is placed over the sample to ensure a closed environment.*

TGA, the furnace of the TMA system is inactivated, and merely its probe is used to measure the local one-dimensional deformation accurately, as shown in Figure 3.2. A custom-made glass bell is placed over the sample holder to create a closed environment. The probe is placed in the middle of the top surface of the sample in all experiments. Moreover, the sample is oriented such that tangential expansion is measured. The length change of the sample during the experiment is then determined by the height change of the probe, by means of a linear variable differential transformer, with an accuracy of ~10 nm. After the experiment, the samples used for expansion and moisture content measurement are oven-dried. The moisture content of the sample is back-calculated using Eq. (2.21), and the expansion ε can be determined as

$$\varepsilon(h) = \frac{l(h) - l_0}{l_0}, \tag{3.11}$$

where l is the length of the sample at a relative humidity h and l_0 is the dry length.

3.2.3 NUMERICAL SIMULATIONS

Numerical simulations are performed to determine the influence of various parameters on the frequency behavior of cubic oak blocks. To this end, a three-dimensional linear elastic model is developed in COMSOL which simulates the moisture transport in the sample and the resulting deformation field due to local moisture-induced dimensional changes. To resemble the experiments, a square cubic block is built which is supported on its bottom surface. This is implemented in the model as a boundary condition which states that the corner points of the bottom surface cannot translate in the z-direction. Furthermore, one corner point is fixed in x- and y-direction as well as a reference point. In the model, moisture transport is described with the diffusion equation, with a sinusoidally varying prescribed moisture content at the

boundaries, following the average sorption curve in Figure 2.7. Several combinations of parameters are tested in the numerical experiments. First computations are performed assuming the material to be isotropic in both moisture transport and mechanical properties. The influence of the magnitude of the diffusion coefficient is assessed. Subsequently, the diffusion coefficient is presumed dominant in one direction, but all mechanical properties are isotropic. Finally, simulations are performed with parameters proposed by Saft and Kaliske (2013), where first average, constant values are used in an anisotropic model, after which the values are presumed to be dependent on moisture content.

The mesh size is chosen dependening on the frequency of the relative humidity fluctuation, the size of the sample, and the chosen diffusion coefficient for the specific numerical experiment. Either fast fluctuations, a relatively large sample, or a low diffusion coefficient result in a minor penetration of moisture into the sample; a finer mesh is therefore required to describe the small consequential changes in moisture content and deformation. In each sequence with the same transport and mechanical properties, simulations with the largest sample size and highest frequency are repeated with increasingly finer meshes to determine the necessary fineness of the mesh.

3.2.4 NMR

The key concept of NMR is that nuclei (e.g., ^{1}H, ^{13}C) possess spin, and consequently have a magnetic dipole moment. In an externally applied magnetic field B_0, these nuclei precess at a resonance frequency

$$f_L = \gamma B_0, \tag{3.12}$$

where γ is the gyromagnetic ratio of the nucleus (for ^{1}H, $\gamma/2\pi$ = 42.58 MHz/T). This resonance condition allows the selective measurement of nuclei in an NMR experiment by applying suitably chosen radiofrequency (RF) pulses. Moreover, when a gradient in the static field is applied, the resonance condition can be made spatially selective. Accordingly, the moisture content at different spatial positions can be determined by changing the resonance frequency f_L.

The magnetic moments of the nuclei can be manipulated by applying RF pulses at the resonance frequency. The amplitude of the detected signal after manipulation is proportional to the amount of nuclei participating in an experiment. After an RF pulse, however, the amplitude of the signal decays due to two relaxation mechanisms: spin-lattice or longitudinal relaxation, characterized by a relaxation time T_1, and spin-spin relaxation, with a relaxation time T_2. These T_1 and T_2 relaxation times reflect the rate at which longitudinal magnetization is restored and transverse magnetization decays respectively, and provide valuable information about the system under consideration. With these relaxation times, the signal intensity of the spin-echo signal can be described by (Vlaardingerbroek & Den Boer, 2003):

$$S \approx S_0 \left(1 - e^{-\frac{T_R}{T_1}} \right) e^{-\frac{T_E}{T_2}}, \tag{3.13}$$

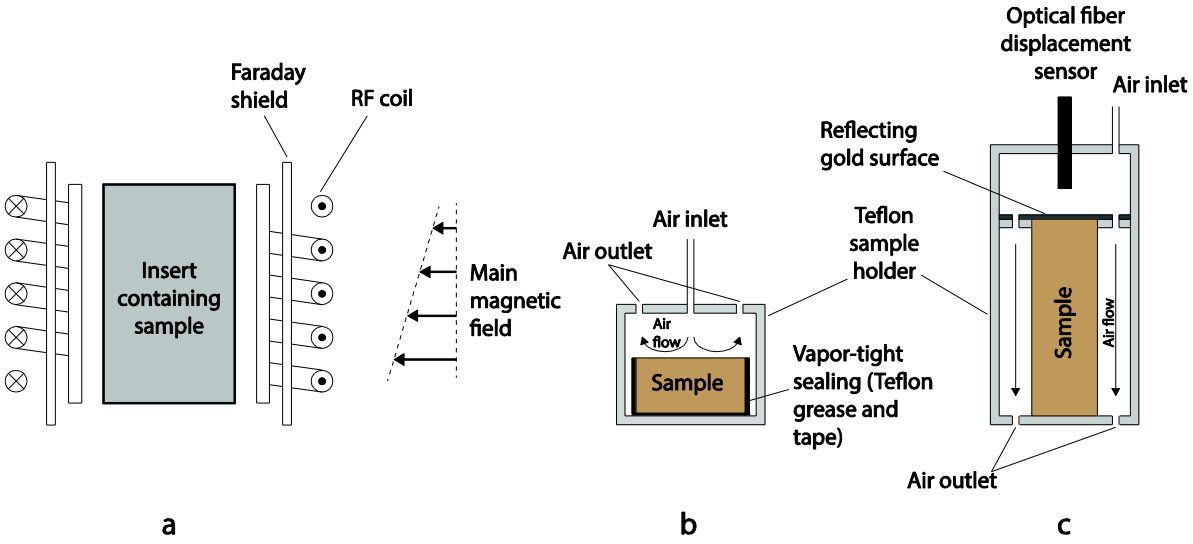

Figure 3.3: *a) NMR set-up as used in the experiments, cross-section of insert to b) assess 1D moisture transport, and c) moisture sorption and consequent 1D expansion.*

where S_0 is the initial spin-echo signal, T_R the repetition time, and T_E the echo time. In case $T_R > 4T_E$, the contribution of spin-lattice relaxation on the signal intensity can be neglected. Latter condition holds in all experiments performed in this study (T_1 ~60 ms, T_R = 1 s), consequently the signal decay provides the T_2 of the moisture in the sample. The magnetization decay of bulk water is mono-exponential, giving rise to a single T_2 value. In a porous system, however, T_2 is most often not a single value but a distribution of relaxation times. Furthermore, T_2 values in porous media are generally lower than values of bulk water. Both characteristics are caused by the moisture being present in a distribution of pore sizes, giving rise to different relaxation times. In their model, Brownstein and Tarr (1979) relate T_2 to pore size by assuming that magnetization can decay due to a surface-like sink. For increasing surface-to-volume ratio, the magnetization will decay at a higher rate, i.e. the T_2 value is lower. By assuming some standard geometries (planar, cylindrical, spherical), a relation between pore size and T_2 can be established. This model has been applied, e.g., to determine pore size distributions (Mitchell, et al., 2008), or to describe the pore water distribution during drying (Valckenborg, et al., 2001).

The experiments described in this study are performed on a custom-built NMR system, specifically designed for quantitative measurement of moisture in porous materials. The system operates with a static magnetic field of 0.78 T, using a magnetic field gradient of ~0.3 T/m in the vertical direction generated with Anderson coils (Valckenborg, et al., 2001). The set-up is shown schematically in Figure 3.3a. A Teflon sample holder containing the sample of interest is placed inside a coil to transmit and receive RF fields during the NMR experiments. A Faraday shield is placed between the coil and the sample to suppress the effects of a varying dielectric permittivity induced by moisture content changes, thereby enabling quantitative measurement.

Two different types of experiments are performed. The one-dimensional moisture transport is assessed using the insert shown in Figure 3.3b. To this end, cylindrical samples with a diameter of 20 mm and a height of 10 mm are prepared with their axis in either one of

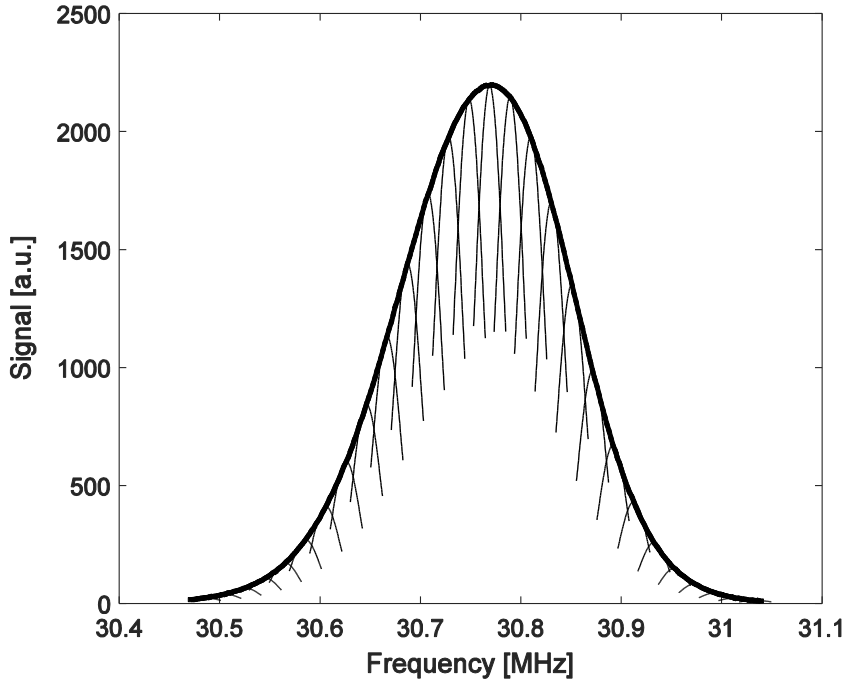

Figure 3.4: *An example of a typical reference profile acquired with a $CuSO_4$ solution in water. The frequency of the peak of the profile corresponds to the center of the coil. The thin curves represent the Fourier transforms of the spin-echo signals at different frequencies. The bold curve is the envelope of the peaks of the individual Fourier transforms. Away from the center frequency, the sensitivity of the coil decreases due to its finite length.*

the principal directions of wood (longitudinal, radial, tangential). The sample is then sealed on its side surface and bottom by a layer of Krytox© Teflon grease and several layers of Teflon tape, ensuring one-dimensional transport from one exposed surface. The sealed sample is placed inside a Teflon sample holder, where air can be blown over the top surface using a humidifier, which was introduced in Section 2.2. Moisture content profiles are determined by performing Hahn spin-echoes (Hahn, 1950) at different frequencies, i.e. at different positions, without moving the sample. These signals are Fourier transformed to acquire the signal intensity. To account for the decreasing sensitivity of the coil away from its center frequency, obtained values are divided by a reference profile, which is shown in Figure 3.4. This profile is acquired by capturing the Fourier transforms of the spin-echo signal at different frequencies using a reference sample containing a 0.1 M $CuSO_4$ solution in water. The tops of the Fourier transformed signals constitute the reference profile, highlighted by the bold line in Figure 3.4. To relate the captured signal to moisture content, a calibration procedure is first performed, which is described in Appendix B. After the measurement of a moisture content profile, a CPMG sequence (Meiboom & Gill, 1958) is performed at two different frequencies, i.e. at two different positions in the sample. The T_2 relaxation time distribution can then be obtained from the magnetization decay by Fast Laplace Inversion (Hürlimann & Venkataramanan, 2002).

The set-up for the simultaneous measurement of moisture content and expansion of a cylindrical sample, using a combination of NMR and a Philtec© optical fiber displacement

sensor, is shown in Figure 3.3c. A cylindrical sample with a diameter of 10 mm and a height of 30 mm is placed on the bottom of the cylindrical Teflon sample holder with an inner diameter of 22 mm. In contrast to the cylindrical sample for one-dimensional moisture transport measurement, the sides of the cylinder are not sealed. Instead, a small gold-coated Teflon plate is placed on its top surface. The optical fiber displacement sensor measures the distance to this surface, and therefore captures the length change of the sample during a dynamic measurement. Meanwhile, air from a humidifier is blown along the sides of the sample. Moisture content profiles are determined as described before. In this experiment, however, the spatial distribution has less importance since moisture enters the sample from the sides. The signal is therefore integrated over the sample height to arrive at the moisture content of the sample in total, rather than spatially.

3.3 RESULTS AND DISCUSSION

3.3.1 MOISTURE CONTENT AND EXPANSION

An example of the evolution of moisture content and one-dimensional expansion of two different, equally sized samples with sides of 6 mm during exposure to sinusoidal fluctuations in relative humidity is shown in Figure 3.5. Both moisture content and expansion fluctuate sinusoidally following the imposed relative humidity changes of the ambient air. Furthermore, the amplitude of the response, both in moisture content and expansion, is seen to decrease with increasing frequency. The moisture content and expansion over time can be fitted with a sine function to acquire the amplitude of the response. This is done for different frequencies (periods of 132 hours to 30 seconds) of the relative humidity variation 50 ± 40 %, to obtain the amplitude in moisture content and expansion as a function of frequency. This results in the Bode amplitude plots for moisture content and expansion, shown in Figure 3.6 for different sample sizes. In both plots three regions can be distinguished: a region at low frequencies where the amplitude is almost constant; an intermediate region with an inflection in the amplitude towards lower values; and a region at high frequencies with a constant decline in amplitude. Furthermore, a trend is observed with different sample sizes. The larger samples are seen to have their inflection already at a lower frequency compared to smaller samples. Moreover, at the same frequency in the high frequency region, the higher samples have a lower amplitude in both moisture content and expansion. Nevertheless, the slope in this region is seen to be almost equal for all sample sizes, between -0.75 and -0.88. Note that this is close to the theoretical value of -1, and thus a first indication that the system behaves as predicted.

One large deviation is seen in the moisture content Bode amplitude plot. Contrary to the other samples, the 2 mm sample is not seen to reach some more or less constant decline in the high frequency regime. A probable cause for the discrepancy is the presence of more permeable regions in this small sample, which contribute relatively more in a small sample. Although the density of the two small samples is not seen to deviate significantly from the other samples (all between 620-675 kg/m^3), visual inspection revealed two large vessels along the longitudinal direction of the sample for the measurement of moisture content. A similarly obvious presence of large vessels was not observed in the sample used in the measurement of

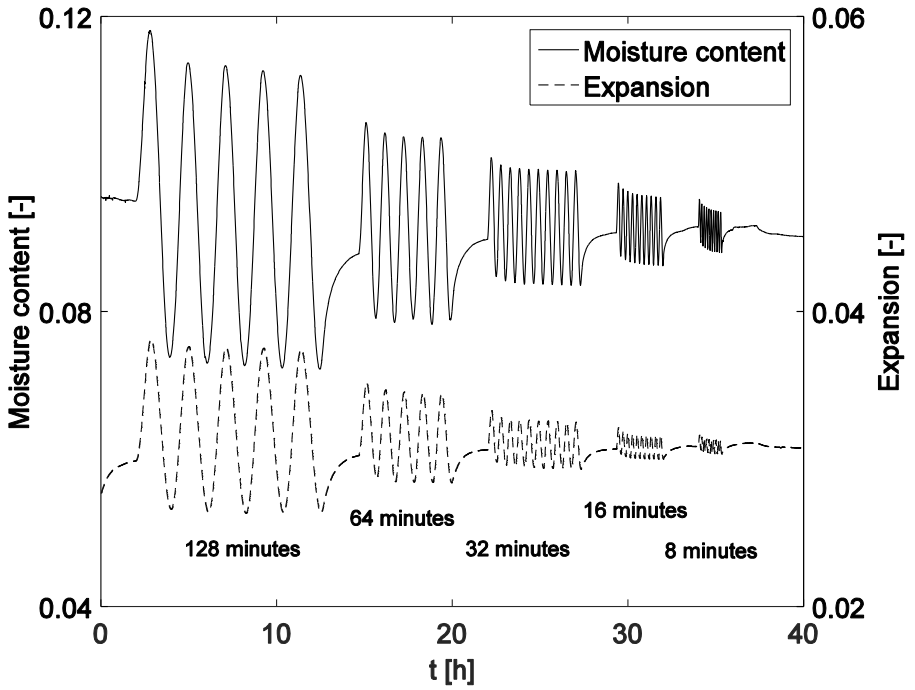

Figure 3.5: *An example of the evolution over time of the moisture content and expansion of two equally sized cubic blocks during exposure to sinusoidal variations in relative humidity (50 ± 40 %) at different frequencies, with equilibration time between two consequent frequencies. The periods of the fluctuations are indicated in the figure.*

the expansion. This may have contributed to the relatively high amplitude in moisture content compared to expansion observed at high frequencies, since moisture transport is generally faster in the longitudinal direction (Siau, 1984).

The frequency-dependence of the amplitude in the Bode plots in Figure 3.6 can be fitted with Eq. (3.2) to determine the time constant τ, as the reciprocal of b. This is done for both the moisture content and expansion amplitudes. For the fitting of the moisture content amplitude of the 2 mm sample, which is seen to deviate qualitatively from the other sample, the amplitudes of the highest four frequencies are omitted. The resulting characteristic times τ_{mc} and τ_{exp}, for the moisture content and expansion respectively, are related in Figure 3.7. The linear curve indicates equal values for τ_{mc} and τ_{exp}. Values are either on or slightly left of this curve, indicating the agreement in characteristic times for moisture content and expansion. Again a deviation in the 2 mm sample is observed, which results from its deviation in moisture content amplitude. Values for the diffusion coefficient, calculated using Eq. (3.1) and shown in Figure 3.7, are approximately constant in all samples, i.e. no clear trend with sample size is observed. The values of $\sim 1 \cdot 10^{-10}$ m^2/s are average values over all directions, although moisture transport in oak is anisotropic with different values in the three principal directions. Nevertheless, the values are in good agreement with the radial diffusion coefficients reported by Simpson (Simpson, 1993), derived from one-dimensional experiments.

Using the calculated diffusion coefficients from the frequency behavior, the Bode plots can be scaled by the dimensionless frequency f^*, as shown in Figure 3.8. The scaling

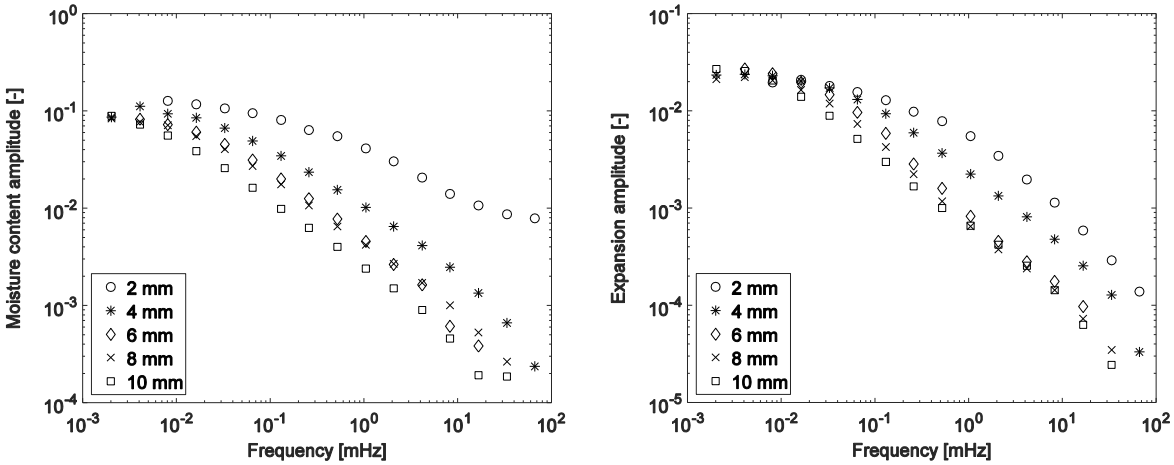

Figure 3.6: *Moisture content amplitude (left) and expansion amplitude (right) as a function of frequency. The lowest frequency corresponds to a fluctuation with a period of 134 hours, the highest to a period of 30 seconds.*

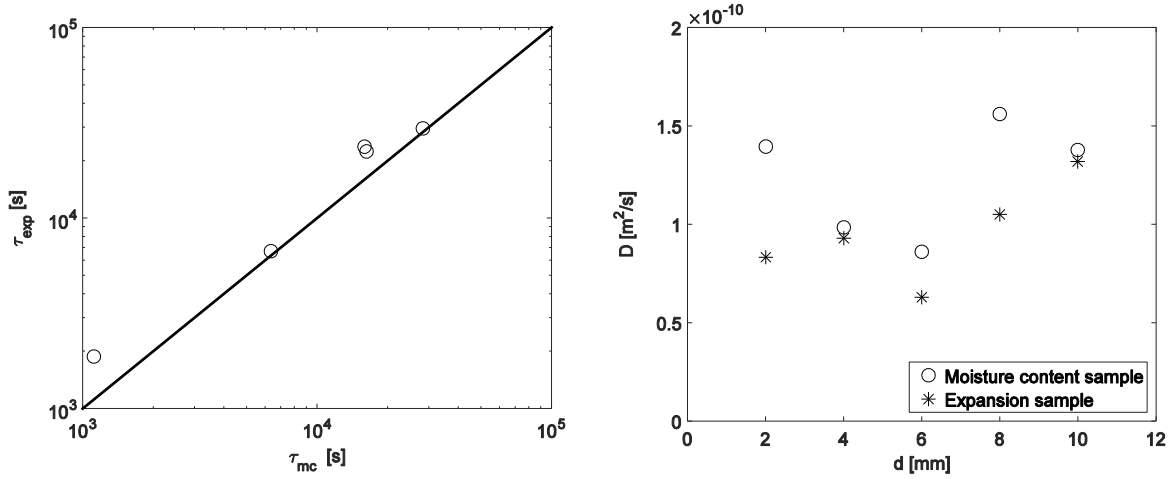

Figure 3.7: *The characteristic moisture sorption time as a function of the characteristic expansion time (left), and the diffusion coefficients as derived from the characteristic times for different sample sizes (right).*

derived from the simple theory results in one single curve for all experimental points of the different samples, both for moisture content and expansion. An exception is the moisture content amplitude of the 2 mm sample, which was already seen to deviate in its qualitative behavior in the original Bode plot. The inflection points which were distinguishable in the original Bode amplitude plots are now approximately on the same scaled frequency. The moisture content and expansion amplitudes plotted in the same graph as a function of f^* are found to approximately overlay when a hygroscopic expansion coefficient of 0.3 is used (Saft & Kaliske, 2013), as shown in Figure 3.9. Furthermore, the experimental results largely follow the qualitative behavior as expected from theory, illustrated by the theoretical curve of

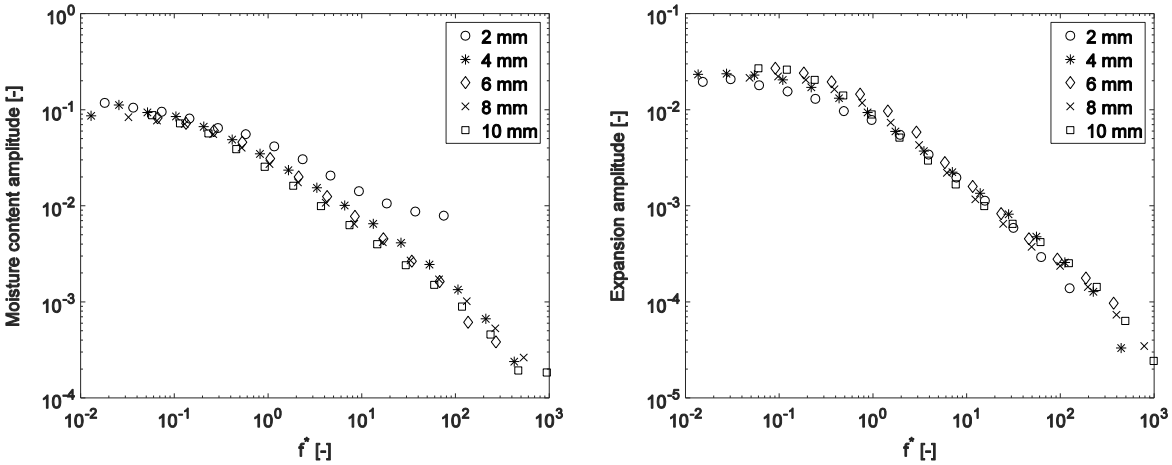

Figure 3.8: *Moisture content amplitude (left) and expansion amplitude (right) as a function of the dimensionless frequency.*

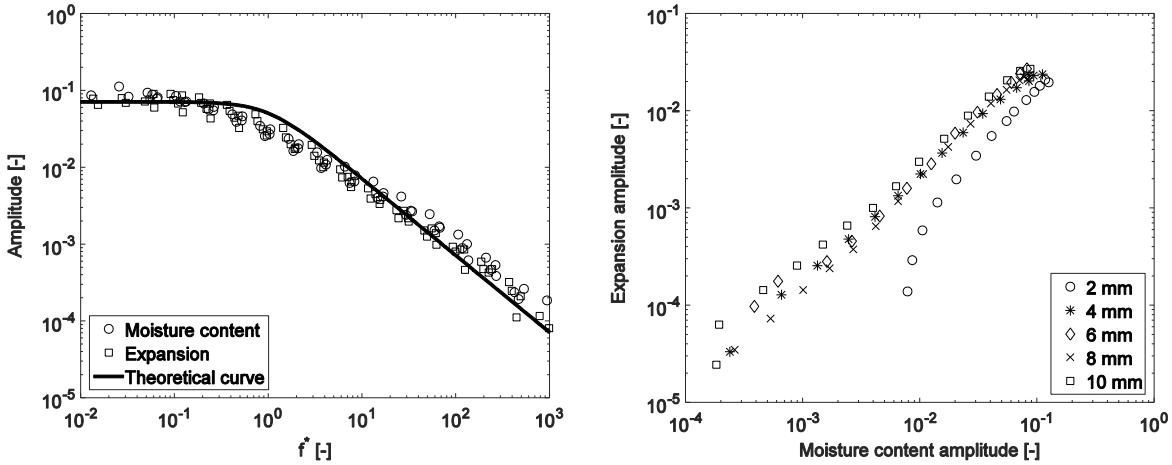

Figure 3.9: *Amplitude as a function of dimensionless frequency for moisture content and expansion with the theoretical prediction (left), where an expansion coefficient of 0.3 is assumed, and the relation between moisture content and expansion amplitude (right). In the left figure, the moisture content amplitude of the deviating 2 mm sample is omitted.*

Eq. (3.7). Again three regions can be distinguished, depending on the relation between the frequency of the changes and the capability of the sample to equilibrate. The one-on-one relation between moisture content and expansion is even more obvious when the expansion amplitude is plotted as a function of the moisture content amplitude, also shown in Figure 3.9. From both plots, the linear relation between moisture content and expansion amplitude is evident. The slope on the logarithmic scale has a value of approximately 1, indicating that a change in moisture content amplitude is associated with an equally large relative change in expansion amplitude, even at high frequencies.

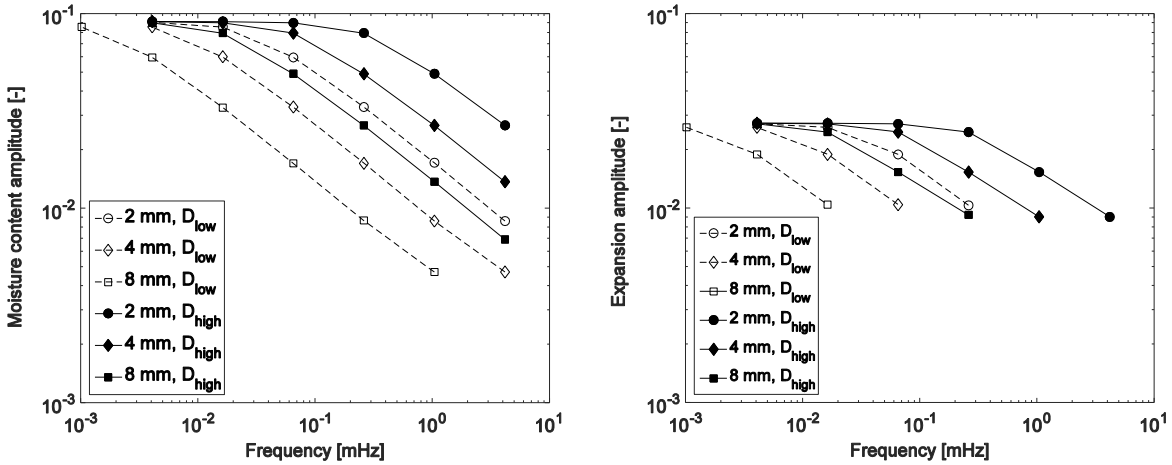

Figure 3.10: *Moisture content amplitude (left) and expansion amplitude (right) as a function of frequency, for different sample sizes in an isotropic model. Two different diffusion coefficients are used in the simulations (D_{low} = $5 \cdot 10^{-11}$ m^2/s, D_{high} = $5 \cdot 10^{-10}$ m^2/s). Other values used are $\alpha = 0.3$, $E = 3 \cdot 10^9$ Pa, Poisson's ratio $\upsilon = 0.3$, $\rho = 650$ kg/m^3.*

The linear relation in the amplitudes over a wide range of frequencies and the linear relation between the characteristic times τ indicates the immediate expansive response of the samples to the induced moisture content changes. Furthermore, analysis of the phase lag yielded no significant differences between moisture content and expansion. The effect of viscoelasticity, sometimes attributed to wood (Schniewind & Barrett, 1972), is therefore not substantial in these experiments. A significant contribution of viscoelasticity would results in a different frequency behavior for moisture content and expansion, with a more rapid decline in the expansion amplitude at higher frequencies. The similar shape of the experimental Bode amplitude plots contradicts this.

3.3.2 NUMERICAL SIMULATIONS

Bode amplitude plots for moisture content and expansion of the isotropic model with two different diffusion coefficients are shown in Figure 3.10. In accordance with the experiments, the simulations are performed with a relative humidity fluctuation of 50 ± 40 %. The few points in the expansion amplitude plot are due to the requirement of a too fine mesh to accurately describe the expansion. The moisture content can be simulated with a coarser mesh. Nevertheless, the same qualitative shape as predicted from theory is observed, with constant amplitude at relatively low frequencies and a constant negative slope at high frequencies. In accordance with the theory, a lower diffusion coefficient results in the inflection of amplitude at lower frequencies. Furthermore, the amplitude in both moisture content and expansion is lower at high frequencies for a lower diffusion coefficient.

The expansion amplitude in the isotropic model is uninfluenced by the magnitude of the Young's modulus E: increasing E by an order of magnitude results in equal expansion amplitudes at all frequencies. Moreover, the anisotropic model with average transport and mechanical properties from Saft and Kaliske (2013) differs only slightly from the results from the isotropic model with high diffusion coefficient, as shown in Figure 3.11. Assuming their

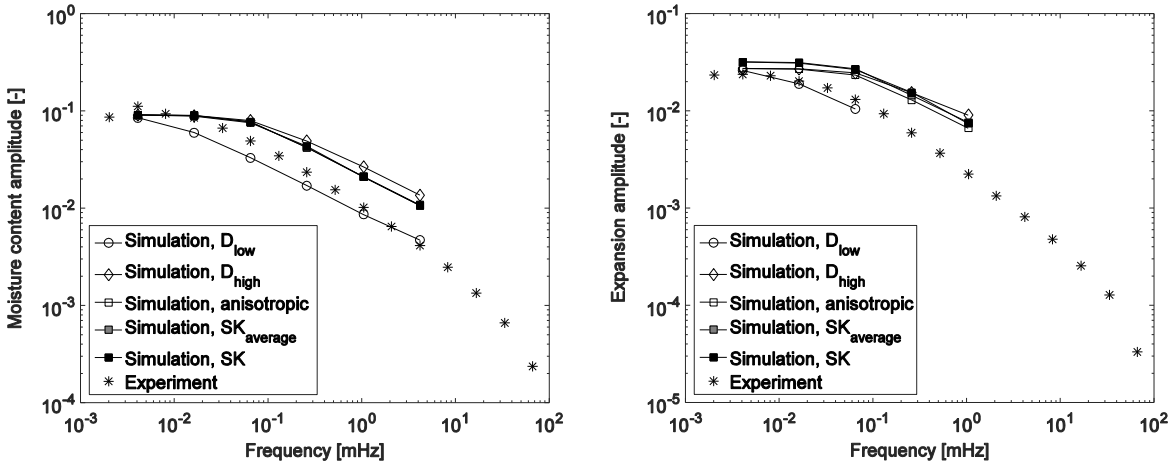

Figure 3.11: *Amplitude as a function of frequency for moisture content (left) and expansion (right), for a sample size of 4 mm. Different models are used in the simulations: an isotropic model with different diffusion coefficients (D_{low} = $5 \cdot 10^{-11}$ m^2/s, D_{high} = $5 \cdot 10^{-10}$ m^2/s), an anisotropic moisture transport model ($D_{longitudinal}$ = $1 \cdot 10^{-9}$ m^2/s, D_{radial} = $D_{tangential}$ = $5 \cdot 10^{-11}$ m^2/s) with constant, isotropic mechanical properties (α = 0.3, E = $3 \cdot 10^9$ Pa, υ = 0.3), and the anisotropic model with moisture dependent transport and mechanical properties proposed by Saft and Kaliske (SK), where average properties over the moisture content of interest are used, and moisture-dependent properties.*

proposed moisture content dependence of the Young's and shear moduli, and of the three moisture diffusion coefficients yields similar results as simulations with averages of these properties over the moisture content range of interest. All simulation results are, however, seen to overestimate experimental results, when compared in Figure 3.11 for a sample size of 4 mm. The moisture content amplitude is overrated by the high diffusion coefficient (D_{high} = $5 \cdot 10^{-10}$ m^2/s) and the anisotropic moisture transport model, with dominant transport in the longitudinal direction ($D_{longitudinal}$ = $1 \cdot 10^{-9}$ m^2/s, D_{radial} = $D_{tangential}$ = $5 \cdot 10^{-11}$ m^2/s). The isotropic model with low diffusion coefficient (D_{low} = $5 \cdot 10^{-11}$ m^2/s) predicts the frequency dependence of the amplitude best, although the inflection point is seen to be lower. Note that the derived diffusion coefficient in Figure 3.7 corresponds quite well to this diffusion coefficient. In the expansion amplitude plot, the same is seen. The slope of all simulated results is, however, lower than the experimental slopes.

The relation between the amplitudes in moisture content and expansion is shown in Figure 3.12 for different simulations and experiments. As already shown in Figure 3.9, the experiments manifest a linear relation on the logarithmic scale. The simulations demonstrate a similar linear relation, however, due to the mesh requirement only a limited range in moisture content and expansion amplitudes is simulated. The one-on-one relation between moisture content and expansion, for all simulation models, justifies the use of Eq. (3.9) in the derivation of the scaling parameter f^*.

The Bode amplitude plots resulting from numerical simulations can be scaled by the dimensionless frequency in Eq. (3.6), as was done with experimental results previously. The scaled simulated Bode amplitude plots are shown in Figure 3.13 for the isotropic model, for anisotropic moisture transport but isotropic mechanical properties, and for the anisotropic

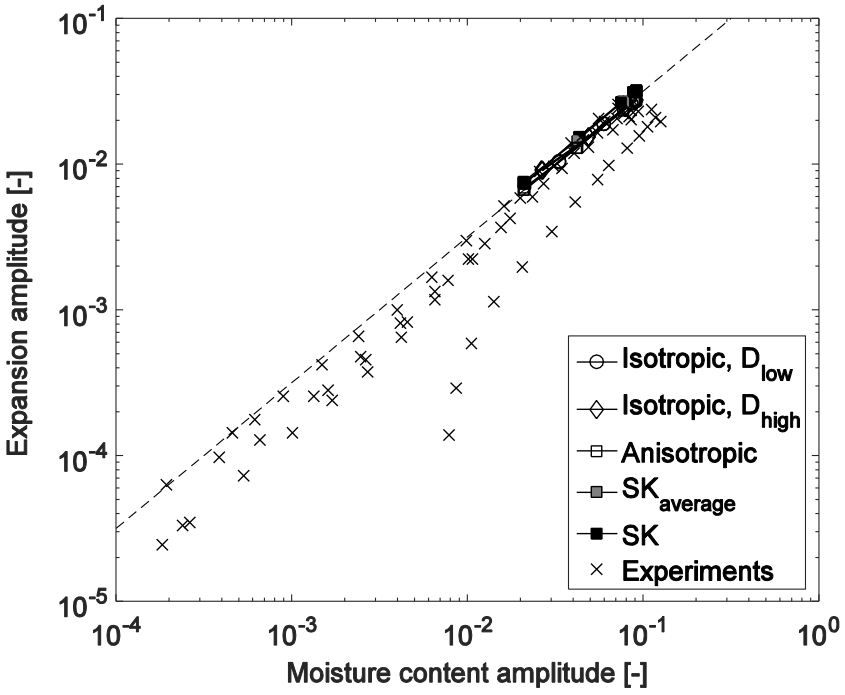

Figure 3.12: *The moisture content amplitude as a function of the expansion amplitude for experiments and simulations.*

model with moisture-dependent transport and mechanical properties as proposed by Saft and Kaliske (2013). For the models with anisotropic moisture transport, an average of the three diffusion coefficients is used for D in the calculation of f^*. The scaled moisture content Bode amplitude plots are found to be on one single curve, similar to the experiments. Even results of the anisotropic, moisture dependent model are seen to produce a scalable Bode amplitude plot, despite the rough estimate for an apparent diffusion coefficient in terms of an average of the three individual coefficients.

The expansion shows a similar single curve for all scaled amplitudes, although some minor deviations are observed. Nevertheless, all models, including the anisotropic model with moisture dependent mechanical properties, roughly show the same behavior after scaling. The simulated and experimental results, although both scalable, deviate especially at high values of f^*. A possible cause is the assumption in the models that moisture transport can be described by the diffusion equation, with a single diffusion coefficient for both water vapor transport in the lumens and moisture transport in the cell wall. This has been contradicted in literature (Wadsö, 1994), and several studies treat the two transport mechanisms separately, coupled by a sorption rate term (Dvinskikh, et al., 2011; Eitelberger, et al., 2011). This might result in a lower moisture content amplitude at high frequencies, where the sorption rate starts to play a role. Water vapor, with a higher diffusion coefficient, may penetrate in the material, but the fast fluctuations do not result in significant exchange with moisture in the cell wall. Not only the moisture content amplitude is affected by this, but also the expansion, which is caused by the moisture in the cell walls. Future multi-Fickian simulations can affirm or reject this hypothesis.

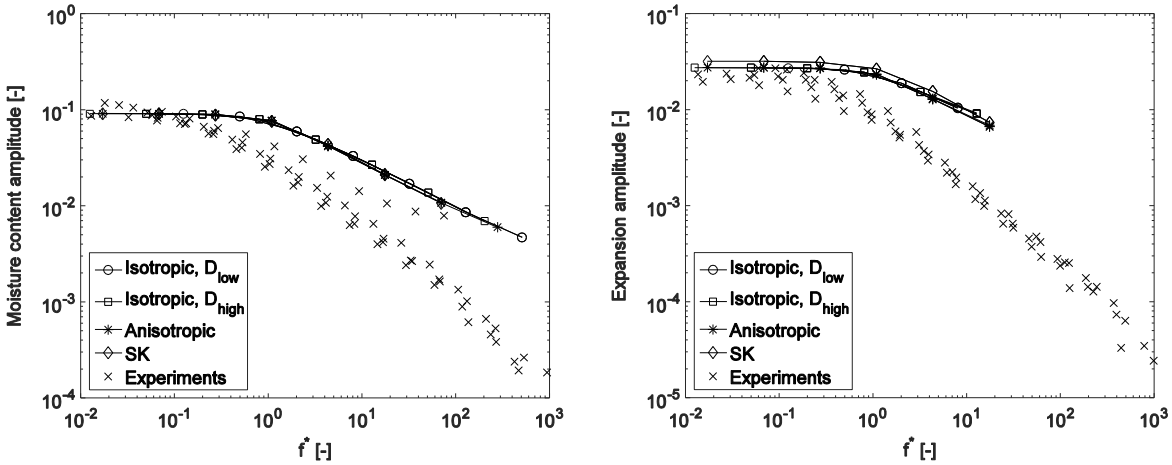

Figure 3.13: *Moisture content amplitude (left) and expansion amplitude (right) as a function of the scaled frequency f^*, for isotropic models ($D_{low} = 5 \cdot 10^{-11}$ m^2/s, $D_{high} = 5 \cdot 10^{-10}$ m^2/s), an anisotropic moisture transport model ($D_{longitudinal} = 1 \cdot 10^{-9}$ m^2/s, $D_{radial} = D_{tangential} = 5 \cdot 10^{-11}$ m^2/s) with constant, isotropic mechanical properties ($\alpha = 0.3$, $E = 3 \cdot 10^9$ Pa, $\upsilon = 0.3$), and the anisotropic model with moisture dependent transport and mechanical properties proposed by Saft and Kaliske (SK).*

3.3.3 NMR

Experiments are performed on cylindrical samples with their axes in longitudinal, radial, or tangential direction. Moisture content profiles of a sample with its axis along the longitudinal direction during exposure to a sinusoidal fluctuation in relative humidity are shown for one sinusoidal cycle in Figure 3.14. The outer 1 mm of the sample near both surfaces is omitted since the resolution (~1 mm) does not allow a sharp boundary to be detected. Nevertheless, the moisture content near the exposed surface is seen to fluctuate with the largest amplitude, and moisture content gradients are observed. The moisture content fluctuation at different depths from the exposed surface is plotted in Figure 3.14 as well, which shows a monotonically decreasing amplitude away from the surface. Near the sealed surface of the sample, however, the moisture content is still seen to fluctuate to a large extent, with an amplitude of approximately one half of the amplitude near the surface.

In contrast to the homogeneous structure of the longitudinal sample, the radial and tangential sample exhibit inhomogeneities, as shown in Figure 3.15. These inhomogeneities are manifested in a non-constant moisture content profile at equilibrium, with regions of lower and higher density. A region with higher density, i.e. more cell wall material compared to cell cavities, is capable to accommodate more moisture, and thus provides more signal, which is perceived as a higher moisture content. Similarly fluctuating profiles in the radial direction have been found by (Hameury & Sterley, 2006), attributed to the consequent regions of earlywood and latewood.

The amplitude in moisture content in three samples with different principal transport directions (longitudinal, radial, tangential) for three different frequencies (periods of 17, 8.5, and 4.25 hours) is shown as a function of the distance from the exposed surface in Figure 3.16. The longitudinal sample has a clear decay in amplitude, which was already observed in

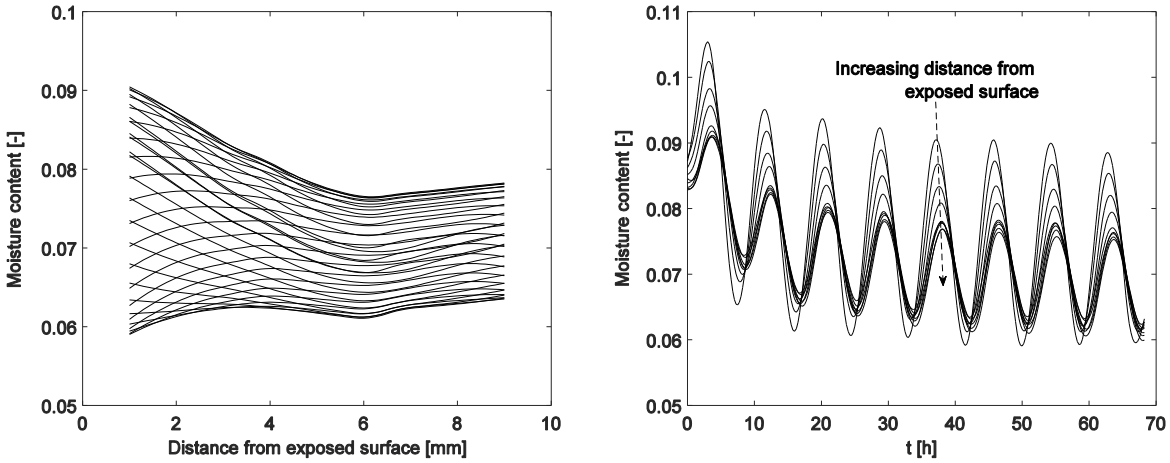

Figure 3.14: *Moisture content profiles during one cycle (left) and the moisture content at different depths from the exposed surface (right) of a longitudinal sample during exposure to a sinusoidal fluctuation in relative humidity (50 ± 40 %), with a period of 8.5 hours. The time between subsequent moisture content profiles is 15 minutes.*

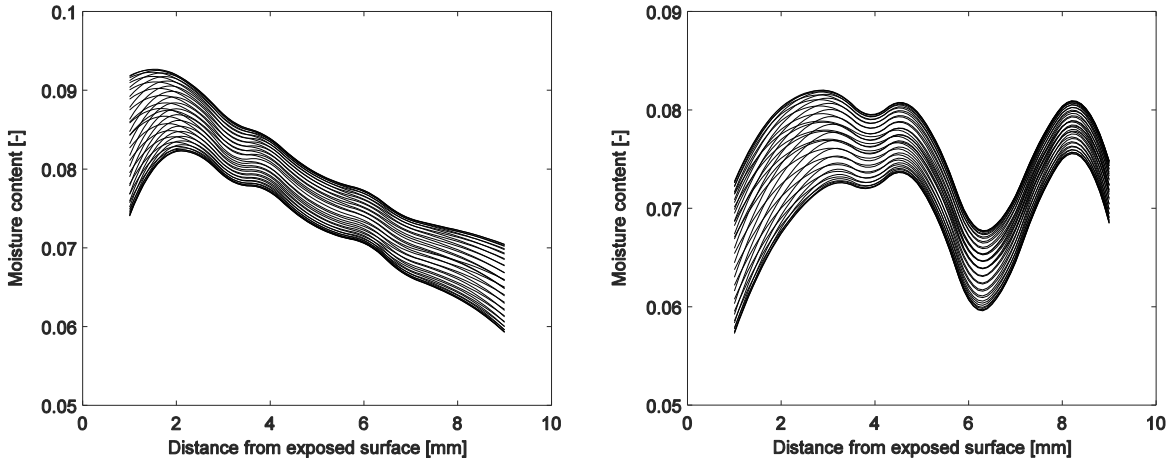

Figure 3.15: *Moisture content profiles during one cycle for transport in the radial direction (left), and in the tangential direction (right), during exposure to a sinusoidal fluctuation in relative humidity (50 ± 40 %), with a period of 8.5 hours. The time between subsequent moisture content profiles is 15 minutes.*

Figure 3.14. The amplitude is the highest near the exposed surface, and monotonically decreases towards the sealed surface. Furthermore, the amplitude is seen to be lower for increasing frequency, which is consistent with the results obtained from moisture sorption and expansion experiments described in the previous section. A similar clear decrease in amplitude is not observed for samples with transport in radial and tangential direction. Although the amplitude is the highest near the exposed surface, the decrease in amplitude is minimal, and even quite high at the sealed surface. An experiment is conducted with the radial sample upside down, i.e. with the sealed surface exposed to the air flow, where moisture penetration through the layers of Teflon tape and Krytox© grease is observed. Additional experiments were therefore performed with a thicker layer of Krytox© grease on the radial

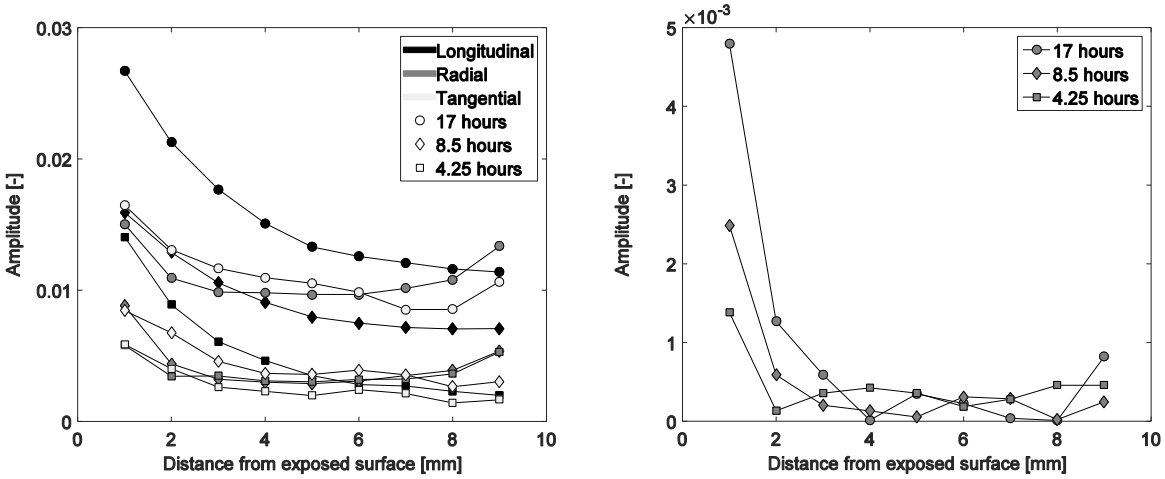

Figure 3.16: *Moisture content amplitude as a function of the distance from the surface for different transport directions and different frequencies. Original experiments (left), and a repeated experiment on a radial sample after removal of Teflon tape and application of a thick layer of Krytox© Teflon grease (right).*

sample, without Teflon tape surrounding it. The results in Figure 3.16 show a more rapid decay of the amplitude away from the exposed surface, with a minor penetration depth of the moisture into the sample. The additional experiments also illustrate that moisture has penetrated through the sides in the original experiments, since the large amplitude in the middle of the sample in the original experiment has vanished. The presented measurements therefore need to be repeated with a thicker layer of Krytox© grease to ensure one-dimensional transport.

Despite the absence of purely one-dimensional transport, Figure 3.16 shows a dominance of transport in the longitudinal direction over the other two directions. The amplitude in the longitudinal sample is higher in the original experiments compared to the other two directions. Moreover, the application of a thicker layer of Krytox© grease on the sides of the radial sample obstructs transport in the longitudinal direction. The consequent disappearance of the high amplitudes away from the surface demonstrates the major contribution of the longitudinal direction on the moisture transport. It can therefore be concluded that transport in the longitudinal direction is dominant.

During the sinusoidal fluctuation in relative humidity, a CPMG sequence is performed at two different frequencies, i.e. at two different positions in the sample, one near the middle and one near the exposed surface. Fast Laplace Inversion is applied on each CPMG sequence to acquire the T_2 relaxation time distributions of water inside the sample. An example of the distributions during one cycle in relative humidity for the position closest to the exposed surface is shown in Figure 3.17. The T_2 distribution is seen to shift over time, and the signal intensity changes. The contour plot in Figure 3.17 illustrates the sinusoidal shift of the T_2 distributions over time more clearly, towards lower values at low moisture content and higher values at high moisture content.

If the model of Brownstein and Tarr (1979) is applied, the shifting of the T_2 distribution can be coupled to the moisture being present in different pore sizes during the experiment. In wood, moisture can roughly be present in cell cavities, either as liquid water or

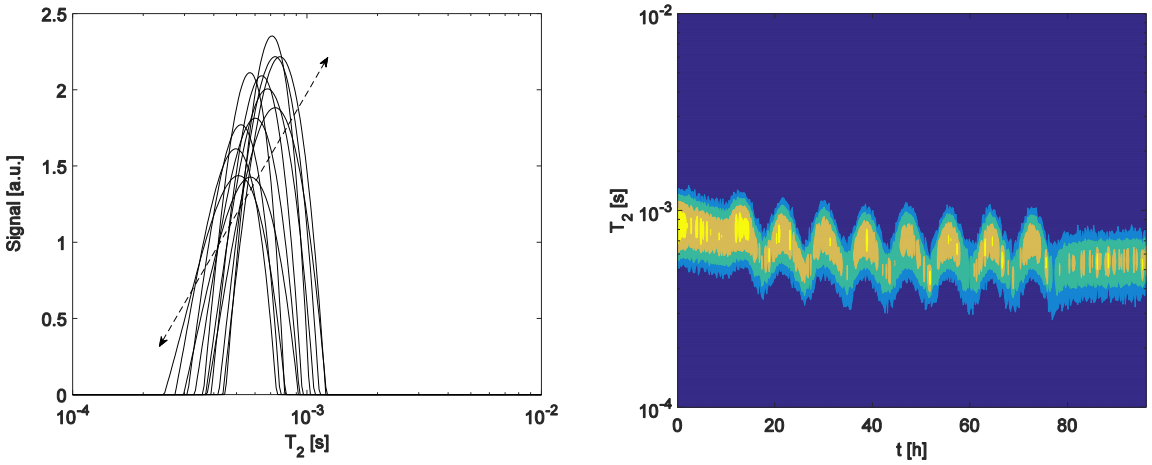

Figure 3.17: *Example of the T_2 distribution shift over time during one cycle (left), and a contour plot showing the evolution of the T_2 distribution near the surface of the sample (right), during exposure to a sinusoidal fluctuation in relative humidity (50 ± 40 %) with a period of 8.5 hours.*

as water vapor, and between microfibrils in the cell walls. Below the fiber saturation point, which holds for this experiment, no liquid water in the cell cavities is present, only water vapor and cell wall water. Whereas moisture in a cell cavity can be considered as moisture inside a pore, moisture in the cell wall should be approached slightly different (Balcom, 2016). At low moisture content, moisture in the cell wall is adsorbed on the surface of the cell wall constituents, mainly on the surface of hemi-cellulose. At higher moisture content, multiple layers will form on the surface, and also moisture between two opposing layers will be present. This moisture is less confined compared to moisture adsorbed on the surface, and its magnetization will therefore relax slower. With increasing moisture content, the ratio between the less confined moisture and adsorbed moisture increases, i.e. the surface-to-volume ratio decreases. As a consequence, the T_2 relaxation time of the moisture in the cell wall rises. Although the notion of the space between microfibrils as a pore is source for discussion, the behavior in magnetization relaxation can be equivalent to the model of Brownstein and Tarr. An indication for the above hypothesis is the shifting of the bounds of the T_2 distributions over time during sinusoidal relative humidity fluctuations, as shown in Figure 3.17. Generally, moisture in a porous medium is present in the smallest pores at low moisture content, and fills increasingly larger pores with increasing moisture content. During sinusoidal fluctuations in moisture content, this would imply that the lower bound of the T_2 distribution remains constant and the upper bound fluctuates sinusoidally over time. In the experiments, sinusoidal shifting of both bounds of the distribution is observed. This could suggest drainage of small pores during wetting, which contradicts general findings in porous media and is counterintuitive. More insight can be gained by additional experiments with a sinusoidal relative humidity fluctuation on materials which do not exhibit hygro-expansion (e.g., brick or concrete).

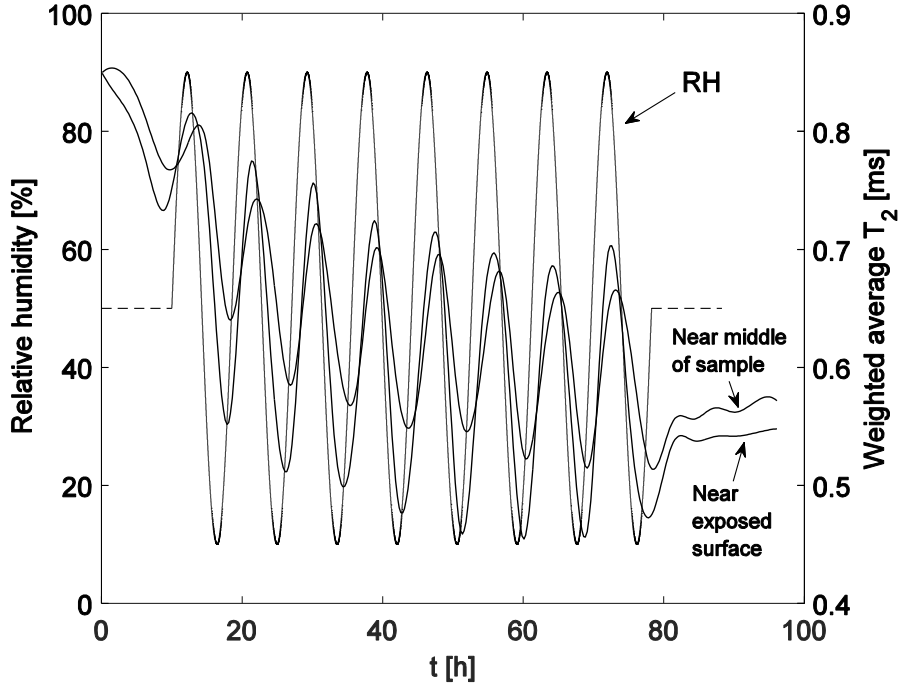

Figure 3.18: *Weighted T_2 average over time at two different distances from the exposed surface during exposure to a sinusoidal fluctuation in relative humidity (RH) of 50 ± 40 %, with a period of 8.5 hours.*

Kleinberg (1996) already concluded that, although relaxation time distributions can be significantly affected by measurement noise, integrated measures of the distributions are stable. A weighted average of each T_2 distribution is therefore calculated to arrive at a representative T_2 value over time. Its cubic spline interpolation is shown in Figure 3.18 for the two different positions. As can be expected from the contour plot in Figure 3.17, the weighted T_2 average fluctuates sinusoidally. Furthermore, the amplitude in the fluctuation is higher near the surface of the sample compared to the middle of the sample. This corresponds to the higher amplitude in moisture content near the surface, as observed in Figure 3.16. A higher amplitude in moisture content is thus accompanied by a higher amplitude in average T_2.

Several experiments are performed with long cylindrical samples, with their axes along the radial and tangential direction, to couple moisture content and T_2 to expansion under sinusoidal exposure conditions. The contour plot of the T_2 distribution over time of one of these experiments is shown in Figure 3.19. More noise is observed compared to Figure 3.17, especially at low moisture content. This is caused by the smaller cross-sectional area of the cylinder in the expansion measurements, leading to less signal and therefore a lower signal-to-noise ratio. Nevertheless, the contour plot clearly shows the sinusoidal course of the T_2 distribution over time, consistent with our previous results. Again a weighted average of each T_2 distribution is calculated to arrive at a representative value over time. The evolution of the T_2 average, moisture content, and expansion is shown in Figure 3.19. All three quantities fluctuate sinusoidally to the imposed cyclic exposure condition. An increase in moisture content is seen to be associated with an increase in both expansion and T_2. Vice versa, a lower moisture content is accompanied by a decrease in expansion and T_2. If we recall the

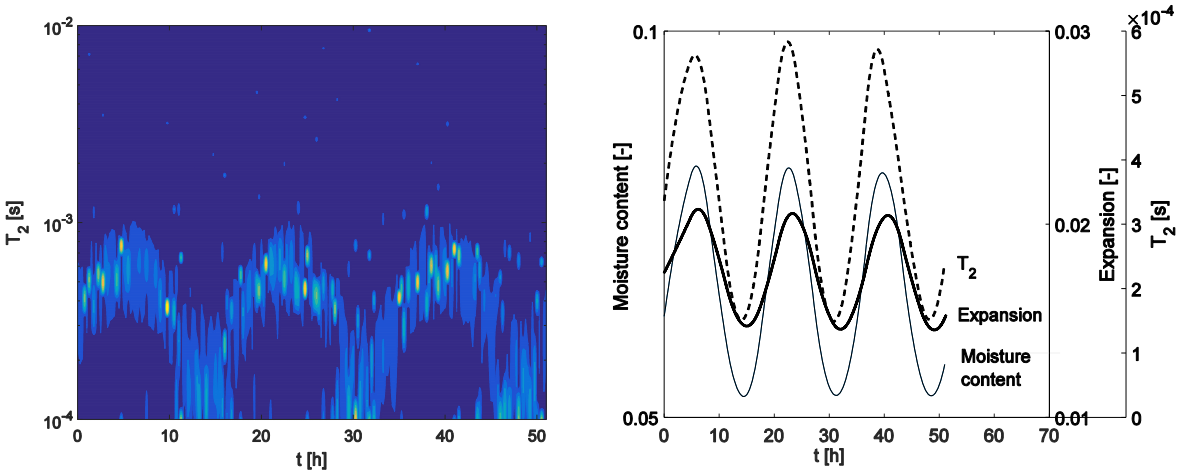

Figure 3.19: *Contour plot of the T_2 distribution over time (left) during exposure to a sinusoidal fluctuation in relative humidity (50 ± 40 %), with a period of 17 hours, and moisture content, expansion, and weighted T_2 average over time during the same experiment (right).*

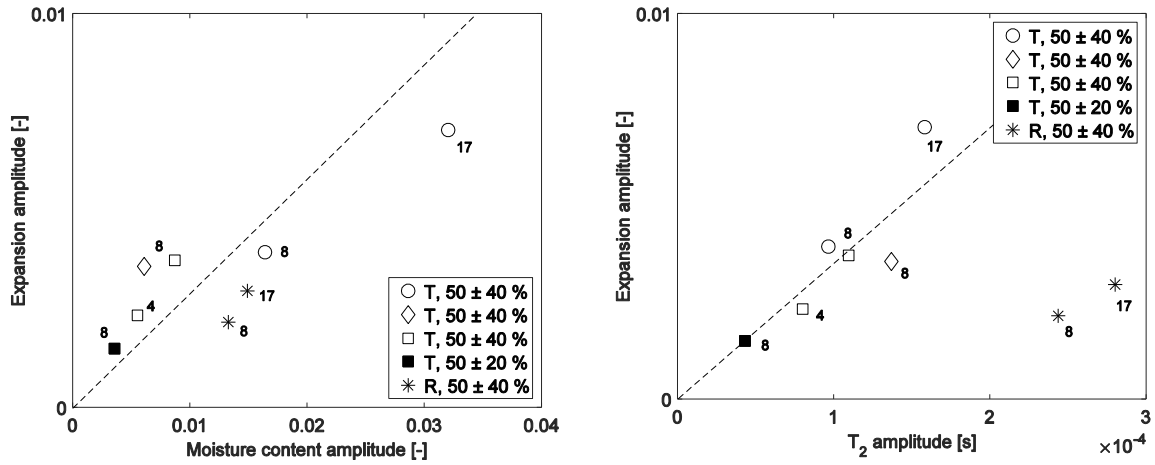

Figure 3.20: *The expansion amplitude as a function of the moisture content amplitude (left) and the T_2 amplitude (right) for tangential (T) and radial (R) expansion, with different fluctuations in relative humidity. Four different samples are used, which are shown by the different markers. The periods of the fluctuations (4.25, 8.5, and 17 hours) are added to the figures as 4, 8, and 17.*

discussion above concerning the increase in space between microfibrils in the cell wall associated with an increase in moisture content, these results arise naturally. An increase in moisture content results in more moisture in the cell wall, i.e. between the microfibrils, which was already seen to increase the T_2. The moisture forces the two opposing fibrils apart, which is perceived as macroscopic expansion. The same mechanism is hence responsible for both a change in T_2 of the moisture in the cell wall and the macroscopic expansion.

Three different frequencies of relative humidity fluctuations are imposed on the samples. The results in Figure 3.20 show the relation between amplitudes in moisture content and expansion, and T_2 and expansion. An increase in the moisture content amplitude is

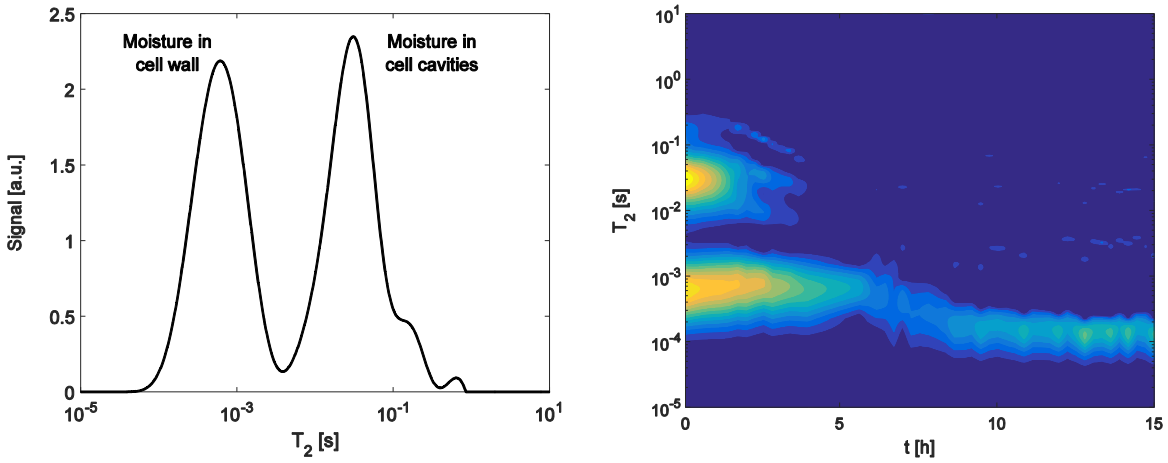

Figure 3.21: *Initial T_2 distribution of a vacuum-saturated sample (left) with two distinct peaks attributed to moisture in the cell wall and moisture in the cell cavities, and the evolution of the T_2 distribution over time (right) during exposure to a dry air flow.*

associated with a larger expansion amplitude, as already observed in the previous sections. Furthermore, slower fluctuations are associated with a larger amplitude in both moisture content and expansion. The sample with its axis along the radial direction exhibits less expansion at equal moisture content amplitude, which is in accordance with literature (Skaar, 1988). A smaller amplitude in relative humidity additionally results in a smaller amplitude in moisture content, expansion, and T_2. Moreover, a linear relation between the amplitudes in moisture content and expansion, and T_2 and expansion is observed for the tangential samples, pointing to the origin. A similar relation is not seen in the radial sample. Since it concerns the measurement of only one sample, however, no conclusions can be drawn regarding this result.

An additional experiment is performed to elucidate the expansive mechanisms in the sample. To this end, a sample with the tangential direction along its axis is vacuum-saturated with water before placement in the sample holder. Instead of exposure to a sinusoidally varying relative humidity, the sample is exposed to a dry air flow. Meanwhile, its length is measured and a CPMG sequence is performed to derive the relaxation characteristics of the moisture in the sample. The initial T_2 distribution of the completely saturated sample is shown in Figure 3.21. In contrast to the single peak in the previous experiments below the fiber saturation point, two peaks are observed. These peaks can be attributed to water in the cell cavities and water in the cell walls (Telkki, et al., 2013). The water in the cell cavities is more mobile since it is less confined, and therefore has a higher T_2 value. The moisture in the cell walls is more confined, resulting in a lower T_2, as discussed before. The course of the T_2 distribution over time is shown in the contour plot in Figure 3.21, with bright areas indicating a high signal intensity and thus a high moisture content. Initially, the two peaks are clearly visible. Progressing in time, the signal of the moisture in the cell cavities is seen to lose intensity, and after ~3 hours, the moisture in the cell cavities has disappeared. The signal intensity of the moisture in the cell wall decreases significantly only after the signal of the moisture in the cell cavities has disappeared. This illustrates the drainage of moisture from the large, pore-like cell cavities first during drying, while moisture in the cell walls is hardly affected.

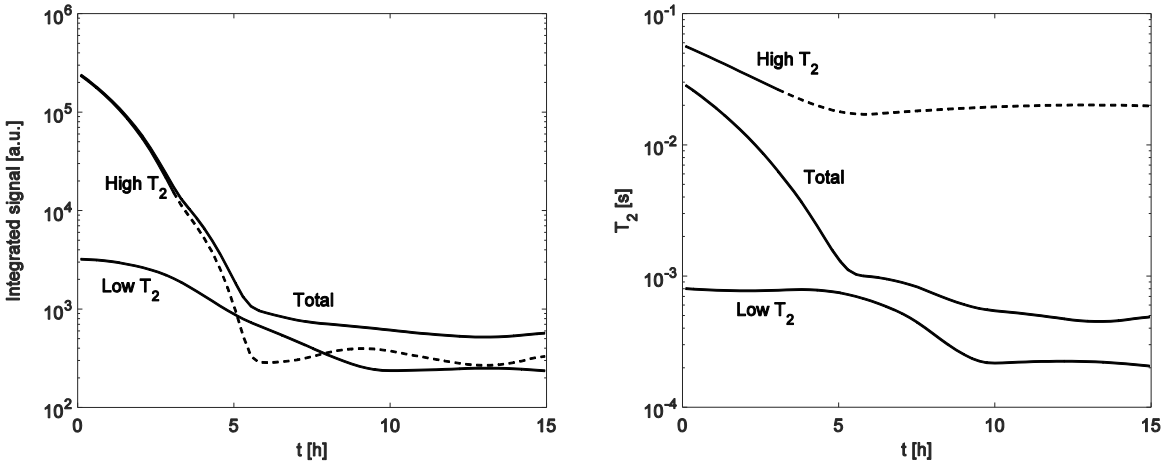

Figure 3.22: *Evolution over time of the integrated signal (left) and the weighted T_2 average (right) of the total population and of the populations with low and high T_2 values of a vacuum-saturated sample during exposure to a dry air flow. The dotted line indicates the part of the experiment where the average values of the high T_2 components is governed merely by noise.*

A weighted average is calculated for the total population of the sample, but also for the populations with high and low T_2 separately. These values as a function of time are shown in Figure 3.22. Initially, the integrated signal of the moisture in the cell cavities is two orders of magnitude higher than the cell wall component. A considerably larger volume of water is accordingly present in the cell cavities. The signal intensity, however, drops rapidly, and after some time, only moisture in the cell wall is present. As can be seen in the contour plot in Figure 3.21, the signal of the moisture in the cell cavities has disappeared. Due to measurement noise, however, the fitting procedure produces some incidental minor peaks in signal intensity afterwards. An average can therefore still be calculated, although it is not caused by the physical presence of moisture. This part is therefore indicated in the plots by a dotted line.

The T_2 value of the moisture in the cell cavities initially decreases while the value of the moisture in the cell wall remains constant. Unlike the cell wall, cell cavities can be considered as pores. The initial T_2 distribution illustrates that the moisture in the cell cavities is present in a distribution of pore sizes. Application of Brownstein and Tarr's theory on the decrease in T_2 indicates that large pores are emptied first, and the average pore size in which the moisture is present decreases while the material dries. This is consistent with previous NMR studies on wood drying (Menon, et al., 1987; Elder & Houtman, 2013).

The expansion of the sample during the experiment is initially constant, as shown in Figure 3.23. No shrinkage of the sample is observed although water is released from the cell cavities. Only after some time the sample starts to shrink notably. The contour plot in Figure 3.21 shows that the shrinkage is associated with a loss of the signal intensity of moisture in the cell wall. This is also observed when the expansion is plotted as a function of the integrated signal. An initial decrease in signal intensity of the moisture in the cell cavities is accompanied by a constant length, whereas a decrease in signal of the moisture in the cell wall is immediately associated with shrinkage. The expansion as a function of T_2 in Figure

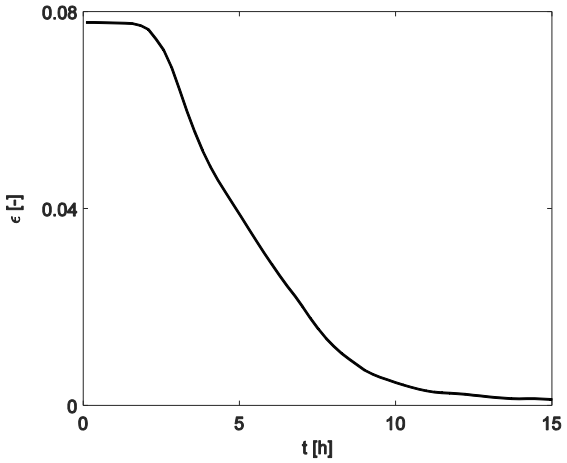

Figure 3.23: *The expansion ε over time of the initially vacuum-saturated sample relative to the final length during exposure to dry air.*

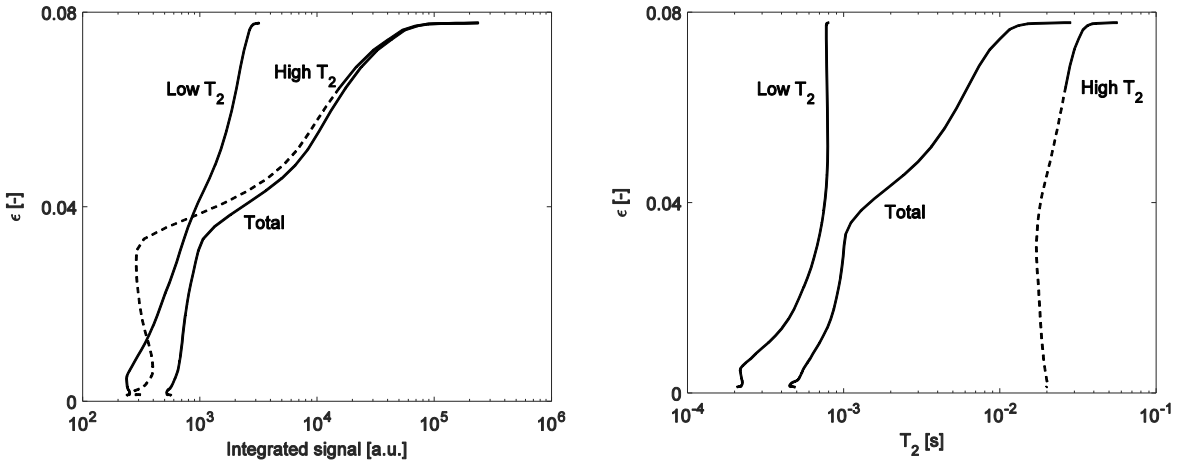

Figure 3.24: *Expansion as a function of the integrated signal (left), and as a function of the weighted T_2 average (right) of the total population and of the populations with low and high T_2 values of a vacuum-saturated sample during exposure to dry air. The dotted line indicates the part of the experiment where the average values of the high T_2 components is governed merely by noise.*

3.24 demonstrates that an initial decrease in T_2 of the moisture in the cell cavities is accompanied by a constant length. The average T_2 of the moisture in the cell wall, however remains constant initially, and starts to decrease only after half of the shrinkage has occurred. This is an unexpected result, since previous results with sinusoidal exposure conditions revealed that the T_2 changes as the moisture content changes. Here we see a constant average T_2 accompanied by a decline in the signal intensity. The moisture is thus released from the cell wall without changing the T_2. Contrary to the previous experiments, the sample was initially vacuum-saturated in this experiment. Furthermore, the sample had been oven-dried before. These actions might have had an influence on the microstructure of the wood.

3.4 CONCLUSIONS

Despite many factors influencing three-dimensional moisture transport and consequent expansion in wood, a simple approach is seen to describe the frequency behavior of both moisture content and expansion in cubic oak blocks well. The assumption of the sample being a first-order linear system provides a powerful scaling parameter in terms of a dimensionless frequency, dependent on the size of the sample and the diffusion coefficient. The frequency dependence of the amplitude in both moisture content and expansion can then effectively be scaled such that all amplitudes of different sample sizes are on one single curve. The moisture content and expansion amplitudes are seen to be related by a hygroscopic expansion coefficient of ~0.3, which is in accordance with values in literature. This furthermore suggests a one-on-one relation between moisture content and expansion.

The detailed study of moisture penetration during sinusoidal relative humidity fluctuations demonstrates the dominance of the longitudinal direction on the overall transport in oak. The moisture content amplitude with transport in the longitudinal direction is large compared to transport in radial or tangential direction. Even though the side sealing is found to be improper, resulting in all-sided exposure instead of one-dimensional transport, the results clearly illustrate the decay of amplitude in moisture content away from the exposed surface. The minor moisture penetration after proper side sealing in a radial sample additionally indicates the major contribution of the longitudinal direction to the moisture transport.

The evolution of the T_2 relaxation time distribution over time during sinusoidal relative humidity fluctuations provides valuable information about the moisture present in the system. During these exposure conditions the distribution shifts sinusoidally too. This gives rise to a conceptual model in which this shift is attributed to more moisture between the microfibrils in the cell wall, forcing the cell wall constituents apart and thereby enlarging the volume-to-surface ratio of moisture. As a consequence, not only the T_2 average changes, but also the bounds of the T_2 distributions. When expansion is measured concurrently, an increase in moisture content is found to be accompanied by an increase in T_2 and expansion. This suggests an interrelation between the three quantities, i.e. that the same mechanism is responsible for a change in moisture content, T_2, and expansion.

4 HYGROMORPHIC RESPONSE DYNAMICS FROM A SIMPLE BENDING EXPERIMENT

When a wood board is exposed to a change in relative humidity on only one of its surfaces, the resulting asymmetric moisture content profile induces differential expansion over the thickness. Consequently a bending moment causes the board to curve. A simple theory is presented to describe the bending of a wood board due to a step change in relative humidity. The conceptual idea of the process is shown in Figure 4.1. We consider a homogeneous, isotropic, and linearly elastic wood board with a thickness much smaller than its length and width, clamped at one end. The board has an impermeable layer on five surfaces, while one surface is exposed to the atmosphere surrounding it, provoking semi one-dimensional moisture transport. Here we will assume that the impermeable layer has no influence on the mechanical behavior of the board. The board itself is initially in equilibrium with the surrounding air, and therefore has a flat moisture content profile (Figure 4.1a), when suddenly the relative humidity of the surrounding air is changed. The moisture content at the exposed surface consequently rises, and moisture is transported into the material resulting in a moisture gradient. The consequent asymmetric moisture profile causes unequal expansion over the thickness; the expansion near the exposed surface is the highest and decreases towards the coated surface. These differences in expansion result in a constant moment, and as a consequence the board bends (Figure 4.1b). Due to moisture transport, the moisture profile continuously changes and consequently the bending changes continuously over time. The deflection has a maximum in time when the moment induced by the differences in expansion is the largest. Progressing in time, the moisture starts to equilibrate throughout the sample and the moisture content becomes homogenous again. In the final situation the board is straight again, but elongated in length due to the moisture increase (Figure 4.1c).

By analyzing the bending in time after a sudden increase in relative humidity we can obtain the diffusivity and the hygroscopic expansion. We will first discuss the theory. Experimental verification is provided using a device to generate an air flow with adjustable relative humidity. The postulated step change in relative humidity is, however, not very realistic since changes of environmental conditions are continuous, often manifested in daily or seasonally repeating cycles (Forest Products Laboratory, 2010). Nevertheless, the hygromorphic step response of the board can provide information on the frequency response characteristics. The behavior at very low frequencies, which is time-consuming to determine experimentally, can thus be retrieved from a short experiment. We will discuss the theory to derive the frequency response, and the experimental verification including sinusoidal relative humidity fluctuations.

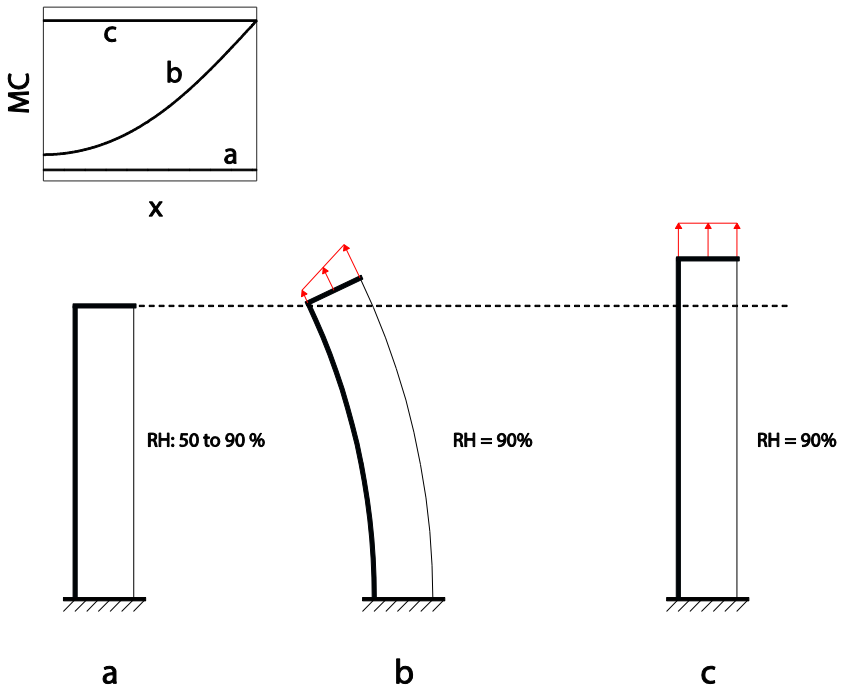

Figure 4.1: *The conceptual idea of the bending experiment due to a inhomogeneous moisture content profile. A board of hygromorphic material with thickness d is exposed to a step change in the ambient relative humidity at one side. The board is sealed on all sides except the one exposed to the environment, resulting in a semi one-dimensional moisture diffusion experiment. a) The sample is initially in equilibrium and the moisture content is constant throughout the sample. b) After a sudden increase in relative humidity a moisture gradient in the sample results in a bending moment due the differential expansion. c) In the final situation the moisture has equilibrated throughout the sample and the board is straight again, but elongated due to a higher moisture content.*

4.1 HYGRO-BENDING THEORY

In this section, the bending of a clamped hygromorphic board, sealed on five of its six sides, is described by introducing a so-called hygro-bending theory. First the moisture transport arising from a sudden change of the ambient relative humidity will be described analytically. A simple, linear elastic model is then proposed to express the consequent bending of the board. The configuration of the board as used in the bending analysis is shown in Figure 4.2.

4.1.1 MOISTURE TRANSPORT

A step change in the moisture content at one surface of the board results in one-dimensional moisture transport. Here we will assume that moisture transport is characterized by a constant diffusion coefficient D throughout the thickness d. Initially the board has a constant moisture content c_0. At a certain moment the relative humidity is increased stepwise resulting in a prescribed moisture content c_d on one surface. The other surface is sealed and therefore has a no-flux boundary condition. Mathematically this can be formulated as:

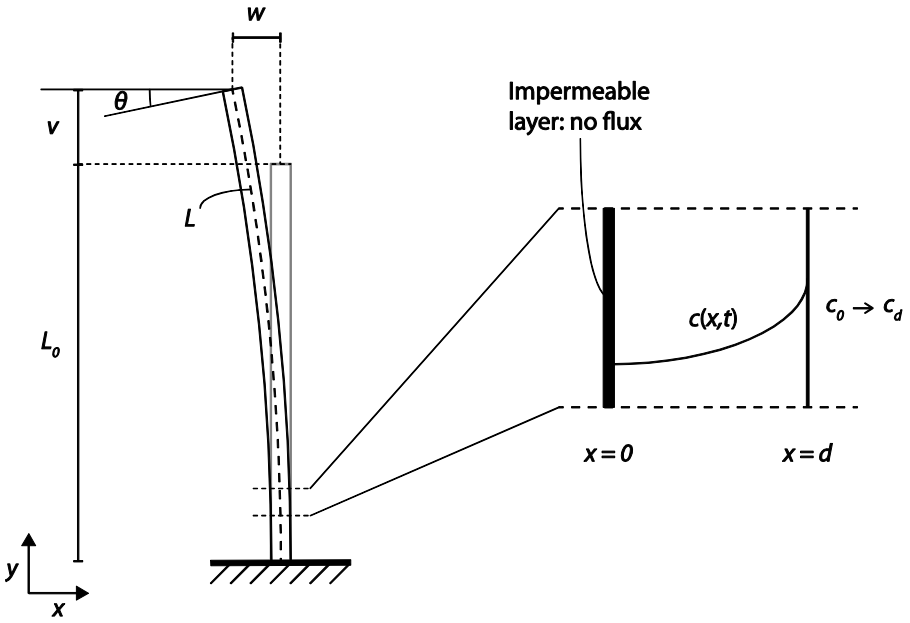

Figure 4.2: *Schematic representation as used in the theory of the bending of a board with initial length L_0 and thickness d, exposed on one surface to a change in moisture content.*

$$\begin{cases} \partial_t c = D\partial_{xx} c, \\ c(x,0) = c_0 \\ c(d,t) = c_d, \\ \partial_x c(0,t) = 0. \end{cases} \tag{4.1}$$

An analytical solution can be obtained by separation of variables, (see (Strauss, 2008)). The result can be formulated in the form of the Fourier series:

$$c(x,t) = c_d + \sum_{n=0}^{\infty} a_n \, \mathrm{e}^{-D\beta_n^2 t} \cos(\beta_n x), \tag{4.2}$$

with components

$$a_n = \frac{4(c_0 - c_d)}{(2n+1)\pi}(-1)^n, \quad \beta_n = \frac{2n+1}{2d}\pi. \tag{4.3}$$

4.1.2 TRANSIENT BENDING

A change in moisture content in a hygromorphic material results in expansion or shrinkage. In case of a uniform moisture distribution *c* and no lateral contraction, the length of the board is given by

$$L(t) = L_0\left[1 + \alpha\left(c(t) - c_0\right)\right], \tag{4.4}$$

where L_0 is the length of the board at time t_0, α the linear hygroscopic expansion coefficient, and c_0 the uniform moisture content at time t_0. During one-sided exposure, the moisture content will not be uniform. As a result the time-evolution of the length of the board can no longer be described by Eq. (4.4). Due to the uneven expansion across the thickness, the board bends. In order to describe the bending of the board, the assumption is made that the material is linearly elastic with no lateral contraction. The thickness of the board can thus be schematically represented by a system of springs, connected to each other on top by an infinitely stiff beam (for a more in-depth discussion see Appendix). By doing so, the length of the board at half-thickness can be expressed as

$$L(t) = L_0\left[1+\frac{\alpha}{d}\int_0^d\left(c(x,t)-c_0\right)dx\right]. \tag{4.5}$$

Note that for a constant moisture content, Eq. (4.5) simplifies to Eq. (4.4). The bending of the board can be characterized by the tangent of the angle of its cross-section (see Figure 4.2):

$$\theta(t) = 12\frac{\alpha L}{d^3}\int_0^d c(x,t)\left(x-\frac{d}{2}\right)dx. \tag{4.6}$$

Here the integral represents the moment exerted on the board as a consequence of an unsymmetrical moisture content distribution. It can be shown that for the general case of a symmetric moisture content profile, i.e. $c(x,t) = c(d-x,t)$, the integral in Eq. (4.6) vanishes and the angle of the cross-section of the board equals zero. In case of a two-sided exposure to a change in relative humidity there will be no deflection, only an expansion in the y-direction. In case of a one-sided step change, the moisture profile will approach the constant value c_d for $t \to \infty$, and consequently the angle θ approaches zero again.

The bending of the board causes deflection, which is maximal at the free end of the board. The x-deflection at the free end at half-thickness is given by (see Appendix D):

$$w(t) = \frac{L}{\varphi}(1-\cos\varphi), \tag{4.7}$$

and the corresponding y-deflection can be expressed as:

$$v(t) = \frac{L}{\varphi}\sin\varphi - L_0, \tag{4.8}$$

where $\varphi = \tan^{-1}\theta$. Under the assumption that the deflection of the beam remains small, i.e. $\varphi \approx \theta$, a compact expression for the deflection can be derived by taking into account only the first two terms of the Taylor series expansion of Eq. (4.7) and assuming $L_0 \approx L$:

$$w(t) = 6\frac{\alpha L_0^{\,2}}{d^3}\int_0^d c(x,t)\left(x-\frac{d}{2}\right)dx. \tag{4.9}$$

To obtain an analytical expression for the length L after a step change in the moisture content at one surface, Eq. (4.2) is substituted in Eq. (4.5) to yield

$$L(t) = L_0 \left[1 + \alpha (c_d - c_0) + \frac{\alpha}{d} \sum_{n=0}^{\infty} a_n \, \mathrm{e}^{-D\beta_n^2 t} \frac{(-1)^n}{\beta_n} \right]. \tag{4.10}$$

Similarly, Eq. (4.2) is inserted in Eq. (4.9) to arrive at an explicit expression for the deflection

$$w(t) = 6 \frac{\alpha L_0^{\,2}}{d^3} \sum_{n=0}^{\infty} a_n \, \mathrm{e}^{-D\beta_n^2 t} \left(\frac{d(-1)^n}{2\beta_n} - \frac{1}{\beta_n^{\,2}} \right). \tag{4.11}$$

Eq. (4.10) and (4.11) may be approximated by taking into account only a finite number of components of the infinite sum. In Figure 4.3 the calculated deflection over time is plotted with Eq. (4.11) using 1, 2 and 100 components. Since the higher order terms decay fast due to higher exponential decay constants, all terms converge to the first component over time. As can be seen the total behavior is well described by two components. Before the maximum is reached, the terms for $n > 1$ have no serious influence anymore. The contribution of these higher order terms is only significant at small times, especially in the initial value. In the remainder of the study, the length in Eq. (4.10) and the deflection in Eq. (4.11) will be approximated by the first two components of the infinite sum. The approximated evolution of the length of the board over time can thus be expressed as

$$L_a(t) = L_0 \left[1 + \alpha (c_d - c_0) \left(1 - \frac{8}{\pi^2} e^{-D\left(\frac{\pi}{2d}\right)^2 t} - \frac{8}{9\pi^2} e^{-D\left(\frac{3\pi}{2d}\right)^2 t} \right) \right]. \tag{4.12}$$

Approximation of Eq. (4.11) with two components yields for the x-deflection of the board

$$w_a(t) = 24 \frac{\alpha L_0^{\,2}}{\pi^2 d} (c_0 - c_d) \left[\left(1 - \frac{4}{\pi} \right) e^{-D\left(\frac{\pi}{2d}\right)^2 t} + \frac{1}{9} \left(1 + \frac{4}{3\pi} \right) e^{-D\left(\frac{3\pi}{2d}\right)^2 t} \right]. \tag{4.13}$$

To find the time t_m at which the maximum deflection occurs we can take the zero of the derivative with respect to time:

$$t_m = \frac{d^2}{2\pi^2 D} \ln\left(\frac{1}{3} \frac{3\pi + 4}{4 - \pi} \right). \tag{4.14}$$

Hence the time at which the board is deflected maximally is proportional to the typical diffusion time d^2 / D. Inserting t_m into Eq. (4.13) yields the maximum deflection of the board

$$w_m = 24 \frac{\alpha L_0^{\,2}}{\pi^2 d} (c_0 - c_d) \left[\left(1 - \frac{4}{\pi} \right) \left(3 \frac{4 - \pi}{3\pi + 4} \right)^{\frac{1}{8}} + \frac{1}{9} \left(1 + \frac{4}{3\pi} \right) \left(3 \frac{4 - \pi}{3\pi + 4} \right)^{\frac{9}{8}} \right]. \tag{4.15}$$

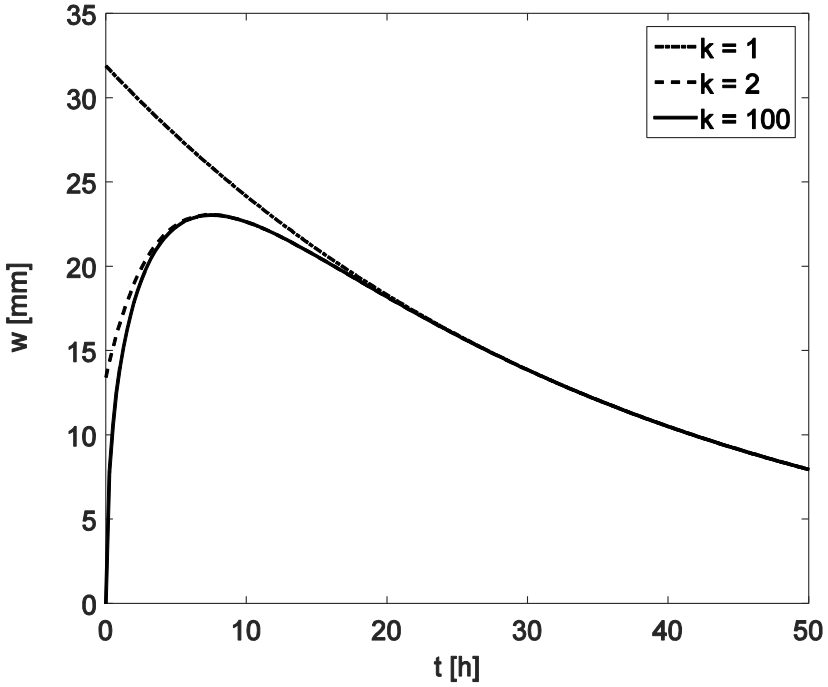

Figure 4.3: *The calculated deflection as a function of time by approximating with 1, 2 or 100 components (see Eq. (4.11)). Values used in the calculation are: $\alpha = 0.4$, $L_0 = 80$ mm, $d = 4$ mm, $D = 5 \cdot 10^{-11}$ m^2/s, $c_0 = 0.1$, $c_d = 0.2$.*

As can be seen, the maximum deflection is proportional to the linear expansion coefficient, the length of the board squared, and the step in moisture content at the surface, and inversely proportional to the thickness of the board. It also appears that the maximum deflection is independent of the diffusion coefficient. The diffusion coefficient only plays a role in the time at which the maximum occurs. By performing an experiment with a board of thickness d, the diffusion coefficient can be derived from the results by rewriting Eq. (4.14) to arrive at

$$D = \frac{d^2}{2\pi^2 t_m} \ln\left(\frac{1}{3}\frac{3\pi + 4}{4 - \pi}\right). \tag{4.16}$$

Hence by analyzing the bending response of a board during a step change in the ambient relative humidity the diffusivity can be obtained. The linear hygroscopic expansion coefficient α can be derived from Eq. (4.12) as the asymptote of the length for $t \to \infty$. Furthermore, Eq. (4.15) provides us a scaling law with which experimental results using boards of different thicknesses can be compared.

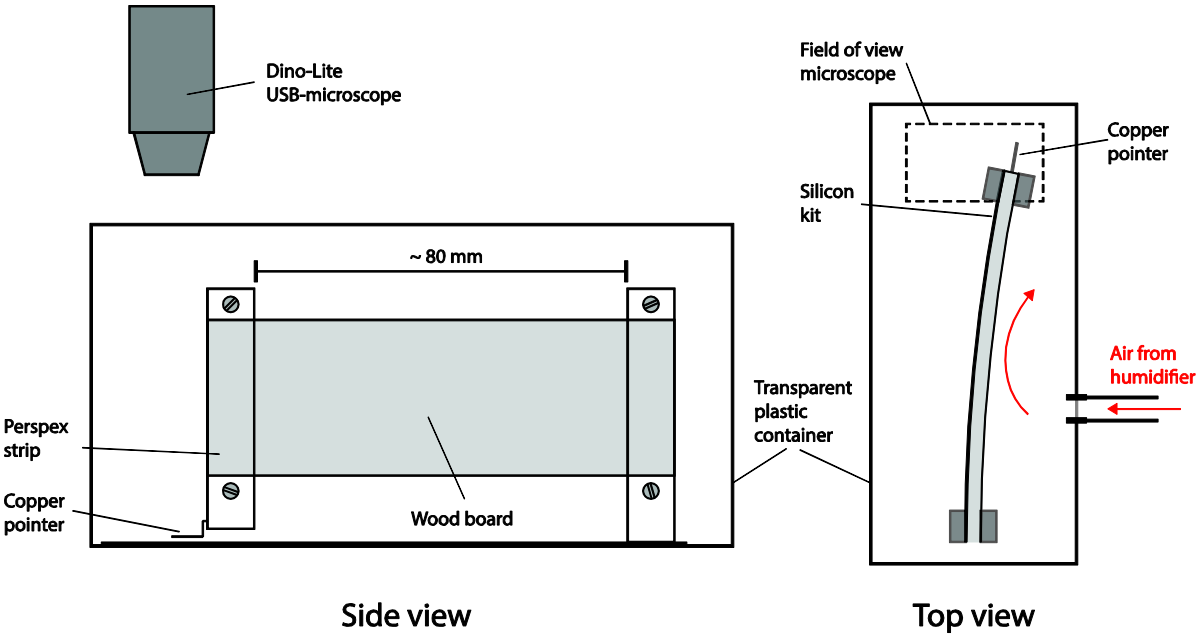

Figure 4.4: *The experimental set-up for measuring the bending of an oak wood board under dynamic humidity conditions. On the left, the side view of the experimental set-up is shown, the top view is shown on the right.*

4.2 MATERIALS AND METHODS

Experiments were conducted on oak boards where the bending due to one-sided exposure to a change in relative humidity is assessed. First, the material of interest and the preparation of samples are described, after which the experimental procedure is elucidated with the description of the set-up.

Oak boards with a length of 100 mm, a width of 30 mm, and different thicknesses (2, 4, 6, 8 mm) were sawn from a large oak wood board. Because wood is an anisotropic material with properties dependent on the characteristic directions, attention is paid to the grain direction in the samples. All samples are prepared such that the grain direction is along the width of the board. Perpendicular to that, the tangential direction is in the length of the board, and the radial direction along the thickness. Transport will hence occur in the radial direction of the wood, whereas the expansion along the length of the board is the expansion in tangential direction. Since all experiments start at a relative humidity of 50 %, the boards are placed in a desiccator containing a saturated $Mg(NO_3)_2 \cdot 6H_2O$ solution, ensuring a relative humidity of 53 %. Prior to the experiment, Bison silicone kit© is applied on five sides of the board, leaving one of the two largest surfaces open. The silicone kit was allowed to dry for at least one day.

The experimental set-up designed to measure the deflection of a wood board due to humidity fluctuations is shown in Figure 4.4. One end of the wood board is clamped between two PVC strips. The other end of the sample is also clamped between two strips, on which a pointer is mounted. This set-up is placed in a plastic container in which the relative humidity can be controlled by the help of a humidifier, which was introduced in Section 2.2. A Dino-Lite© digital microscope records images to measure the deflection. Using a Matlab optical

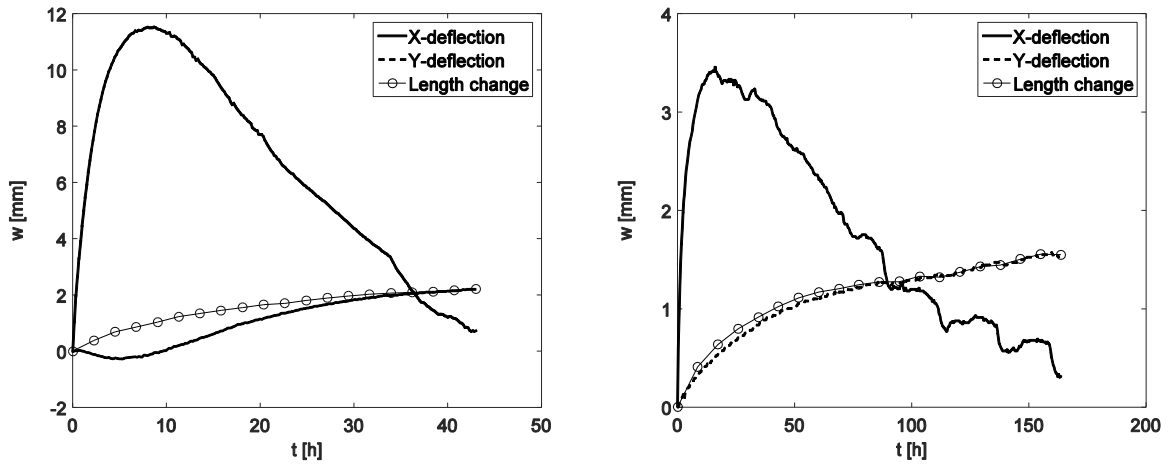

Figure 4.5: *The deflection of the free end and the length change of a clamped board at half-thickness due to a step change in the relative humidity of the ambient air from 50 to 90 %. Results are shown for thicknesses of 4 mm (left) and 8 mm (right).*

recognition program the position of the pointer is recorded automatically. The image analysis procedure is explained in more detail in Appendix E, along with the correction procedure to account for the attached pointer.

4.3 RESULTS AND DISCUSSION

4.3.1 STEP RESPONSE

We have first measured the step response of boards with various thicknesses. In Figure 4.5 the deflection at half thickness of the free end of the board is shown as a function of time after a step change in the relative humidity from 50 to 90 %. Here the deflection in both directions is shown for thicknesses of 4 mm and 8 mm. The characteristic shape as predicted from the theory is seen. After the step change in relative humidity the board immediately starts to bend up to a maximum deflection, subsequently it more slowly bends back towards its initial x-position. The deflective response in the y-direction is dependent on the thickness of the board, since it is caused by two processes. Pure geometrically, the bending of an initially straight board causes a change in the y-position of its end. In case of a hygro-expansive material, the length of the board also changes during moisture sorption. This double effect causes the y-position of the end of the board to first decrease before increasing, if the x-deflection happens faster than expansion. In a thicker board, which deflects less in the x-direction, expansion dominates and no initial dip in the y-position is recorded. In the experimental results of the 8 mm thick board, some random fluctuations in the deflection are observed, especially after reaching the maximum, which might be contributed to the inhomogeneity of wood. Local variation in the wood structure may result in local variations in the moisture transport and/or expansion. As a result, the expansion and consequently the deflection, may show time-dependent effects.

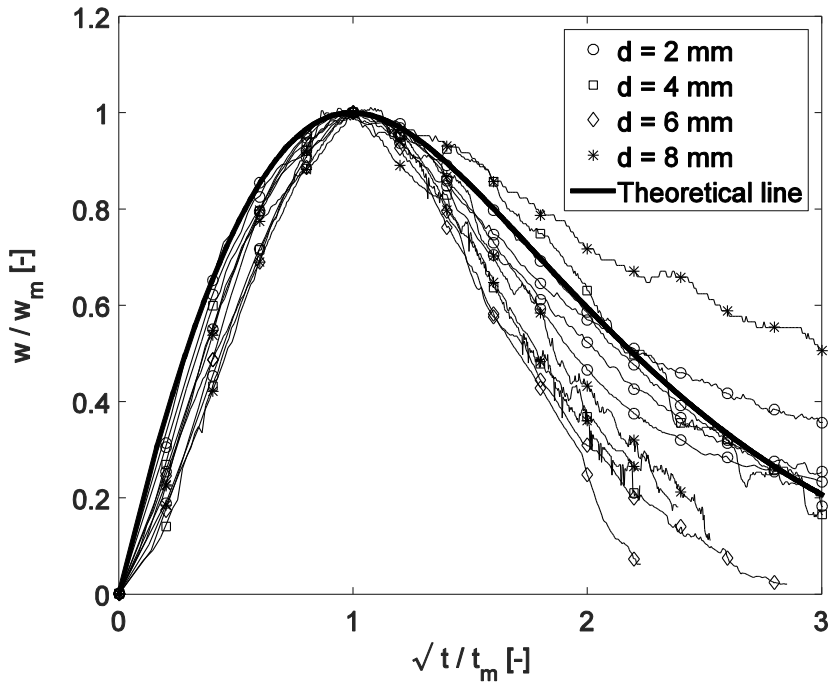

Figure 4.6: *The scaled x-deflection, plotted as a function of the square root of the normalized time for samples with thicknesses of 2,4,6 and 8 mm.*

The x-deflection scaled by the maximum deflection w_m is plotted in Figure 4.6 as a function of the square root of the scaled time by t_m, for different thicknesses of the board. It is seen that the theory overestimates the velocity of initial deflection up to the maximum deflection, but predicts a slower back-deflection than seen from experiments for most boards. Nevertheless, the same characteristic behavior is seen for all samples. After reaching the maximum deflection some deviations are observed between the boards. This can most probably be attributed to the inhomogeneous nature of wood, as postulated before. Apparently the influence of inhomogenieties is small during the initial stage of the bending, but more pronounced in the second stage, where the board bends back. Local inhomogeneities can also explain the feature found in the experimental results of a 2 mm thick board, where a rather permanent deformation is seen. This occurred for instance when the relative humidity was elevated to 90 % from its equilibrium position 50 %, but seen to be reversible when the relative humidity was decreased to 50 % again. The same effect causes the warping of thin wood boards in equilibrium with a changed relative humidity (Reichert, et al., 2015). The influence of these small scale effects is relatively large in a thin board, whereas these differences are more leveled out in a thicker board.

To derive the diffusion coefficient D and the linear hygroscopic expansion coefficient α from the experimental results, some additional steps need to be taken. The x-deflection is first fitted with the double exponential function

$$x(t) = \beta\left(e^{-c_1 t} - e^{-c_2 t}\right), \tag{4.17}$$

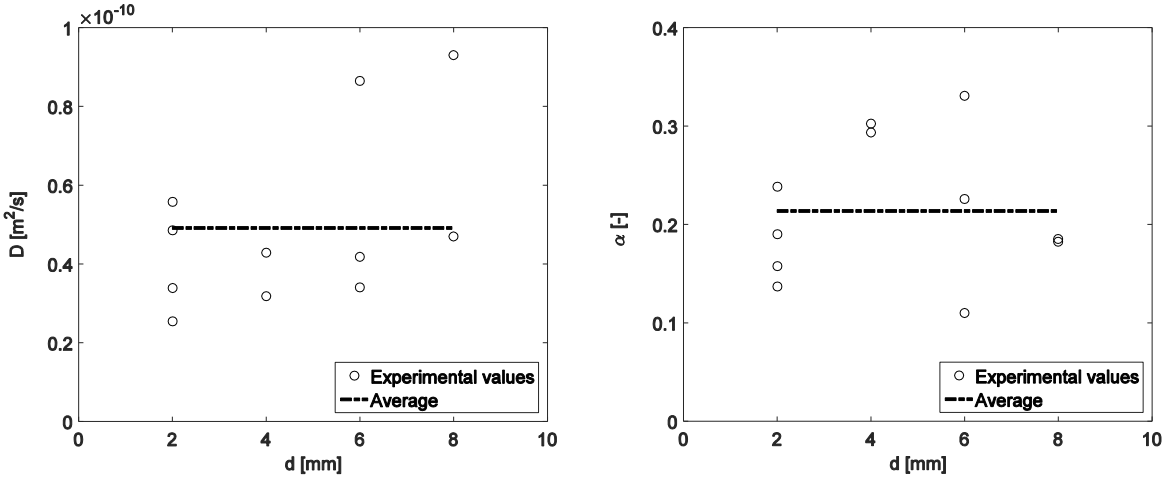

Figure 4.7: *Diffusion coefficient D (left) and linear hygro-expansion coefficient α (right) for different thicknesses.*

where β, c_1, and c_2 are fitting parameters. Note that Eq. (4.17) has a similar form as Eq. (4.13), only the initial values of the exponential terms are chosen such that their sum is zero. Furthermore we have disregarded $c_2 = 9c_1$ to obtain the optimal fit. Eq. (4.17) has a maximum at the time

$$t_m = \frac{1}{c_2 - c_1} \ln\left(\frac{c_2}{c_1}\right). \tag{4.18}$$

Substitution of Eq. (4.18) in Eq. (4.17) yields the maximum deflection. The diffusion coefficient can be calculated by substitution of t_m in Eq. (4.16). Analogous to the x-deflection the y-deflection can be fitted by:

$$y(t) = \beta_3\left(e^{-c_3 t} - 1\right) + \beta_4\left(e^{-c_4 t} - 1\right), \tag{4.19}$$

where β_3, c_3, β_4 and c_4 are fitting parameters. For $t \to \infty$ the x-deflection approaches zero, and consequently the y-deflection approaches the length change of the board. With Eq. (4.10) the product α (c_1 - c_0) can be derived from Eq. (4.19) as -(β_3 + β_4). Since the step in ambient relative humidity is known instead of the step in moisture content, an additional operation needs to be performed to obtain the expansion coefficient α. The step in moisture content is calculated with a general sorption isotherm for wood proposed in literature (Forest Products Laboratory, 2010). A step in relative humidity from 50 % to 90 % at T = 293 K results in c_d - c_0 = 0.11. This results is used to retrieve the expansion coefficient.

The diffusion coefficients and linear hygroscopic expansion coefficients derived from experiments are plotted in Figure 4.7 for different thicknesses. The diffusion coefficients found are in the range of 2-9·10^{-11} m^2/s, with an average of 5·10^{-11} m^2/s. This value is in accordance with values reported in literature for oak (Simpson, 1993) (Saft & Kaliske, 2013). Quite a large scatter is found in the expansion coefficients. Different boards are used in the experiments; microstructural differences can cause different moisture capacities or expansion

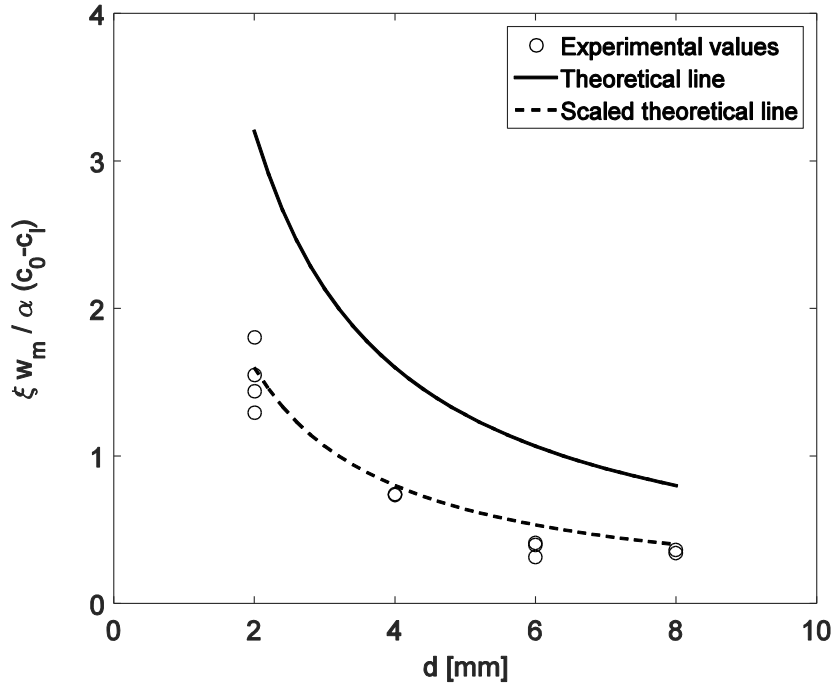

Figure 4.8: *Scaled values for the maximum deflection w_m, resulting from application of Eq. (4.15) to experimental results, with ξ the constant in Eq. (4.15). The solid theoretical line represents L^2/d, which is also plotted scaled by a factor ½ to show the qualitative resemblance of experimental and theoretical values.*

coefficients. The average of the derived expansion coefficients (0.21) is somewhat lower than values reported in literature for the tangential expansion of oak (~ 0.3). This is most probably caused by the negligence of lateral contraction. A correction factor of $1/(1-\nu)$, with ν the Poisson ratio, can be applied to arrive at a similar expression as in the case of thermal expansion (Gatewood, 1957). With $\nu = 0.35$ (Saft & Kaliske, 2013), the corrected expansion coefficient is comparable with values found in literature (Noack, et al., 1973; Caré, et al., 2012; Saft & Kaliske, 2013).

In Figure 4.8 we have plotted the maximum deflection scaled by the linear hygroscopic expansion coefficient and the step in moisture content, as a function of the thickness (see Eq. (4.15)). The theoretical line representing L^2/d should ideally overlay the experimental results. However, a theoretical overestimation of the maximum deflection is seen. Scaling the theoretical line by a factor ½ results in a more accurate description of the experimental results. The qualitative scaling behavior of $1/d$ is thus followed by experiments with different thicknesses, but the absolute values are overestimated, which may have several causes. In the present theory, it is assumed that the surface of the board reaches equilibrium with the surrounding air immediately. A stationary boundary layer at the surface can, however, increase resistance to moisture sorption. If the transport of moisture is limited by the resistive boundary layer, less asymmetry in the moisture profile is expected over time. As a consequence, the deflective response of the board is less intense. In the experimental set-up used in this study, humid air is blown into the plastic container with a flow such that the air in the container is refreshed at least once a minute. It is therefore presumed that no stagnant

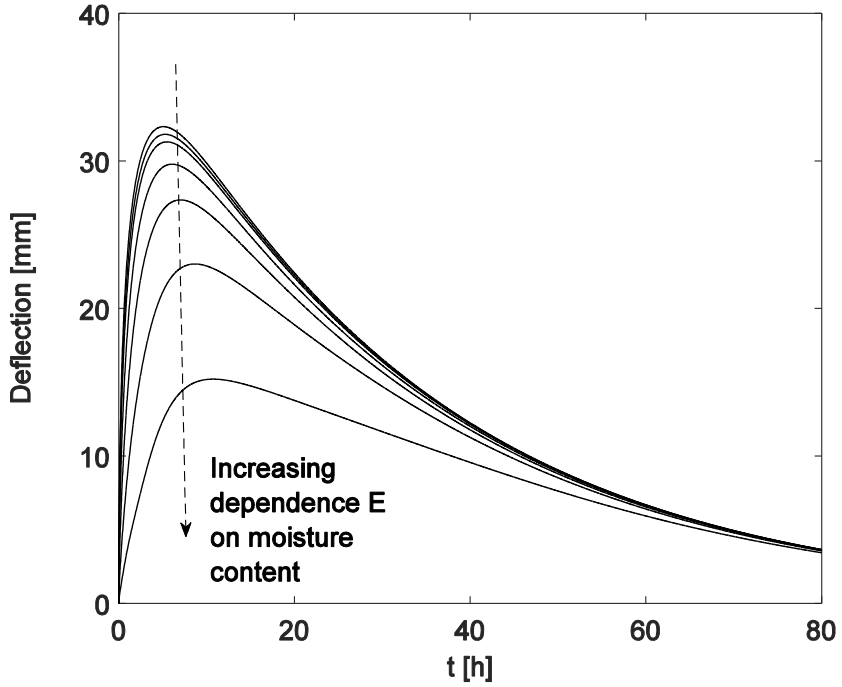

Figure 4.9: *The deflection over time after a step change in the moisture content at one surface of a board with a thickness of 4 mm, for different dependencies of the E-modulus on the moisture content. The E-modulus is assumed to have the form* $E = 10^{b-kc}$ *Pa, with b = 10 and k = 0, 1, 2, 5, 10, 20, or 50.*

boundary layer is formed which attenuates moisture sorption. A more probable cause of the overestimated maximum deflection values is the assumption of wood as a homogeneous, isotropic, and linearly elastic material. Local structural fluctuations can, e.g., lower the moisture content asymmetry over time, decreasing the deflection. Also expansion is presumed to follow the change in moisture content immediately, whereas in literature viscoelastic effects are assigned to wood (Schniewind & Barrett, 1972). These time-dependent effects can attenuate the bending of the board.

To determine the effect of viscoelasticity on the transient bending of a board, some simple numerical calculations are performed. The E-modulus is allowed to be dependent on the moisture content, which leads to similar effects as viscoelasticity (Scherer, 2016). Due to the analogy, the result from the warping of a gel plate due to a thermal gradient as presented by Scherer (1987) is used. The deflection of the end of a fixed board can then be described by

$$w = \frac{{L_0}^2}{2} \frac{f_1 g_0 - f_0 g_1}{{g_1}^2 - g_0 g_2}, \tag{4.20}$$

with

$$f_n = \alpha \int_0^d E\left(c - c_0\right)\left(x - \frac{d}{2}\right)^n dx, \quad g_n = \int_0^d E\left(x - \frac{d}{2}\right)^n dx. \tag{4.21}$$

Note that an extension of the analysis presented in Appendix D by assuming a non-constant spring constant yields the same result. Numerical calculations are performed on a board with a thickness d of 4 mm, responding to a step change at the surface from an initial moisture content c_0 of 0.1 to a moisture content of 0.2, with an expansion coefficient α = 0.4. The moisture profiles $c(x,t)$ are described with Eq. (4.2), and the deflection with Eq. (4.20), where the modulus is assumed to have the form $E = 10^{b-k.c}$ Pa. The value for b is assumed to be 10, calculations are then performed with increasing values for k (k = 0, 1, 2, 5, 10, 20, 50). The results of the calculations are shown in Figure 4.9, which illustrates that with increasing dependence of the E-modulus on moisture content, the deflection decreases. For k = 50, the maximum deflection has a value of approximately one half of a constant E (i.e. k = 0), which would account for the over prediction with a factor 2 of the presented analysis in Figure 4.8. This value, however, entails that the E-modulus drops to 0 at a moisture content of 0.2, which is obviously not realistic. More realistic values, as proposed by, e.g., Saft and Kaliske (2013), would result in $k \approx 0.5$, which is seen to have no significant influence on the deflection of the board. This result implies that viscoelastic effects cannot account for the observed discrepancies in deflection between theory and experiments. A more probable cause of the differences is the assumption that moisture transport can be described by a single diffusion equation for both water vapor transport in the lumens and moisture transport in the cell wall. The validity of this approach has been doubted by some authors (Wadsö, 1994), and simulations have been performed with the two transport mechanisms treated separately, coupled by a sorption rate term (Dvinskikh, et al., 2011; Eitelberger, et al., 2011). Knowledge about the moisture content profile during the experiment, e.g., by NMR, is expected to shine a light on the transport part of the process.

4.3.2 FREQUENCY RESPONSE

To derive frequency response characteristics from a step response, the deflective behavior of the wood board is considered as the dynamic response of a linear system (Franklin, et al., 1994). The frequency response for the x-deflection can be obtained by first determining the Laplace transform of Eq. (4.17) in terms of the complex variable s:

$$X(s) = \mathcal{L}\left(x(t)\right) = \beta\left(\frac{1}{c_1 + s} - \frac{1}{c_2 + s}\right). \tag{4.22}$$

Eq. (4.17) is the response of the linear system to a step change in the moisture content at the surface at t = 0. Since the board is approximated by a linear system, only the difference in initial and final value of the moisture content are of interest, not the actual values. The step change $u(t)$ can therefore be written as

$$u(t) = a, \tag{4.23}$$

where a is the step in moisture content. The Laplace transform of Eq. (4.23) is:

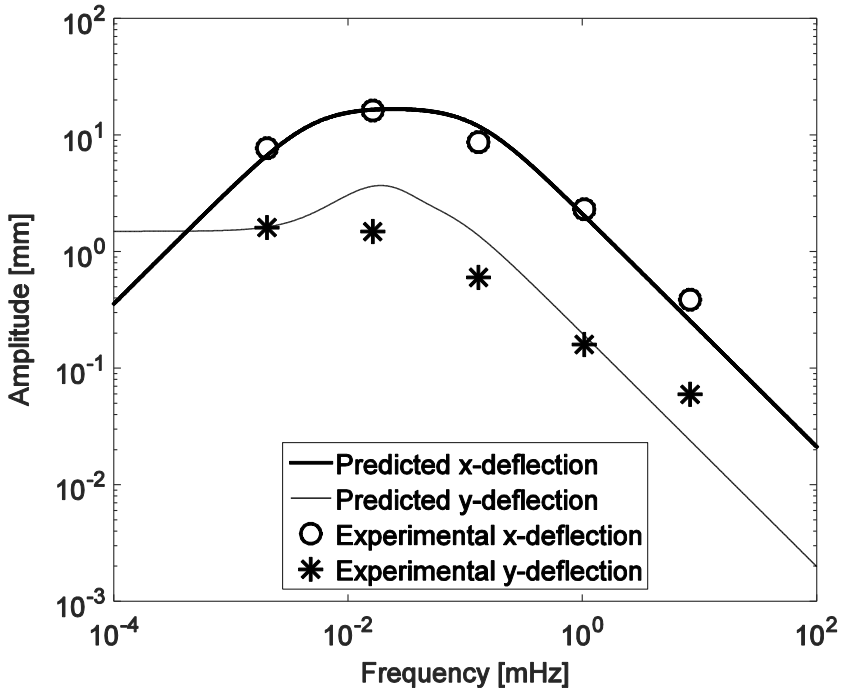

Figure 4.10: *Bode amplitude plots for the x- and y-deflection of a 2 mm thick board, which results from application of Eqs. (4.26) and (4.27) to a step change from a relative humidity of 50 to 90 %. For the experimental values, the slowest variation is 134 hours, the fastest 2 minutes.*

$$U(s) = \frac{a}{s}. \tag{4.24}$$

In a linear system, the Laplace transforms X and U of the output and input function respectively, are related by:

$$X(s) = H(s)U(s), \tag{4.25}$$

where $H(s)$ is the transfer function of the system. Note that this relation holds for all input functions $u(t)$ for which a Laplace transform exists. As a consequence, if the transfer function of a system is known, the inverse Laplace transform of Eq. (4.25) will yield the transient response $x(t)$ of the system to an arbitrary input $u(t)$. Using Eqs. (4.22) and (4.24) in Eq. (4.25), the transfer function of the x-deflection can be expressed as

$$H(s) = \frac{s\beta(c_2 - c_1)}{a(c_1 + s)(c_2 + s)}. \tag{4.26}$$

If the transfer function of the system known, its frequency response can be determined by considering the real and imaginary parts of $H(j\omega)$, with ω the angular frequency. $H(j\omega)$ is a vector in the complex plane; its magnitude is the amplitude of the steady-state output signal to a sine input signal with unit amplitude, and its angle with the positive real axis determines the phase shift of the output signal. Using these results, a Bode amplitude plot can be constructed

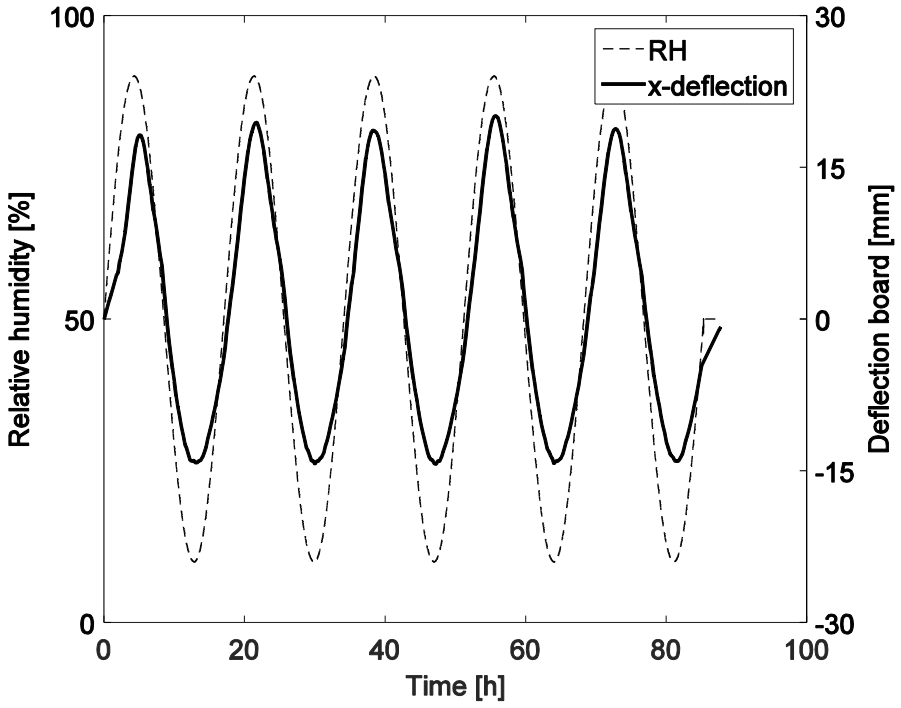

Figure 4.11: *Experimental x-deflection of a 2 mm thick board during sinusoidal relative humidity (RH) fluctuations.*

which shows the amplitude on a logarithmic scale as a function of frequency. A similar analysis can be performed to determine the frequency dependence of the y-deflection of the board. The transfer function of the y-deflection can be obtained using Eq. (4.24) and the Laplace transformation of Eq. (4.19) as

$$G(s) = \frac{s\left(\beta_3 c_4 + \beta_4 c_3 + s\left(\beta_3 + \beta_4\right)\right)}{a\left(c_3 + s\right)\left(c_4 + s\right)}. \tag{4.27}$$

In a similar fashion, the frequency behavior of the y-deflection can be calculated by considering the real and imaginary part of $G(j\omega)$.

Based on this approximation we can determine the frequency response of a 2 mm thick board from a single step experiment. In Figure 4.10 the predicted Bode amplitude plots of the deflection of the board in x- and y-direction are given as a function of the frequency. Three regimes can be distinguished. At low frequencies, the board is seen to deflect to a small extent in the x-direction, but its amplitude in the y-direction reaches a constant value. In an intermediate frequency interval, the board reacts heavily to the imposed fluctuations in relative humidity. For increasing frequencies, the amplitude in both x- and y-deflection is seen to decline; the variations in relative humidity are too fast to follow.

In order to verify the frequency response we have conducted experiments in which the relative humidity was varied sinusoidally at different frequencies. The equilibrium relative humidity was 50 % and the amplitude 40 % in all experiments. The result of one of these measurements for a board with a thickness of 2 mm is given in Figure 4.11. The board is seen

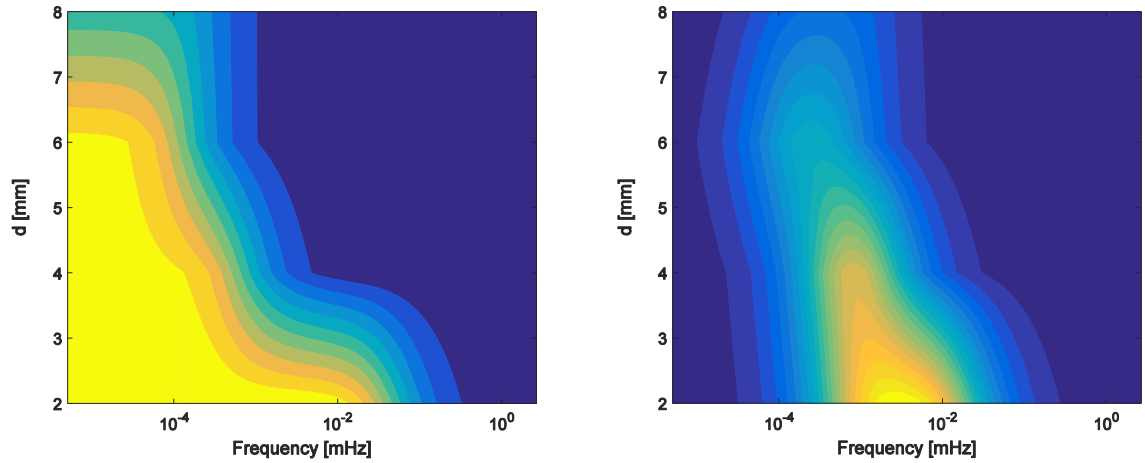

Figure 4.12: *Contour plots of the frequency behavior of the expansion of the board (left), and the x-deflection (right), as a function of the thickness. The frequency on the x-axis spans the range of periods from 1 year to 1 minute.*

to deflect cyclically to the imposed relative humidity variations. Furthermore it is seen that the deflection during moisture adsorption is slightly larger than during desorption. This can be explained with the sorption curve of wood, which has an S-shape with a relatively large increase at high relative humidity (Skaar, 1988). Although the input, i.e. the relative humidity, has a pure sinusoidal shape, the non-linearity of the sorption curve causes the moisture content at the exposed surface to follow a transformed course over time. As a result, the deflection of the board is not pure sinusoidal. In Figure 4.10 we have also plotted the results from individual experiments with sinusoidally varying relative humidity at different frequencies. As can be seen these results overlap well with the frequency response as calculated from a single step experiment. Some quantitative deviations between predicted and experimentally found values are encountered, especially with the y-deflection. As mentioned earlier, the y-deflection has a dual source: it arises as a geometrical consequence of the bending and is caused by expansion/shrinkage. This explains the peak in the predicted curve, which is not seen to be confirmed by experiments.

The Bode amplitude plots for expansion and x-deflection are shown in a contour plot in Figure 4.12 for different thicknesses. The amplitude plots result from the Laplace transform of the step response of individual boards, as described above. Bright areas indicate a high intensity, i.e. a large length change or x-deflection. In the contour plot of the length change, a clear trend is visible with high intensity regions in a larger span of frequencies for a thin board. A thin board will expand to a large extent at a higher frequency compared to a thicker board. In other words, a fast fluctuation will result in a larger length change of a thinner board when unconstrained. This is consistent with previous results in Chapter 3 concerning the expansion of cubic blocks. Furthermore, Figure 4.12 illustrates the x-deflection over a wide range of frequencies for different thicknesses, which elucidates two important features. First of all, the intensity is higher for smaller thicknesses, which is consistent with the theory and results presented in this chapter. Besides the lower intensity, the frequency of the maximum intensity also shifts towards lower values for increasing thickness.

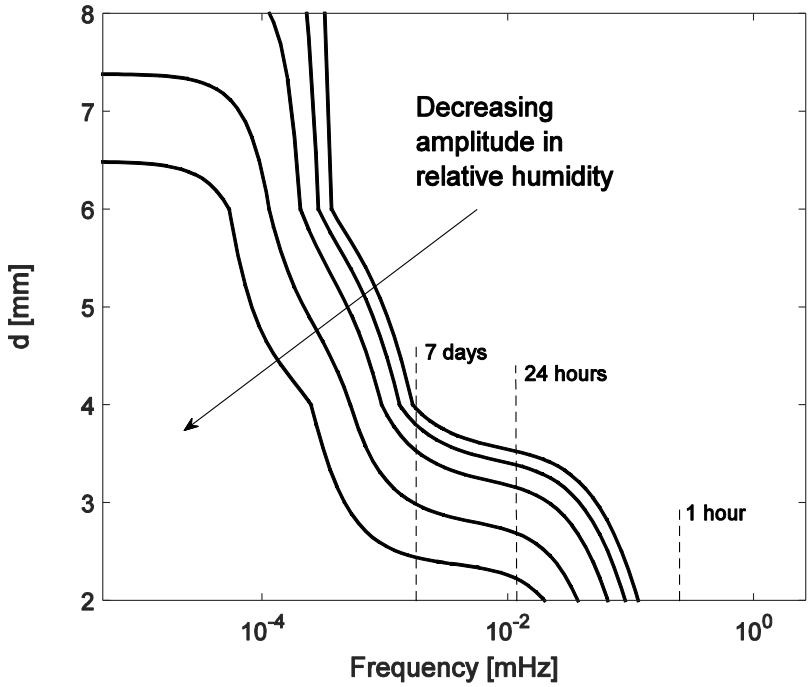

Figure 4.13: *Contour plot of the allowable fluctuations in relative humidity in boards with different thicknesses. The lines indicate the frequency for a given thickness at which the strength of the material is exceeded. Right of this line, the stresses remain below the strength. The lines correspond to different amplitudes (15, 20, 30, 40, and 50 %). Frequencies corresponding to periods of 1 hour, 24 hours, and 7 days are highlighted.*

The expansion and deflection shown in Figure 4.12 apply to an unconstrained board. It illustrates the free strain, i.e. the strain when the board is free to expand. Objects exposed to fluctuations in relative humidity are, however, often constrained in some way. An example of such an object is a panel painting, which may be restrained in expansion or bending, or in both. Stresses arising in such conditions are generally larger compared to the unrestrained case. Some fluctuations may even induce stresses as high as the yield stress, at which the material deforms plastically. Ultimately, an exceedance of the strength of the material can occur, resulting in failure. To get an indication of the maximum allowable fluctuations in relative humidity, the results in Figure 4.12 are combined with experimentally determined values for the E-modulus and the strength of the material. To this end, three-point bending tests are performed on small beams prepared from a large oak board, with dimensions of 10 x 10 x 150 mm. A constant strain rate of 0.5 mm/min is applied until sample failure. In total 8 experiments are performed with different beams, all with their axes along the radial direction. The average E-modulus of the beams is 1.44 GPa, with an average strength of 17.6 MPa. With these values, a maximum strain can be calculated as

$$\varepsilon_{\max} = \frac{\sigma_{\max}}{E}, \tag{4.28}$$

with σ_{max} the material strength and E the Young's modulus, which results in ε_{max} = 0.012. Note that this applies for a material restrained in expansion, where only normal stresses are assumed. The value for ε_{max} is plotted in the contour plot in Figure 4.13 as the solid line for different amplitudes in relative humidity. To the left of this line, the maximum strain is exceeded, i.e. the maximum stress is surpassed, which may cause failure. A decrease in relative humidity amplitude results in a shift of this line towards lower frequencies: the board can sustain the imposed relative humidity up to slower fluctuations.

Although the contour plot in Figure 4.13 provides an insightful image in the allowable fluctuations of relative humidity of an oak board, some comments need to made. First of all, the contour plot should not be interpreted as a robust criterion for the failure of a component. The calculation relies on the free strain calculated at half-thickness, which, when constrained, results in stresses. The resulting free strain is therefore a crude average of the board, which may be exceeded at certain positions. Moreover, the absence of shear stress is assumed; only normal stresses are considered. Steep gradients in moisture content, however, may provoke high values of shear stress. Furthermore, material inhomogeneity or finishing layers can influence moisture transport, and consequently stresses, to a large extent. Finally, the mechanical properties used in the estimation of the maximum allowable strain result from experiments on radial samples, whereas the expansion is calculated in the tangential direction. The ratio between material strength and E-modulus used to calculate the maximum strain is, however, seen to be comparable in both directions (Saft & Kaliske, 2013). The deviations when tangential properties are used, are therefore expected to be minor.

Nevertheless, the simple approach with experimental values for both expansion and mechanical properties yields a clear qualitative image of the allowable frequencies for different thicknesses. The plot illustrates that, for thin boards, small fluctuations in the order of one day can already lead to exceedance of the strength by the stresses associated with restrained expansion. Switching off the heating system in a museum overnight can therefore have major consequences for thin objects.

4.4 CONCLUSIONS

With the analysis proposed in this study, the diffusion coefficient and linear hygroscopic expansion coefficient of wood can be derived from a simple bending experiment. The resulting diffusion coefficients in the range of $2\text{-}9\cdot10^{-11}$ m^2/s and linear hygro-expansion coefficients in the range of 0.2-0.4 are in agreement with values found in literature. The scaling law concerning the maximum deflection of the board during a step change in the relative humidity is seen to describe the experiments well qualitatively, but overestimates the maximum deflection quantitatively. Local inhomogeneities can attenuate the asymmetry in moisture content over time, leading to smaller deflections. Furthermore it is assumed that the moisture transport is uninfluenced by stresses in the material. It is, however, expected that stresses affect the movement of moisture due to their impact on the chemical potential of water and thus the moisture absorption capacity of the matrix (Derrien & Gilormini, 2007). Since a gradient in chemical potential is the driving force for moisture transport, stresses

arising from swelling and shrinkage can have an influence on the moisture distribution over time (Sar, et al., 2012). The incorporation of the interrelation between the stress field and moisture transport in the theory is not straightforward. A more thorough analysis is needed to include these aspects. Nevertheless, the qualitative behavior as predicted from theory is seen to be adopted by experiments. Experiments with different thicknesses of the board result in the same characteristic shape for the deflection, where the similarity is striking in the starting period. After the maximum deflection is reached, the relaxation of the boards is seen to follow different paths, in a more or less random fashion, i.e. not dependent on thickness. This may be attributed to the inhomogeneous nature of wood.

Frequency response behavior of the wood board can be derived from its step response provided that the board can be approximated as a linear system. The behavior is well captured, reflected in the shape of the predicted Bode plots adopted by experimental results. Moreover, the amplitude in x-deflection can be predicted accurately from the step response. The ability to qualitatively predict the frequency behavior of the board is an encouraging result. It allows the prediction of mechanical behavior of an element for fluctuating climatic conditions by measuring its step response, which is a relatively short experiment. It should be noted though, that under slowly fluctuating conditions, other effects may start to play a role, e.g., creep.

A promising extension of the experimental part of the study should be sought in the simultaneous measurement of the deflection and the local moisture content. The deflection can be assessed optically, as shown in this study, whereas the moisture could be measured non-destructively by NMR. In this way the moisture content profile can be related directly to the hygromorphic response at any time. This combination provides more information about the moisture transport during the bending experiment, and possibly elucidates the interrelation of stress distribution and moisture transport. Also the influence of the number of cycles in relative humidity on the bending behavior can be evaluated, as well as the impact of different paints or coatings on the surface of the board.

5 CONCLUSIONS AND OUTLOOK

The treatment of the sorption behavior of a cubic oak block in Chapter 2 is seen to provide the sorption curve by fitting its moisture content during sinusoidal fluctuations in relative humidity. Comparison of an average sorption curve determined from an equilibrium measurement shows good agreement. Discrepancies are caused by the condition imposed on the derived sorption curve that it should pass through the initial condition of the sample.

The frequency behavior of moisture content and expansion of cubic oak blocks is scalable by introducing a dimensionless frequency, as shown in Chapter 3. This dimensionless frequency is dependent on the size of the sample and the diffusion coefficient. After scaling, three regimes can be distinguished: constant amplitude at low dimensionless frequencies, where the sample is always in equilibrium; an inflection in amplitude when the time scale of the fluctuations is of the order of the diffusion time scale; a constant decline in amplitude at high dimensionless frequencies where the fluctuations are faster than transport. Numerical simulations affirm the scaling derived from the simple approach.

The more thorough assessment of moisture transport by means of Nuclear Magnetic Resonance (NMR) provides insight in the influence of the transport direction during cyclic relative humidity fluctuations. The longitudinal direction is found to be dominant over the radial and tangential direction. Furthermore, the T_2 distribution over time provides additional information about the moisture present in the system. During the sinusoidal fluctuations, not only the average value, but also the bounds of the T_2 distribution shift sinusoidally. This might be attributed to the change in surface-to-volume ratio associated with a change in moisture content. Additional sinusoidal experiments with materials exhibiting no expansion in the hygroscopic range can provide more insight on this aspect. Concurrent measurement of expansion, moisture content, and T_2 reveals that all three quantities are coupled during sinusoidal fluctuations.

A transient bending experiment on oak boards is introduced in Chapter 4. A simple model, based on the description of moisture transport by the diffusion equation, and assuming an isotropic, elastic mechanical model, provides the diffusion coefficient and expansion coefficient. Furthermore, the deflective response of the board to a step change in relative humidity contains information about its frequency response. Experiments with a sinusoidally varying relative humidity show good agreement with the prediction based on the step response.

Diffusion coefficients are derived from two different experiments in this study. The frequency behavior of the moisture content and expansion of small blocks can be fitted to determine the diffusion coefficient. Since this diffusion coefficient results from all-sided exposure to the ambient air, it contains the contributions of the three orthotropic directions. Since NMR experiments showed the major contribution of the longitudinal direction, this diffusion coefficient is higher than the radial diffusion coefficient derived from the transient bending of a board. Nevertheless, values agree in the order of magnitude ($\sim 10^{-10}$ m^2/s).

The overall conclusion of the study described in this thesis is that the moisture sorption and resulting expansion of oak wood can be well described by treating the material as

a first-order linear system. Sorption experiments on oak with a sinusoidally fluctuating relative humidity, in combination with a model based on the approximation of its sorption behavior as the response of a linear system are shown to provide the non-linear sorption curve. Good agreement is found with an average sorption curve determined with the conventional, equilibrium method. Furthermore, the sorption and expansion frequency behavior of small oak blocks is shown to be scalable with a dimensionless frequency, arising from the approximation as a linear system. Three-dimensional simulations of the experiment affirm the scaling with the dimensionless frequency. Moreover, the step response of an oak board to a change in relative humidity at one of its surfaces in terms of the deflection contains information about its frequency behavior. Laplace transforming the fitted step response provides an accurate prediction of the deflection in a wide range of frequencies, which is verified by performing experiments with sinusoidal relative humidity fluctuations. All these results allow us to conclude that the hygromorphic behavior of oak can be approximated as the response of a linear system, at least as a first order approximation.

Several possibilities exist for extension and continuation of the study presented here. The first-order linear behavior used to describe the sorption and expansion behavior in wood can be explored in other materials. The method presented to determine an average sorption curve from the response of a sample to a sinusoidal relative humidity fluctuation is promising, however, experiments need to be performed with other materials to determine whether the sorption behavior is universal for hygroscopic materials. To this end, experiments with highly hygroscopic materials (e.g., other wood species or gypsum), and materials with minor hygroscopic moisture sorption (e.g., brick or concrete) should be conducted. Furthermore, the study on the frequency behavior of moisture sorption and expansion of small cubic blocks can be deepened by considering other relative humidity ranges and amplitudes. The results presented were performed with a relative humidity fluctuation of 50 ± 40 %. If the material responds to imposed changes almost linearly, as seen in the experiments, it is expected that halving the amplitude in relative humidity results in half the amplitude in moisture content and expansion. The non-linearity of the sorption curve can, however, account for non-linear effects, especially at high relative humidity (above 90 %).

The simple approach in the bending experiments is seen to lead to an overestimation of the deflection. Mechanical properties influenced by the moisture content cannot account for this deviation. It is therefore expected that the description of moisture transport with the diffusion equation is an oversimplification. To acquire more information about the moisture transport during the experiment, the bending experiment presented in Chapter 4 could be performed in combination with NMR. When placing the clamped end of the board inside the coil and changing the applied gradient, profiles along the thickness of the board can be measured. Simultaneously, the bending of the board can be assessed optically, as presented in this thesis. This concurrent evaluation can provide further information regarding the interrelation between moisture transport and resulting macroscopic deformation. Additionally the impact of different paint or coating layers on the (obstruction of) moisture transport in the board, and consequently on the deformation, can be determined.

Since the moisture-induced expansion is associated with stresses in the material, it is expected that cracks are formed eventually. The occurrence is expected sooner when the board is restricted in expansion in some way, when stresses are generally larger. An appealing

extension is therefore the incorporation of Acoustic Emission (AE) in the experiments. AE has been applied before for failure analysis in wood (Lamy, et al., 2013), relying on the detection of transient elastic waves generated during rapid release of strain energy during cracking. The deformation can then be measured as shown in this study, while the failure of the material is assessed by AE.

APPENDIX A: HUMIDIFIER

To generate an air flow with a certain relative humidity, a system called a humidifier is used. The working principle of the humidifier consists of intermixing a dry air stream and a humid air stream. A schematic diagram of the humidifier is shown in Figure 2.6. Compressed air is first dried by a membrane dryer. A chamber of silica gel beads is connected to the air stream after the membrane dryer using the color of the beads to verify that the air stream is dry. The dehumidified stream is then divided over two Bronkhorst flow controllers. By applying a certain voltage, the flow through the flow controller can be set precisely. This voltage is applied using a LabJack U12 digital-to-analog converter (DAC), which is controlled through Matlab on a desktop. After leaving the flow controllers, both separated air streams are still dehumidified. One of the air streams is conducted through tubing with semi-permeable sides, embedded in a temperature controlled bath, to moisten the air. After leaving the bath, the air stream is conducted through a condenser to remove excess moisture. A check valve is added to the end of both the wet and dry circuit to ensure flow only in one direction. Both streams are reunited again using a y-coupling, after which the streams mix to produce a uniform flow with a relative humidity determined by their mixing proportions. The relative humidity of the outflowing air is set by

$$RH = \frac{V_{wet}}{V_{wet} + V_{dry}}, \tag{A.1}$$

where V_{wet} and V_{dry} are the wet and dry flow respectively, which are set through the flow controllers. The sum of these two air flows is kept constant during a dynamic experiment.

Two different types of humidifiers are used in the experiments. One is exactly as described above, the other one is equipped with two magnetic valves instead of two flow controllers. This complicates the control of relative humidity slightly since the valves can be either open or closed. To arrive at the desired relative humidity value, a method is used in which one of the valves is open continuously and the other valve is opened and closed on a pulsed interval. During the pulse window τ the valve is alternately open and closed during a time t_o and t_c respectively, such that $\tau = t_o + t_c$. The times t_o and t_c depend on the desired relative humidity. If a relative humidity below 50 % is desired, the dry stream is open continuously and the wet stream is pulsed, where the times during which the valves are open and closed are given by

$$t_{w,o} = \tau \frac{RH}{1-RH}, \quad t_{w,c} = \tau \frac{1-2RH}{1-RH}, \quad t_{d,o} = \tau, \quad t_{d,c} = 0. \tag{A.2}$$

In the above expressions the subscripts *w* and *d* refer to the wet and dry streams respectively, and the subscripts *o* and *c* denote open and closed respectively. If a relative humidity above 50 % is desired, the wet stream is open continuously and the dry stream is pulsed, which results in expressions for the open and closed times as

$$t_{w,o} = \tau, \quad t_{w,c} = 0, \quad t_{d,o} = \tau \frac{1 - RH}{RH}, \quad t_{d,c} = \tau \frac{2RH - 1}{RH}. \tag{A.3}$$

The pulse window τ should be chosen such that the two air streams can mix properly during this time interval. If τ is chosen too short, the execution time of the command in Matlab starts to play a role. If τ is chosen too long, the relative humidity of the outflowing air has a more discrete course over time, since the mixing time of the two air streams is shorter than the pulse window. A pulse window of 2 s yields a continuous course of the output relative humidity, as verified by a relative humidity-sensor.

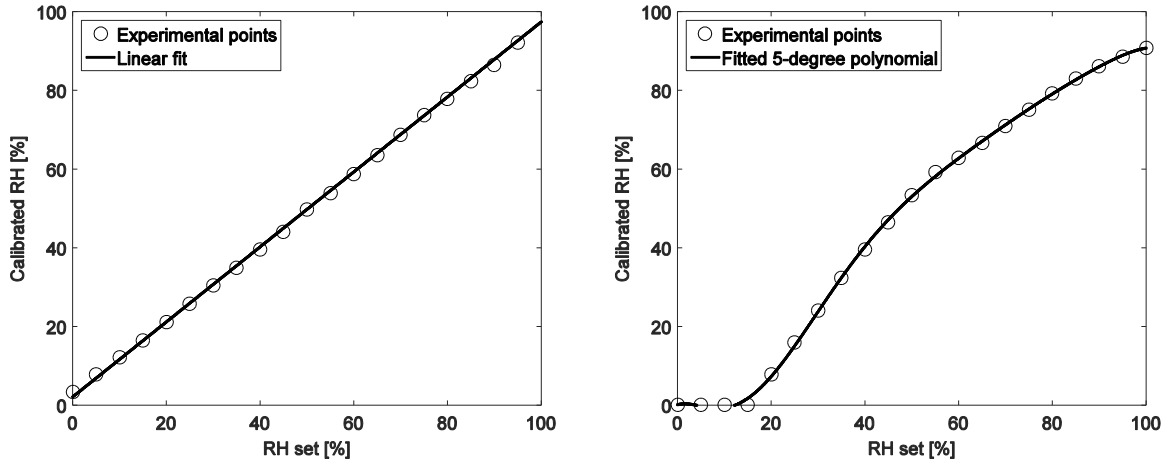

Figure A.1: *Relative humidity calibration curves for the two humidifying set-ups used in the present study.*

The relative humidity of the air leaving the humidifier is calibrated using a Sensirion relative humidity-sensor which has been calibrated by a mirror dew-point meter. The calibration is performed as follows: an air stream is generated and conducted through a tube containing the relative humidity-sensor. The relative humidity of the air is varied from 0 to 100 % in steps of 5 %, during which the relative humidity is measured by the sensor. Because the sensor has a certain equilibration time, stabilization of the sensor is awaited before continuation to the next relative humidity value. In Figure A.1 the calibrated relative humidity, which follows from the sensor, is plotted against the relative humidity from mixing proportions for both set-ups. The calibration curve of the set-up in which two flow controllers are used to set the mixing proportions of the wet and dry air streams is seen to be linear. The calibration curve of the set-up with magnetic valves is non-linear.

APPENDIX B: CALIBRATION NMR SIGNAL

The NMR signal is calibrated using samples which have been equilibrated in desiccators over saturated salt solutions for three months. An additional sample is used which is vacuum-saturated with water. The samples are first weighed to determine their equilibrium weight and then placed in the sample holder depicted in Figure 3.3. The NMR signal is captured with the settings also used in subsequent experiments, described in Section 3.2.4. A Hahn spin-echo is performed at several frequencies, covering the total size of the sample. An average signal is then calculated to account for local inhomogeneities in the wood. Afterwards, the samples are oven-dried at 105 °C. The moisture content of the sample is determined from the mass of the sample *w* as

$$c_{eq} = \frac{w_{eq} - w_0}{w_0}, \tag{B.1}$$

where w_0 is the oven-dried mass of the sample. A linear relation between the moisture content of the sample and the NMR signal is observed, as shown in Figure B.1. It is seen that at a moisture content of ~0.05, the captured signal is approximately equal to the background noise. A moisture content below this point can thus not be distinguished from the noise and provides us with a lower bound. A similar signal calibration was also found by van Meel et al. (2011).

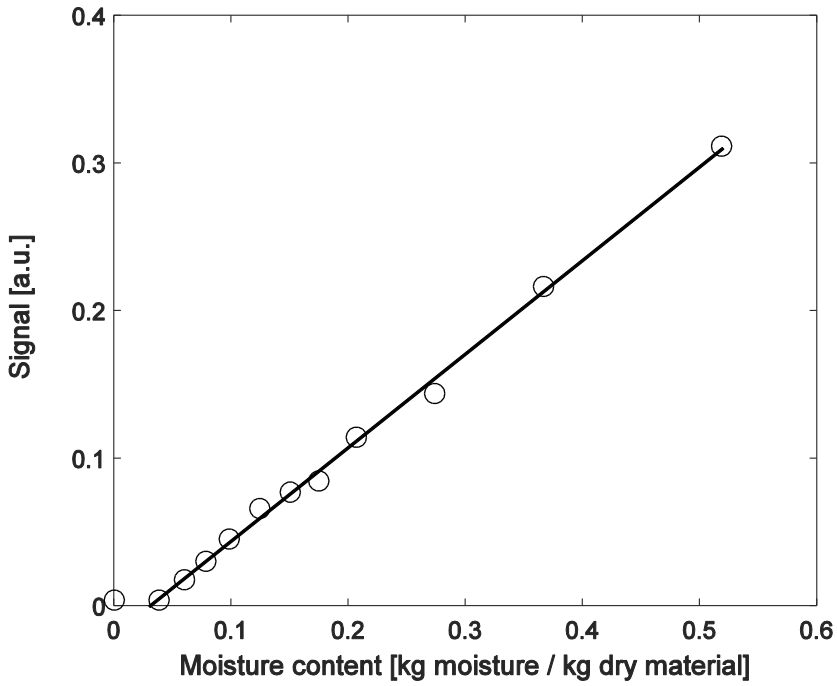

Figure B.1: *Average Hahn spin-echo signal of equilibrated samples as a function of their moisture content.*

APPENDIX C: CALIBRATION OPTICAL FIBER SENSOR

The Philtec© optical fiber displacement sensor is calibrated using three Mitutoyo calibration blocks, with thicknesses of 1, 1.7, and 2 mm. The calibration procedure is as follows: the optical fiber displacement sensor is fixed above a plane surface. First one calibration block is placed on the surface. The distance between the optical sensor and this first calibration block is the reference length. By changing the blocks, or using combinations of several blocks, different distances between the sensor and the blocks can be created. The relation between the distance imposed by the combination of the calibration blocks and the distance detected by the sensor is shown in Figure C.1, and seen to be perfectly linear.

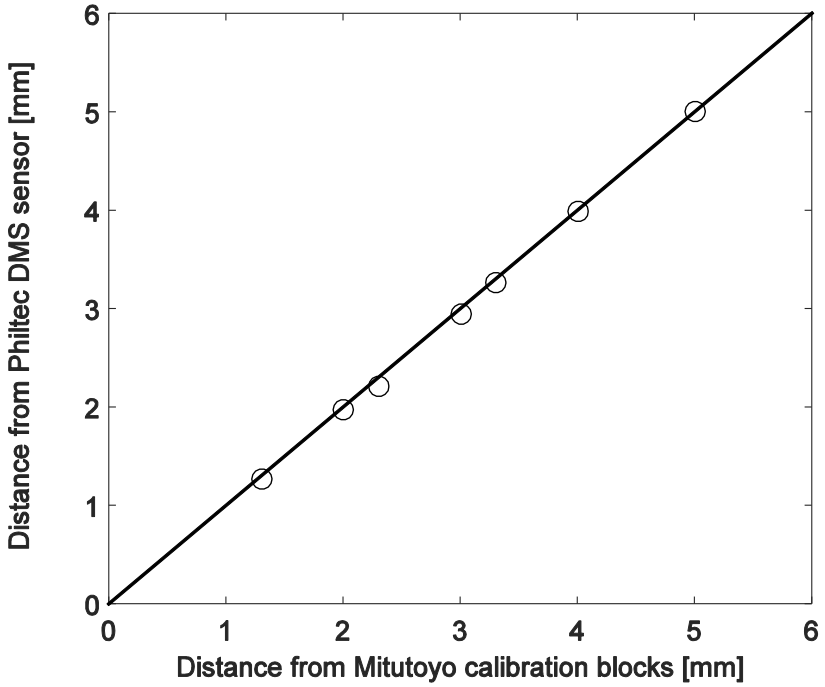

Figure C.1: *The distance detected by the sensor as a function of the distance which follows from different combinations of calibration blocks.*

APPENDIX D: DERIVATION OF HYGRO-BENDING THEORY

In this appendix we give a more detailed explanation of the linear elastic model to describe the bending of a board with an inhomogeneous moisture distribution. A cross-section of the board with thickness *d* is schematically represented by a system consisting of *n* equally spaced springs, and an infinitely stiff beam connecting the springs on their upper ends, as is shown schematically in Figure D.1.

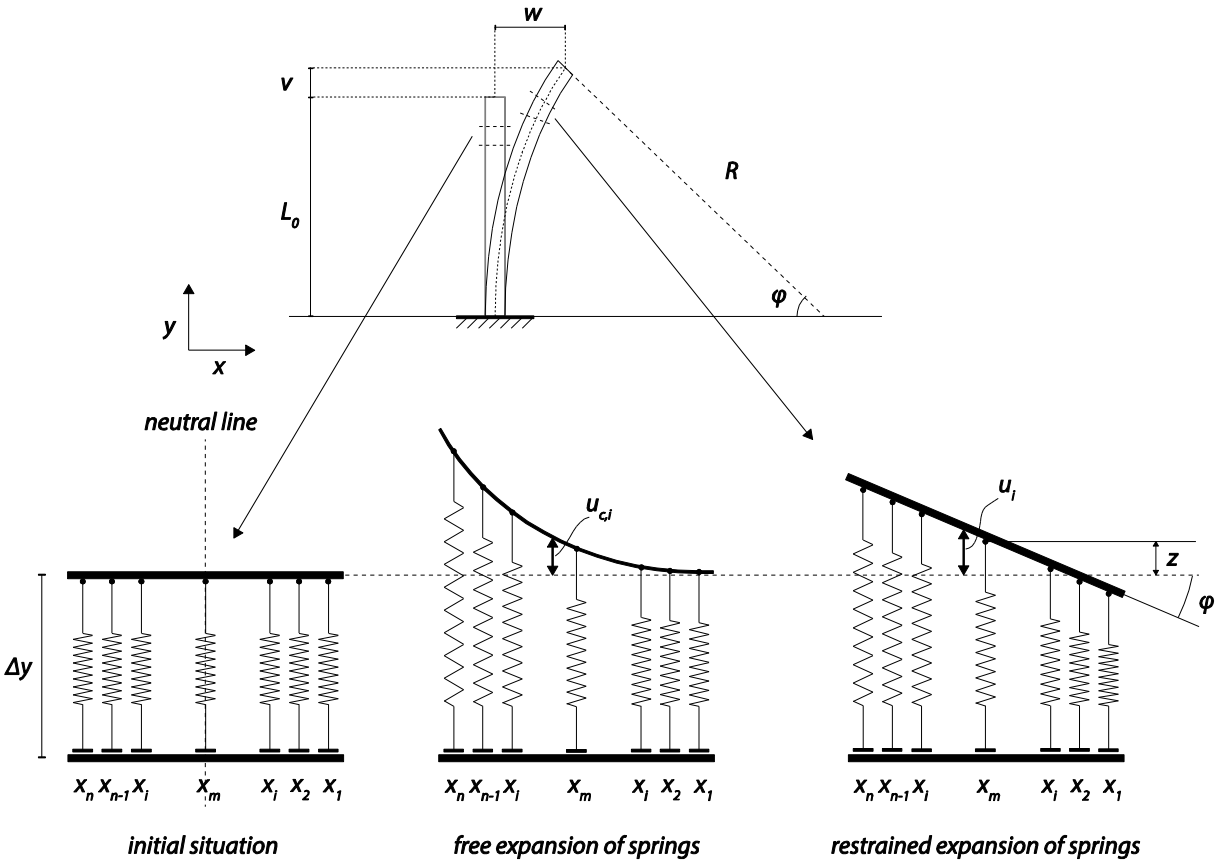

Figure D.1: *A schematic representation of the cross-section of the wood board, consisting of n springs and an infinitely stiff beam connecting the springs on their upper ends. In equilibrium (left), the moisture content profile is flat, consequently all springs have equal lengths and equal forces; the beam is thus flat as well. For a non-uniform moisture content profile (middle), the springs will have different lengths when not restrained by the infinitely stiff beam. The springs are, however, connected to each other by the beam, which cannot deform, only rotate and translate. The indention of each spring is consequently influenced by all other springs, which results in the configuration on the right.*

Initially, the board has a flat moisture content profile and all springs are equally long. A change in moisture content results in expansion or shrinkage; in our model, this is reflected in a change in the length of the spring. If all springs are free to expand, the result is a situation as shown in the middle of Figure D.1. The springs, however, are connected to each other on their ends by an infinitely stiff beam. This beam cannot deform, only translate in the y-direction

and rotate. As a consequence, a spring may have a different elongation than its free length change. The force in a spring is proportional to the difference between the free and restrained length change of the spring. Since only the static configuration of the system is considered, the sum of all forces acting on the beam should be zero. Furthermore, the sum of moments exerted on the beam by the individual springs should be zero.

In this approach several assumptions are made. First of all, the moisture profile is known at all moments in time and is not influenced by the deformation of the board. Secondly, it is assumed that the material is linearly elastic. The model beam is infinitely stiff, therefore it can rotate and translate, but cannot deform. This corresponds to the assumption that the section plane does not deform, which is also one of the assumptions in simple bending theory. Another assumption is the subjection to pure bending, i.e. the absence of shear stresses. Furthermore, the neutral line of the board is assumed to run along its length, at the middle of the board, as indicated by the dotted line in Figure D.1. This is justified if the impermeable layer at one surface of the board does not contribute to the system mechanically. Finally lateral contraction is neglected, i.e. the board expands or shrinks only along its length, not along its thickness.

The configuration of the system starts with the known moisture content profile as a function of the one-dimensional space variable x and time t, i.e. $c = c(x,t)$. In the discretized grid, the moisture content c_i at point i with position x_i is given by

$$c_i = c\left(x_i, t\right). \tag{D.1}$$

The unconstrained expansion $u_{c,i}$ at point i, purely due to the presence of moisture, is proportional to the difference between initial moisture content and moisture content at time t, and can be expressed as

$$u_{c,i} = \alpha\left(c_i - c_{s,i}\right)\Delta y, \tag{D.2}$$

where α is the linear hygroscopic expansion coefficient, $c_{s,i}$ the initial moisture content at point i, and Δy the height of the section, as shown in Figure D.1. The actual expansion u_i at the top of spring i can be written in terms of the unknown variables z and θ as

$$u_i = z + \theta\left(x_i - x_m\right), \tag{D.3}$$

with z the expansion at the neutral line, $\theta = \tan\varphi$, x_m the position of the neutral line, and x_i the position of point i. Note that $x_m = d/2$. The force exerted on the spring is proportional to the indention of the spring:

$$F_i = k\left(u_{c,i} - u_i\right) = k\left(u_{c,i} - z - \theta\left(x_i - x_m\right)\right), \tag{D.4}$$

where k is the spring constant, analogous to Young's modulus of elasticity. The system needs two conditions to solve for the unknown variables z and θ. These two conditions are the balance of forces and the balance of moments over the neutral point x_m:

$$\sum_{i=1}^{n} F_i = 0,$$
$$\sum_{i=1}^{n} F_i \left(x_i - x_m \right) = 0. \tag{D.5}$$

The force balance is used to derive an expression for the displacement of the beam at its neutral point

$$z = \frac{1}{n} \sum_{i=1}^{n} u_{c,i} = \alpha \frac{\Delta y}{n} \sum_{i=1}^{n} \left(c_i - c_{s,i} \right), \tag{D.6}$$

where use has been made of the fact that

$$\sum_{i=1}^{n} \left(x_i - x_m \right) = 0. \tag{D.7}$$

The second condition states that the sum of moments is zero, which leads to the expression for the angle of the beam

$$\theta = \frac{\sum_{i=1}^{n} u_{c,i} \left(x_i - x_m \right)}{\sum_{i=1}^{n} \left(x_i - x_m \right)^2} = \alpha \frac{\sum_{i=1}^{n} \left(c_i - c_{s,i} \right) \left(x_i - x_m \right)}{\sum_{i=1}^{n} \left(x_i - x_m \right)^2} \Delta y. \tag{D.8}$$

In case of a flat initial moisture profile, Eq. (D.8) may be simplified using Eq. (D.7) to give

$$\theta = \alpha \frac{\sum_{i=1}^{n} c_i \left(x_i - x_m \right)}{\sum_{i=1}^{n} \left(x_i - x_m \right)^2} \Delta y. \tag{D.9}$$

Note that Eqs. (D.6) and (D.9) can be rewritten as

$$z = \frac{\alpha}{d} \frac{d}{n} \Delta y \sum_{i=1}^{n} \left(c_i - c_{s,i} \right), \tag{D.10}$$

$$\theta = \alpha \Delta y \frac{\frac{d}{n} \sum_{i=1}^{n} \left(c_i - c_{s,i} \right) \left(x_i - x_m \right)}{\frac{d}{n} \sum_{i=1}^{n} \left(x_i - x_m \right)^2}, \tag{D.11}$$

where d/n is the spacing between two springs Δx. For an infinite number of springs, the expressions (D.6) and (D.9) can be expressed as the integrals

$$\lim_{n\to\infty} z = \frac{\alpha}{d} L \int_0^d \left(c - c_s\right) dx, \tag{D.12}$$

$$\lim_{n\to\infty} \theta = \alpha L \frac{\int_0^d \left(c - c_s\right)\left(x - x_m\right) dx}{\int_0^d \left(x - x_m\right)^2 dx}. \tag{D.13}$$

The integrals in Eqs. (D.12) and (D.13) may be simplified by assuming the moisture content independent of the y-position, to arrive at

$$z = \frac{\alpha L}{d} \int_0^d \left(c - c_s\right) dx, \tag{D.14}$$

$$\theta = 12 \frac{\alpha L}{d^3} \int_0^d \left(c - c_s\right)\left(x - x_m\right) dx, \tag{D.15}$$

where the integral in the denominator in Eq. (D.13) is calculated as

$$\int_0^d \left(x - x_m\right)^2 dx = \frac{d^3}{12}. \tag{D.16}$$

With the expressions for the z and θ known, the deflection of the board at half-thickness can be derived. Figure D.1 shows the bent board with relevant parameters. First of all, the length of the board L at any time $t > 0$ can be expressed as

$$L\left(t\right) = L_0 + z\left(t\right), \tag{D.17}$$

where L_0 is the length of the board at time $t = 0$. With Eq. (D.14) we can rewrite Eq. (D.17) as

$$L\left(t\right) = L_0 \left[1 + \frac{\alpha}{d} \int_0^d \left(c\left(x,t\right) - c_0\right) dx\right]. \tag{D.18}$$

Since the board bends onto a circle, the length of the board, the radius of curvature R, and the angle $\varphi = \tan^{-1} \theta$ are related by

$$\varphi R = L. \tag{D.19}$$

Using this expression, the deflection of the board in the x-direction w and the expansion in the y-direction v can be written as

$$w = R\left(1 - \cos\varphi\right) = \frac{L}{\varphi}\left(1 - \cos\varphi\right), \tag{D.20}$$

$$v = R\sin\varphi - L_0 = \frac{L}{\varphi}\sin\varphi - L_0. \tag{D.21}$$

By taking into account only the first two terms of the Taylor series expansion of Eq. (D.20), and assuming $L_0 \approx L$ and $\varphi \approx \theta$, which holds for small deflections, a compact expression for the deflection can be derived as*:*

$$w(t) = 6\frac{\alpha L_0^{\,2}}{d^3}\int_0^d c(x,t)\left(x - \frac{d}{2}\right)dx. \tag{D.22}$$

APPENDIX E: IMAGE ANALYSIS

The deflection of the wood board is measured by detecting the copper pointer attached to the head of the board. Since the contrast between the copper pointer and its background is large, a Matlab code is written which automatically detects the position of the tip of the pointer. The procedure is schematically shown in Figure E.1. It consists of an initial manual calibration using the background graph paper, by selecting two points and entering the distance between these two points. This calibration also determines the angle of the graph paper with a random horizontal line. Then, a loop starts to analyze all images from one experiment. The contrast of each image is first adjusted, after which edges in the image are detected based on a specified threshold level. The resulting binary image is then dilated and a flood-fill operation is performed on the dilated image. Structures connected to the image border are subsequently deleted and the image is eroded to arrive at the final binary image from which the position of the tip of the pointer is determined. In the final binary image, several remaining groups may exist. The group closest to the position of the tip of the pointer from the previous iteration in the loop is selected as the group belonging to the pointer. The position of the tip of the pointer is then determined as the point of this group with the highest y-position after rotation with the angle from the initial calibration.

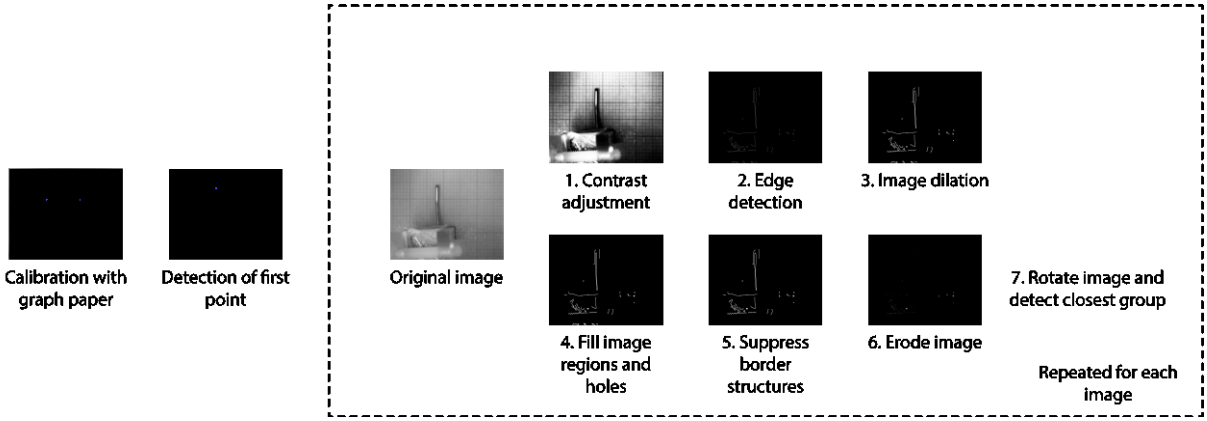

Figure E.1: *Schematic representation of the image analysis procedure performed in Matlab to determine the position of the tip of the copper pointer attached to the board.*

To verify the accuracy of the automatic detection method, a comparison is made with a procedure in which the position of the tip of the copper pointer is assigned manually for each image. The result for a random experiments is shown in Figure E.2. As can be seen, the deflection of the board from automatic detection overlaps the deflection from manual detection. It can therefore be concluded that the Matlab code is suited to detect the deflection of the board up to an accuracy as would result from manual detection.

The analysis of the images by automatic tracking of the tip of the copper pointer yields the deflection of the board over time, in the x- and the y-direction. However, this deflection is not the true deflection of the board itself, but the deflection measured at the tip of the copper pointer. The pointer and the Perspex strip over the end of the board act as inactive, elongating

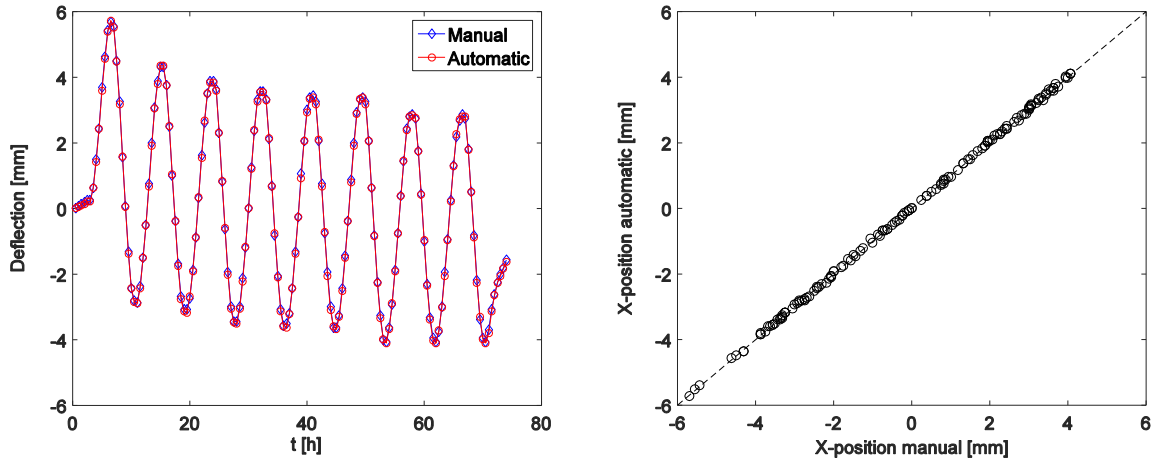

Figure E.2: *The manual and automatic x-position of the copper pointer during an arbitrary experiment (left), and the relation between manual and automatic x-position detection of the copper pointer during the same experiment.*

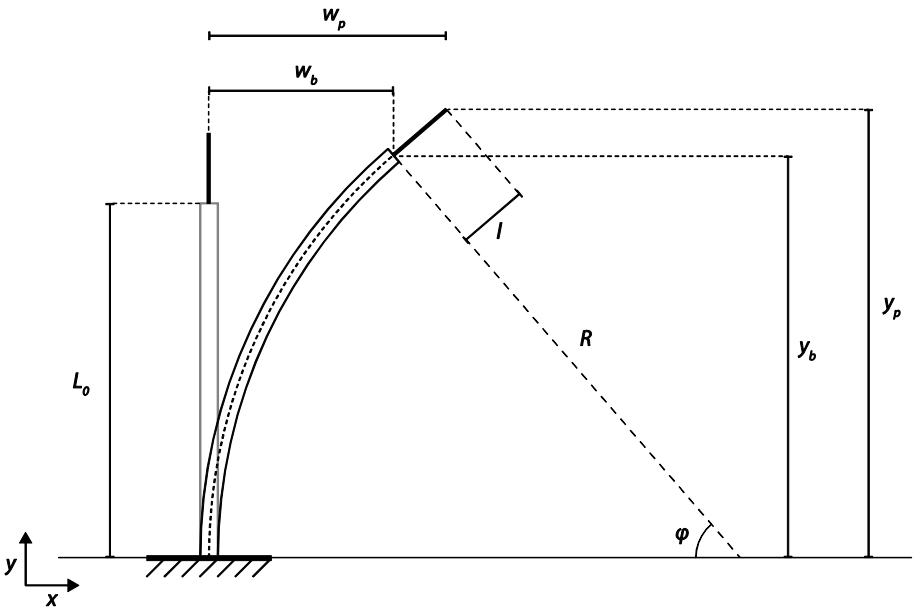

Figure E.3: *The geometry of the hygro-bending system, i.e. board and inactive pointer, with parameters for analysis.*

parts. To obtain the maximum deflection of the board at its half thickness, a correction procedure is applied. Consider the geometry of the hygro-bending system as shown schematically in Figure E.3, with a board of length L, to which a pointer is attached with a length l. In the introduced coordinate system, the x-position of the tip of the pointer and of the end of the board are equal to their respective deflections w_p and w_b. The relation between both deflections is

$$w_p = w_b + l\sin\varphi = \frac{L}{\varphi}\left(1-\cos\varphi\right) + l\sin\varphi, \tag{E.1}$$

where use has been made of Eq. (D.20). Using Eq. (D.21), the y-position of the pointer y_p and of the end of the board y_b can be related by the expression

$$y_p = y_b + l\cos\varphi = \frac{L}{\varphi}\sin\varphi + l\cos\varphi. \tag{E.2}$$

Rewriting Eq. (E.2) and using the relation between the y-deflection of the board v_p and its y-position $y_p = v_p + L_0 + l$, an expression for the length of the board is found as

$$L = \frac{\varphi}{\sin\varphi}\left(v_p + L_0 + l\left(1-\cos\varphi\right)\right). \tag{E.3}$$

Eq. (E.3) can be inserted into Eq. (E.1) to yield the non-linear equation

$$\frac{1-\cos\varphi}{\sin\varphi}\left(v_p + L_0 + l\left(1-\cos\varphi\right)\right) - w_p + l\sin\varphi = 0, \tag{E.4}$$

which can be solved using a non-linear solver to acquire φ. With the angle φ known, the length of the board can be acquired with Eq. (E.3). The deflection of the end of the board at half-thickness can then be obtained with Eqs. (D.20) and (D.21). This procedure is repeated for all measurement points.

REFERENCES

Alesiani, M., Proietti, F., Capuani, S., Paci, M., Fioravanti, M. & Maraviglia, B., 2005. ^{13}C CPMAS NMR spectroscopic analysis applied to wood characterization. *Applied magnetic resonance,* Volume 29, pp. 177-184.

Allegretti, O. & Ferrari, S., 2007. Characterization of the drying behaviour of some temperate and tropical hardwoods. *Proceedings of the 1st International Scientific Conference on Hardwood Processing, Quebec,* pp. 285-290.

Allegretti, O., Rémond, R. & Perré, P., 2003. A new experimental device for non-symmetrical drying tests - experimental and numerical results for free and constrained samples. *Proceedings 8th International IUFRO Wood Drying Conference, Brasov,* pp. 65-70.

Almeida, G., Gagné, S. & Hernández, R. E., 2007. A NMR study of water distribution in hardwoods at several equilibrium moisture contents. *Wood Science and Technology,* Volume 41, pp. 293-307.

Avramidis, S., Englezos, P. & Papathanasiou, T., 1992. Dynamic nonisothermal transport in hygroscopic porous media: moisture diffusion in wood. *AIChE Journal,* Volume 38, pp. 1279-1287.

Babbitt, J. D., 1942. On the adsorption of water vapour by cellulose. *The Canadian Journal of Research A,* Volume 20, pp. 143-172.

Balcom, B., 2016. *Personal correspondance.* University of New Brunswick.

Blumer, S., Serrano, E., Gustafsson, P. J. & Niemz, P., 2011. Moisture induced stresses and deformations in parquet floors. In: V. Bucur, ed. *Delamination in wood, wood products and wood-based composites.* Dordrecht: Springer, pp. 365-378.

Bouquet, R., Chirife, J. & Iglesias, H. A., 1980. Technical note: On the equivalence of isotherm equations. *Journal of Food Technology,* Volume 15, pp. 345-349.

Brandao, A. & Perré, P., 1996. The "flying wood" - a quick test to characterise the drying behavior of tropical wood. *Fifth International IUFRO Wood Drying Conference.* Quebec, Canada.

Bratasz, L., Kozlowski, R., Kozlowska, A. & Rachwal, B., 2008. Sorption of moisture and dimensional change of wood species used in historic objects. In: *Proceedings of the International Conference held by COST Action IE0601 Wood Science for Conservation of Cultural Heritage.* Braga, Portugal.

Brownstein, K. R. & Tarr, C. E., 1979. Importance of classical diffusion in NMR studies of water in biological cells. *Physical Review A,* 19(6), pp. 2446-2453.

Brunauer, S., Emmett, P. H. & Teller, E., 1938. Adsorption of gases in multimolecular layers. *Journal of the American Chemical Society,* Volume 60, pp. 309-319.

Caré, S., Bornert, M., Bertrand, F. & Lenoir, N., 2012. Local moisture content and swelling strain in wood investigated by NMR and X-ray microtomography. *15th International Conference on Experimental Mechanics.* Porto, Portugal.

Casieri, C., Senni, L., Romagnoli, M., Santamaria, U. & De Luca, F., 2004. Determination of moisture fraction in wood by mobile NMR device. *Journal of Magnetic Resonance,* Volume 171, pp. 364-372.

Chomcharm, A. & Skaar, C., 1983. Moisture and transverse dimensional changes during air-drying of small green hardwood wafers. *Wood Science and Technology*, Volume 17, pp. 227-240.

Chomcharn, A. & Skaar, C., 1983. Dynamic sorption and hygroexpansion of wood wafers exposed to sinusoidally varying humidity. *Wood Science and Technology*, Volume 17, pp. 259-277.

Cox, J., McDonald, P. J. & Gardiner, B. A., 2010. A study of water exchange in wood by means of 2D NMR relaxation correlation and exchange. *Holzforschung*, Volume 64, pp. 259-266.

Crank, J., 1975. *The mathematics of diffusion.* 2nd ed. New York, Oxford: University Press.

Cunningham, M. J., 1995. A model to explain "anomalous" moisture sorption in wood under step function driving forces. *Wood and Fiber Science*, Volume 27, pp. 265-277.

Danvind, J. & Ekevad, M., 2006. Local water vapor diffusion coefficient when drying Norway spruce sapwood. *Journal of Wood Science*, Volume 52, pp. 195-201.

Dent, R. W., 1977. A multilayer theory for gas sorption. Part I: Sorption of a single gas. *Textile Research Journal*, Volume 47, pp. 145-152.

Derome, D., Rafsanjani, A., Patera, A., Guyer, R., Carmeliet, J., 2012. Hygromorphic behaviour of cellular material: hysteretic swelling and shrinkage of wood probed by phase contrast X-ray tomography. *Philosophical Magazine*, Volume 92, pp. 1-21.

Derrien, K. & Gilormini, P., 2007. The effect of applied stresses on the equilibrium moisture content in polymers. *Scripta Materialia*, Volume 56, pp. 297-299.

Dionisi Vici, P., Mazzanti, P. & Uzielli, L., 2006. Mechanical response of wooden boards subjected to humidity step variations: climatic chamber measurements and fitted mathematical models. *Journal of Cultural Heritage*, Volume 7, pp. 37-48.

Droin, A., Taverdet, J. L. & Vergnaud, J. M., 1988. Modeling the kinetics of moisture adsorption by wood. *Wood Science and Technology*, Volume 22, pp. 11-20.

Droin-Josserand, A., Taverdet, J. L. & Vergnaud, J. M., 1988. Modelling the absorption and desorption of moisture by wood in an atmosphere of constant and programmed relative humidity. *Wood Science and Technology*, Volume 22, pp. 299-310.

Dvinskikh, S. V., Furó, I., Sandberg, D. & Söderström, O., 2011. Moisture content profiles and uptake kinetics in wood cladding materials evaluated by a portable nuclear magnetic resonance spectrometer. *Wood Material Science & Engineering*, Volume 6, pp. 119-127.

Dvinskikh, S. V., Henriksson, M., Berglund, L. A. & Furó, I., 2011. A multinuclear magnetic resonance imaging (MRI) study of wood with adsorbed water: Estimating bound water concentration and local wood density. *Holzforschung*, Volume 65, pp. 103-107.

Dvinskikh, S. V., Henriksson, M., Mendicino, A.L., Fortino, S., Toratti, T., 2011. NMR imaging study and multi-Fickian numerical simulation of moisture transfer in Norway spruce samples. *Engineering Structures*, Volume 33, pp. 3079-3086.

Eitelberger, J. & Hofstetter, K., 2011. Prediction of transport properties of wood below the fiber saturation point – A multiscale homogenization approach and its experimental validation. Part II: Steady state moisture diffusion coefficient. *Composites Science and Technology*, Volume 71, pp. 145-151.

Eitelberger, J., Hofstetter, K. & Dvinskikh, S. V., 2011. A multi-scale approach for simulation of transient moisture transport processes in wood below the fiber saturation point. *Composites Science and Technology,* Volume 71, p. 1727–1738.

Ekstedt, J., Rosenkilde, A., Hameury, S., Sterley, M., Berglind, H., 2007. Measurement of moisture content profiles in coated and uncoated Scots Pine using Magnetic Resonance Imaging. *COST E 53 Conference – Quality Control for Wood and Wood Products.* Warsaw, Poland.

Elder, T. & Houtman, C., 2013. Time-domain NMR study of the drying of hemicellulose extracted aspen (Populus tremuloides Michx.). *Holzforschung,* Volume 67, pp. 405-411.

Engelund, E. T., Thygesen, L. G., Svensson, S. & Hill, C. A. S., 2013. A critical discussion of the physics of wood-water interactions. *Wood Science and Technology,* Volume 47, pp. 141-161.

Erb, R. M., Sander, J. S., Grisch, R. & Studart, A. R., 2013. Self-shaping composites with programmable bioinspired microstructures. *Nature Communications,* Volume 4, p. 1712.

Eriksson, J., Johansson, H. & Danvind, J., 2006. Numerical determination of diffusion coefficient in wood using data from CT-scanning. *Wood and Fiber Science,* Volume 38, pp. 334-344.

Forest Products Laboratory, 2010. *Wood Handbook - Wood as an Engineering Material.* Madison, WI: United States Department of Agriculture.

Franklin, G. F., Powell, J. D. & Emami-Naeini, A., 1994. *Feedback control of dynamic systems.* 3rd ed. Reading, MA: Addison-Wesley Publishing Company.

Frederiksson, M., Wadsö, L. & Johansson, P., 2013. Small resistive wood moisture sensors: a method for moisture content determination in wood structures. *European Journal of Wood and Wood Products,* Volume 71, pp. 515-524.

Gatewood, B. E., 1957. *Thermal stresses.* New York: McGraw-Hill.

Gauvin, C., Jullien, D., Dupré, J.-C. & Gril, J., 2014. Image correlation to evaluate the influence of hygrothermal loading on wood. *Strain,* Volume 50, pp. 428-435.

Gilani, M. S., Abbasion, S., Lehmann, E., Carmeliet, J., Derome, D., 2014. Neutron imaging of moisture displacement due to steep temperature gradients in hardwood. *Internalional Journal of Thermal Sciences,* Volume 81, pp. 1-12.

Hahn, E. L., 1950. Spin echoes. *Physical Review,* Volume 80, pp. 580-594.

Hameury, S. & Sterley, M., 2006. Magnetic resonance imaging of moisture distribution in Pinus sylvestris L. exposed to daily indoor relative humidity fluctuations. *Wood Material Science and Engineering,* Volume 1, pp. 116-126.

Harrington, M., 1996. University of Canterbury.

Holstov, A., Bridgens, B. & Farmer, G., 2015. Hygromorphic materials for sustainable responsive architecture. *Construction and Building Materials,* Volume 98, pp. 570-582.

Hukka, A., 1999. The effective diffusion coefficient and mass transfer coefficient of Nordic softwoods as calculated from direct drying experiments. *Holzforschung,* Volume 53, pp. 534-540.

Hürlimann, M. D. & Venkataramanan, L., 2002. Quantitative measurement of two-dimensional distribution functions of diffusion and relaxation in grossly inhomogeneous fields. *Journal of Magnetic Resonance,* Volume 157, pp. 31-42.

Johansson, J., Blom, A. & Dvinskikh, S. V., 2013. NMR-measurements for determination of local moisture content of coated wood. *Journal of Coatings Technology and Research,* Volume 10, pp. 601-607.

Johansson, J. & Kifetew, G., 2010. CT-scanning and modelling of the capillary water uptake in aspen, oak and pine. *European Journal of Wood and Wood Products,* Volume 68, pp. 77-85.

Kang, W., Chung, W. Y., Eom, C.-D. & Yeo, H., 2008. Some considerations in heterogeneous nonisothermal transport models for wood: a numerical study. *Journal of Wood Science,* Volume 54, pp. 267-277.

Kang, W., Kang, C.-W., Chung, W. Y., Eom, C.-D., Yeo, H., 2008. The effect of openings on combined bound water and water vapor diffusion in wood. *Journal of Wood Science,* Volume 54, pp. 343-348.

Kang, W., Lee, Y. H., Chung, W. Y. & Xu, H. L., 2009. Parameter estimation of moisture diffusivity in wood by an inverse method. *Journal of Wood Science,* Volume 55, pp. 83-90.

Kleinberg, R. L., 1996. Utility of NMR T_2 distributions, connection with capillary pressure, clay effect, and determination of the surface relaxivity parameter ρ_2. *Magnetic Resonance Imaging,* Volume 14, pp. 761-767.

Krabbenhoft, K. & Damkilde, L., 2004. A model for non-Fickian moisture transfer in wood. *Materials and Structures,* Volume 37, pp. 615-622.

Krähenbühl, A., Kerautret, B., Debled-Rennesson, I., Mothe, F., Longuetaud, F., 2014. Knot segmentation in 3D CT images of wet wood. *Pattern Recognition,* Volume 47, pp. 3852-3869.

Lamy, F., Takarli, M., Dubois, F., Angellier, N., Pop, I.-O., 2013. Acoustic emission technique (AET) for failure analysis in wood materials. *13th International Conference on Fracture.* Beijing, China.

Lanvermann, C., Wittel, F. K. & Niemz, P., 2014. Full-field moisture induced deformation in Norway spruce: intra-ring variation of transverse swelling. *European Journal of Wood and Wood Products,* Volume 72, pp. 43-52.

Larsen, K. E. & Marstein, N., 2000. *Conservation of historic timber structures: an ecological approach.* Oxford: Butterworth-Heinemann.

Le Duigou, A., Castro, M., Bevan, R. & Martin, N., 2016. 3D printing of wood fibre biocomposites: From mechanical to actuation functionality. *Materials and Design,* Volume 96, pp. 106-114.

Lindgren, O., Davis, J., Wells, P. & Shadbolt, P., 1992. Non-destructive wood density distribution measurements using computed tomography. *Holz als Roh- und Werkstoff,* Volume 50, pp. 295-299.

Ma, E., Zhao, G. & Cao, J., 2005. Hygroexpansion of wood during moisture adsorption and desorption processes. *Forestry Studies in China,* Volume 7, pp. 43-46.

Maunu, S. L., 2002. NMR studies of wood and wood products. *Progress in Nuclear Magnetic Resonance Spectroscopy,* Volume 40, pp. 151-174.

Meiboom, S. & Gill, D., 1958. Modified spin-echo method for measuring nuclear relaxation times. *The Review of Scientific Instruments,* Volume 29, pp. 688-691.

Menon, R. S., Mackay, A. L., Hailey, J. R. T., Bloom, M., Burgess, A. E., Swanson, J. S., 1987. An NMR determination of the physiological water distribution in wood during drying. *Journal of Applied Polymer Science,* Volume 33, pp. 1141-1155.

Merakeb, S., Dubois, F. & Petit, C., 2009. Modeling of the sorption hysteresis for wood. *Wood Science and Technology,* Volume 43, pp. 575-589.

Merela, M., Oven, P., Serša, I. & Mikac, U., 2009. A single point NMR method for an instantaneous determination of the moisture content of wood. *Holzforschung,* Volume 63, pp. 348-351.

Mitchell, J., Webber, J. B. W. & Strange, J. H., 2008. Nuclear magnetic resonance cryoporometry. *Physics Reports,* Volume 461, pp. 1-36.

Murata, K. & Masuda, M., 2006. Microscopic observation of transverse swelling of latewood tracheid: effect of macroscopic/mesoscopic structure. *Journal of Wood Science,* Volume 52, pp. 283-289.

Nelson, R. M., 1986. Diffusion of bound water in wood. Part 2: A model for isothermal diffusion. *Wood Science and Technology,* Volume 20, pp. 235-251.

Noack, D., Schwab, E. & Bartz, A., 1973. Characteristics for a judgement of the sorption and swelling behavior of wood. *Wood Science and Technology,* Volume 7, pp. 218-236.

Norberg, P., 1999. Monitoring wood moisture content using the WETCORR method. *Holz als Roh- und Werkstoff,* Volume 57, pp. 448-453.

Patera, A., Derluyn, H., Derome, D. & Carmeliet, J., 2015. Influence of sorption hysteresis on moisture transport in wood. *Wood Science and Technology.*

Pel, L., 1995. *Moisture transport in porous building materials, PhD Thesis.* Eindhoven University of Technology.

Pel, L., Landman, K. A. & Kaasschieter, E. F., 2002. Analytic solution for the non-linear drying problem. *International Journal of Heat and Mass Transfer,* Volume 45, pp. 3173-3180.

Pereria da Silva, W., de Silva, C. M. D. P. S., Rodrigues, A. F. & de Figueirêdo, R. M. F., 2015. One-dimensional numerical solution of the diffusion equation to describe wood drying: comparison with two- and threedimensional solutions. *Journal of Wood Science,* Volume 61, pp. 364-371.

Pourmand, P., Wang, L. & Dvinskikh, S. V., 2011. Assessment of moisture protective properties of wood coatings by a portable NMR sensor. *Journal of Coatings Technology and Research,* Volume 8, p. 649-654.

Rafsanjani, A., Derome, D., Wittel, F. K. & Carmeliet, J., 2012. Computational up-scaling of anisotropic swelling and mechanical behavior of hierarchical cellular materials. *Composites Science and Technology,* Volume 72, pp. 744-751.

Reichert, S., Menges, A. & Correa, D., 2015. Meteorosensitive architecture: Biomimetic building skins based on materially embedded and hygroscopically enabled responsiveness. *Computer-Aided Design,* Volume 60, pp. 50-69.

Rémond, R., De La Cruz, M., Aléon, D. & Perré, P., 2013. Investigation of oscillating climates for wood drying using the flying wood test and loaded beams: nood for a new mechano-sorptive model. *Maderas: Ciencia y technologia,* Volume 15, pp. 269-280.

Reyssat, E. & Mahadevan, L., 2009. Hygromorphs: from pine cones to biomimetic bilayers. *Journal of the Royal Society Interface,* Volume 6, pp. 951-957.

Saft, S. & Kaliske, M., 2013. A hybrid interface-element for the simulation of moisture induced cracks in wood. *Engineering Fracture Mechanics,* Volume 102, pp. 32-50.

Santoni, I., allone, E., Sandak, A., Sandak, J., Dirè, S., 2015. Solid state NMR and IR characterization of wood polymer structure relation to tree provenance. *Carbohydrate Polymers,* Volume 117, pp. 710-721.

Sar, B. E., Fréour, S., Davies, P. & Jacquemin, F., 2012. Coupling moisture diffusion and internal mechanical states in polymers - A thermodynamical approach. *European Journal of Mechanics A/Solids,* Volume 36, pp. 38-43.

Schellen, H. L., 2002. *Heating Monumental Churches: Indoor Climate and Preservation of Cultural Heritage, PhD Thesis.* Eindhoven : Eindhoven University of Technology.

Scherer, G. W., 1987. Drying gels: III. Warping plate. *Journal of Non-Crystalline Solids,* Volume 91, pp. 83-100.

Scherer, G. W., 1992. Bending of gel beams: method for characterizing elastic properties and permeability. *Journal of Non-Crystalline Solids,* Volume 142, pp. 18-35.

Scherer, G. W., 2016. *Personal correspondence.* Princeton University.

Scherer, G. W., Prévost, J. H. & Wang, Z.-H., 2009. Bending of a poroelastic beam with lateral diffusion. *International Journal of Solids and Structures,* Volume 46, pp. 3451-3462.

Schniewind, A. P. & Barrett, J. D., 1972. Wood as a linear orthotropic viscoelastic material. *Wood Science and technology,* Volume 6, pp. 43-57.

Senni, L., Caponero, M., Casieri, C., Felli, F., De Luca, F., 2010. Moisture content and strain relation in wood by Bragg grating sensor and unilateral NMR. *Wood Science and Technology,* Volume 44, pp. 165-175.

Senni, L., Casieri, C., Bovino, A., Gaetani, M. C., De Luca, F., 2009. A portable NMR sensor for moisture monitoring of wooden works of art, particularly of paintings on wood. *Wood Science and Technology,* Volume 43, pp. 167-180.

Siau, J. F., 1984. *Transport processes in wood.* Berlin, Heidelberg, New York: Springer.

Simpson, W., 1980. Sorption theories applied to wood. *Wood and Fiber Science,* Volume 12, pp. 183-195.

Simpson, W. T., 1973. Prediciting equilibrium moisture content of wood by mathematical models. *Wood and Fiber Science,* Volume 5, pp. 41-49.

Simpson, W. T., 1993. Determination and use of moisture diffusion coefficient to characterize drying of northern red oak (Quercus rubra). *Wood Science and Technology,* Volume 27, pp. 409-420.

Simpson, W. T. & Liu, J. Y., 1991. Dependence of the water vapor diffusion coefficient of aspen (Populus spec.) on moisture content. *Wood Science and Technology,* Volume 26, pp. 9-21.

Skaar, C., 1988. *Wood-water relations.* Berlin: Springer-Verlag.

Skaar, C. & Babiak, M., 1982. A model for bound-water transport in wood. *Wood Science and Technology,* Volume 16, pp. 123-138.

Stamm, A. J., 1927. The electrical resistance of wood as a measure of its moisture content. *Industrial and Engineering Chemistry,* Volume 19, pp. 1021-1025.

Stamm, A. J., 1959. Bound-water diffusion into wood in the fiber direction. *For Prod J,* Volume 9, pp. 27-32.

Stamm, A. J. & Nelson, R. M., 1961. Comparison between measured and theoretical drying diffusion coefficients. *Forest Products Journal,* Volume 11, pp. 536-543.

Strauss, W. A., 2008. *Partial differential equations: an introduction.* 2nd ed. Hoboken, NJ: John Wiley & Sons, Inc.

Taccola, S., Greco, F., Sinibaldi, E., Mondini, A., Mazzolai, B., Mattoli, V., 2015. Toward a new generation of electrically controllable hygromorphic soft actuators. *Advanced Materials,* Volume 27, pp. 1668-1675.

Talbot, A. & Kitchener, J. A., 1956. Diffusion (or conduction) along a slightly tapering tube, and its application to the determination of diffusion coefficients. *British Journal of Applied Physics,* Volume 7, pp. 96-97.

Telkki, V.-V., Yliniemi, M. & Jokisaari, J., 2013. Moisture in softwoods: fiber saturation point, hydroxyl site content, and the amount of micropores as determined from NMR relaxation time distributions. *Holzforschung,* Volume 67, pp. 291-300.

Time, B., 1998. *Hygroscopic moisture transport in wood, PhD Thesis.* Norwegian University of Technology, Trondheim.

Tuttle, F., 1925. A mathematical theory of the drying of wood. *Journal of the Franklin Institute,* Volume 200, pp. 609-614.

Uetimane Junior, E., Allegretti, O., Terziev, N. & Söderström, O., 2010. Application of non-symmetrical drying tests for assessment of drying behaviour of ntholo (Pseudolachnostylis maprounaefolie PAX). *Holzforschung,* Volume 64, pp. 363-368.

Valckenborg, R. M. E., Pel, L., Hazrati, K., Kopinga, K., Marchand, J., 2001. Pore water distribution in mortar during drying as determined by NMR. *Materials and Structures,* Volume 34, pp. 599-604.

van Laarhoven, K. A., Huinink, H. P., Segers, F. J. J., Dijksterhuis, J., Adan, O. G. C., 2015. Seperate effects of moisture content and water activity on the hyphal extension of Penicillium rubens on porous media. *Environmental Microbiology,* Volume 17, pp. 5089-5099.

van Meel, P. A., Erich, S. J. F., Huinink, H. P., Kopinga, K., de Jong, J., Adan, O. G. C., 2011. Moisture transport in coated wood. *Progress in Organic Coatings,* Volume 72, pp. 686-694.

Vichit-Vadakan, W. & Scherer, G. W., 2003. Measuring permeability and stress relaxation of young cement paste by beam bending. *Cement and Concrete Research,* Volume 33, pp. 1925-1932.

Viel, S., Capitani, D., Proietti, N., Ziarelli, F., Segre, A. L., 2004. NMR spectroscopy applied to the Cultural Heritage: a preliminary study on ancient wood characterisation. *Applied Physics A,* Volume 79, pp. 357-361.

Vlaardingerbroek, M. T. & Den Boer, J. A., 2003. *Magnetic resonance imaging: theory and practice.* 3rd ed. Berlin: Springer-Verlag.

Wadsö, L., 1994. Describing non-Fickian water-vapour sorption in wood. *Journal of Materials Science,* Volume 29, pp. 2367-2373.

Wadsö, L., Svennberg, K. & Dueck, A., 2004. An experimentally simple method for measuring sorption isotherms. *Drying Technology*, Volume 22, pp. 2427-2440.

Yang, T. & Ma, E., 2014. Dynamic sorption and hygroexpansion of wood subjected to cyclic relative humidity changes. II. Effect of temperature. *BioResources*, Volume 10, pp. 1675-1685.

Zhang, J. & Scherer, G. W., 2012. Permeability of shale by the beam-bending method. *International Journal of Rock Mechanics & Mining Sciences*, Volume 53, pp. 179-191.

Zhou, Y., Fushitani, M., Kubo, T. & Ozawa, M., 1999. Bending creep behavior of wood under cyclic moisture changes. *Journal of Wood Science*, Volume 45, pp. 113-119.